MINISTÉRIO DA EDUCAÇÃO
UNIVERSIDADE FEDERAL DO RIO GRANDE DO SUL
PROGRAMA DE PÓS-GRADUAÇÃO EM ENGENHARIA MECÂNICA

RESIDUAL STRESS IMPACT ON FATIGUE PERFORMANCE OF ALUMINUM INTERNAL COMBUSTION ENGINE CYLINDERS

por

Lucas Breda Soares

Dissertação para obtenção do Título de
Mestre em Engenharia

Porto Alegre, Maio de 2023

RESIDUAL STRESS IMPACT ON FATIGUE PERFORMANCE OF ALUMINUM INTERNAL COMBUSTION ENGINE CYLINDERS

por

Lucas Breda Soares
Engenheiro

Dissertação submetida ao Corpo Docente do Programa de Pós-Graduação em Engenharia Mecânica, PROMEC, da Escola de Engenharia da Universidade Federal do Rio Grande do Sul, como parte dos requisitos necessários para a obtenção do Título de

Mestre em Engenharia

Área de Concentração: Mecânica dos Sólidos

Orientador: Prof. Dr. Jakson Manfredini Vassoler

Comissão de Avaliação:

Prof. Dr. Ignácio Iturrioz ..... PROMEC / UFRGS

Dra. Larissa Domingues Lemos ..... STIHL

Prof. Dr. Rogério José Marczak ..... PROMEC / UFRGS

Prof. Dr. Felipe Roman Centeno
Coordenador do PROMEC

Porto Alegre, 25 de Maio de 2023

Agradeço à minha esposa Sabrina, minha família e amigos por todo o suporte dado durante a execução do mestrado e dissertação.

RESUMO

A avaliação de falhas por fadiga em componentes manufaturados em ligas de alumínio submetidos ao tratamento térmico T6 é uma tarefa complexa, pois tensões residuais impostas por este tratamento podem ter grande influência sobre a durabilidade do componente. O presente trabalho tem como objetivo propor uma metodologia capaz de prever as tensões residuais impostas no tratamento térmico T6 realizado em cilindros de motores de combustão interna e o impacto destas tensões na vida em fadiga do componente. Para isto, foi proposta uma metodologia em duas etapas, onde primeiramente foi resolvido um problema térmico para obtenção da distribuição de temperatura, utilizada posteriormente como condição de contorno de um problema termomecânico. A primeira etapa da solução do problema térmico é a solução de um problema inverso de transferência de calor para encontrar parâmetros térmicos que representem o histórico de temperatura medido experimentalmente durante o tratamento térmico. Na segunda etapa, com os parâmetros térmicos calibrados, e a distribuição de temperatura, um problema térmomecânico inelástico é resolvido para calcular as tensões residuais provenientes dos carregamentos térmicos calculados, considerando o efeito de viscosidade que o material sofre nas temperaturas alcançadas durante o tratamento térmico. Por fim, um teste de durabilidade em bancada foi simulado e os fatores de segurança para falhas em fadiga foram calculados, com e sem a influência das tensões residuais, o que mostrou que a precisão da predição do modelo de fadiga foi melhorada significativamente quando utilizada a metodologia proposta. Tal conclusão é corroborada por análises de sensibilidade executadas para avaliar desvios nas respostas frente as possíveis escolhas no desenvolvimento dos modelos.

Palavras-chave: Tensões residuais; Fadiga; Tratamento térmico; Alumínio; Motor.

ABSTRACT

The fatigue assessment of aluminum alloy components submitted to a T6 thermal treatment is a challenging task as the fatigue performance can be highly influenced by the residual stress input during the thermal treatment. The present work aims to propose a methodology capable of evaluating the residual stress input during the manufacturing process of an aluminum internal combustion engine cylinder and its impact on the component fatigue performance. For this, a two-step methodology was proposed, in which a thermal problem is solved to find the temperature distribution used later as a boundary condition in a thermomechanical problem. In the first step, an inverse heat transfer problem is solved to find the thermal parameters capable of reproducing the experimental temperature history acquired during the thermal treatment. In the second step, with the calibrated thermal parameters, and the temperature distribution, an inelastic thermomechanical problem is solved to evaluate the residual stress caused by the thermal loads. In addition, creep effects induced by the elevated temperatures achieved during the thermal treatment are considered. Finally, a bench test was simulated, and the endurance safety factors with and without residual stress influence were evaluated and compared to experimental fatigue data, which showed that the proposed methodology could significantly improve the model prediction accuracy. This conclusion is supported by sensitivity analyses carried out to assess deviations in responses due to possible choices in model development.

Keywords: Residual stress; Fatigue; Thermal treatment; Aluminum; Engine.

INDEX

LIST OF FIGURES

LIST OF TABLES

LIST OF ABBREVIATIONS

ASO	Adaptive single objetive
CFD	Computational fluid dynamics
DOE	Design of experiment
HTC	Heat transfer coefficient
IHTC	Inverse heat transfer coefficient
MISO	Multilinear isotropic hardening
MISQP	Mixed-integer sequential quadratic programming
OSF	Optimal space-filling
RS	Residual stress
SQP	Sequential quadratic programming

LIST OF SYMBOLS

Latin Symbols

c_A	Weighting function constant
C_{ijkl}	Elasticity tensor, Pa
C_n	Creep model material parameters
Cg	Equal-or-less optimization function restriction
Ch	Equal optimization function restriction
$\ddot{q}$	Heat flux, W/m^2
d_A	Trial solution unknown
D_{ij}	Elasticity matrix, Pa
E	Modulus of elasticity, Pa
f	Cost function
$^{th}\mathrm{f}$	Heat generation per unit of body volume, W/m^3
$^{me}\mathrm{f}$	Prescribed body force per unit of volume, N/m^3
$F(\sigma)$	Scalar function of stress, Pa
F_i	Force vector, N
$^{th}\mathrm{g}$	Temperature (Dirichlet) boundary condition, K
$^{me}\mathrm{g}$	Displacement (Dirichlet) boundary condition, m
$^{th}\mathrm{g}_0$	Initial temperature, K
$^{th}\mathrm{h}$	Heat flux (Neumann) boundary condition, W/m^2
$^{me}\mathrm{h}$	Surface traction (Neumann) boundary condition, Pa
h_f	Film coefficient, W/(m^2·K)
H^1	Functions contained in Hilbert space
k	Thermal conductivity, W/(m·K)
K	Number of equal-or-less function restrictions
Ky, Kf, KZ	Kriging functions
l_0	Characteristic length, m
L	Number of equal function restrictions
n	Normal vector
N	Shape function
n_{dof}	Number of degrees of freedom per node

n_{el}	Number of elements
N_f	Number of cycles to failure
n_{np}	Number of nodes
n_{sd}	Number of space dimensions
P_{ID}	Global equation number
q	Heat flux, W
$q_{convection}$	Convective heat flux, W
Q	Plastic potential, Pa
R	Load Ratio
SF_e	Endurance safety factor
t	Time, s
T	Temperature, K
T_B	Fluid bulk temperature, K
T_S	Solid surface temperature, K
T_{sat}	Saturation temperature, K
T_w	Water temperature, K
u	Trial solution
u_i	Displacement vector, m
u^h	Trial solution approximation
w	Weighting function
w^h	Weighting function approximation
$\mathbf{x}$	Vector of coordinates of global domain
$\mathbf{x^e}$	Vector of coordinates of element domain

Greek Symbols

α^{se}	Secant coefficient of thermal expansion, 1/K
Γ	Contour surface
Γ_g	Dirichlet boundary condition application surface, m^2
Γ_h	Neumann boundary condition application surface, m^2
δ_{ij}	Kronecker delta
ε	Strain, m/m
ε_{ij}^{cr}	Creep strain tensor, m/m

ε_{ij}^{el}	Elastic strain tensor, m/m
ε_{ij}^{pl}	Plastic strain tensor, m/m
ε_{ij}^{th}	Thermal strain tensor, m/m
ε_y	Yield strain, m/m
ζ	Set of trial solutions
ζ^h	Set of approximations of trial solutions
η	Set of global node numbers
η_{g_i}	Set of nodes with Dirichlet boundary condition
κ_{ij}	Conductive matrix, W/(m·K)
λ	Magnitude of the plastic strain increment, m/m
ν	Set of weighting functions
ν^h	Set of approximations of weighting functions
ξ'	Set of history dependent internal variables
ξ	Vector of coordinates of local domain
σ_a	Alternate stress, Pa
σ_e	von Mises equivalent stress, Pa
σ_f	Fatigue strength for load ratio R-=1, Pa
σ_{ij}	Stress tensor, Pa
σ_m	Mean stress, Pa
σ_{max}	Maximum stress on fatigue cycle, Pa
σ_{min}	Minimum stress on fatigue cycle, Pa
σ_{UTS}	Ultimate tensile strength, Pa
σ_y	Yield stress, Pa
Ω	Body domain
Ω^e	Discretized body domain

1 INTRODUCTION

One of the top priorities of the project of handheld machines is weight saving, which can be achieved by using low-specific density and high-strength materials. Aluminum alloys are a popular choice for manufacturing internal combustion engines due to their high fatigue strength to specific density ratio [Dixit et al., 2008]. In order to obtain their peak strength, the aluminum alloys are usually submitted to a thermal treatment prior to the component usage. However, such treatments might also input residual stresses [Robinson and Tanner, 2003], which may significantly affect the component endurance performance. Tensile residual stress is usually detrimental to fatigue life, while compressive residual stress is usually beneficial [Webster and Ezeilo, 2001]. Therefore, accurate residual stress prediction is crucial to obtain reliable lightweight components. Otherwise, it would be necessary to manufacture an overengineered component to sustain the unknown residual stress without presenting fatigue failures.

The T6 thermal treatment is a common choice for the treatment of aluminum alloys, as it usually yields the maximum fatigue strength through the increase of the material ductility [Dahle, 2001]. The treatment compromises three processes: solution, quenching and artificial ageing. The first process is done by maintaining the components at temperatures close to the material melting temperature - between 470 and 540 °C for most series 2000, 6000, 7000 and 8000 of aluminum alloys [Davis, 1993] - for a long period, in order to obtain the highest possible concentration of solute in solid solution [Dahle, 2001]. The second process is accomplished by quickly cooling down the components to avoid the precipitation of the solute, which would be detrimental to the resulting material strength. However, the severe thermal gradients imposed during the cooling process may input permanent distortions and residual stress in the treated components [Koç et al., 2006]. Finally, the artificial ageing is done by keeping the parts at intermediate temperatures - usually between 100 and 200 °C for aluminum alloys - for a long period. It aims to achieve a controlled decomposition of the supersaturated solid solution in fine dispersed precipitates, which plays an important role in the increase of yield and tensile strength of the alloy [Dahle, 2001]. During artificial ageing, the thermal gradients are low; thus, no residual stress is formed. However, the long exposition of the parts to elevated temperatures activates the material macroscopic viscous effects, resulting in creep and

partial relaxation of the residual stress loaded regions [James, 1987].

By the end of the thermal treatment processes, the parts are submitted to residual stress, which remains within the parts and will interact with working loads. Thus, the development of a methodology capable of predicting residual stress formation is necessary to obtain an accurate evaluation of the real stress occurring in the component during its utilization, which is fundamental for the project of reliable lightweight components. Additionally, the proposed method can be used to optimize the manufacturing process parameters and component geometry to minimize the residual stress formation.

1.1 Objectives

The main objective of the present work is to propose a method capable of predicting the residual stress formation due to the cylinder manufacturing processes and its influence on the bench test endurance performance. Thus, the primary objectives are set:

- To evaluate the residual stress field resulting from the thermal loads input during the T6 thermal treatment.
- To verify the influence of residual stress on the cylinder endurance performance on the bench test and compare to the experimental data.

1.2 Data Confidentiality Disclaimer

The present work was developed within the context of a two-stroke cylinder industrial development. The confidential data - such process parameters, product geometry and material specifications - have been simplified in a way that the sensitive data remains confidential, but the reader can understand the proposed methodology and results. The geometry is presented here in a simplified model, and the material and process parameters are presented in schematic diagrams, in which the magnitude of the presented variables are suppressed.

2 THE RESIDUAL STRESS PROBLEM

2.1 Internal Combustion Engines

Internal combustion engines are built to last for hundreds of hours of usage. Two-stroke engines can work in angular velocities up to approximately 15.000 revolutions per minute, which means that the engine must sustain several millions of combustion cycles during its designed lifetime. During the engine development phases, it would not be practical to test the engines in real work conditions during to its long duration and associated high cost.

A common solution to overcome this issue is using an experimental accelerated fatigue test, in which loads higher than the ones experienced in the real work condition are applied to evaluate the component fatigue performance in a shorter period. Such experiment is performed in a bench test machine, where the applied load amplitude and frequency can be controlled. This type of experimental analysis allows the evaluation of functional failures of the component. However, with this approach, it is not always possible to experimentally estimate which mechanical phenomenon (inelasticities, residual stress, and others) was present in the physical problem. The lack of information may lead the engineer to rely on hypotheses that need further validation.

Analyzing experimental observation of a bench test against the numerical results using the finite element method, it was possible to notice that some engine cylinders presented earlier fatigue failures as expected by the numerical results. Such cylinders have one common aspect: they are all submitted to the T6 thermal treatment. Thus, there is a strong suspicion that this process may induce effects in the cylinders that are not being considered in the numerical model. Therefore, it could explain the cause of the unexpected failures. One of the solutions to avoid such failures would be to reduce the allowable stress; however, it would be necessary to do it for the entire component as the location of the residual stress formation is uncertain. This would result in an overengineered component, which would go against one of the top project requirements: weight saving. Another approach would be to develop a methodology capable of estimating the residual stress location and magnitude, which could be input in the fatigue model in order to obtain a reliable fatigue performance prediction.

Purely experimental methods may be used to evaluate local information (tempe-

rature, strain, stress), including inelasticities and residual stress [Withers and Bhadeshia, 2001]. However, usually, they are challenging to apply in complex geometries since the critical regions may not be accessible. On the other hand, these methods can provide useful local experimental data for verification and validation procedures or even to be used as input on a numerical approach [Xiao et al., 2022]. Numerical methods can be used more broadly. For example, finite element analyses allow us to obtain the stress field in a component submitted to the same loading applied in a bench test. Then, fatigue models can be used to predict the occurrence of fatigue failures numerically. Finally, the numerical results can be compared against experimental fatigue data and validate the mechanical model. This approach is used to save time and resources as the component geometry can be optimized to sustain a given load for a given number of cycles in a virtual environment. The feedback of the bench test results in the numerical model allows the fatigue parameters calibration, which results in a model capable of giving reliable predictions for the component fatigue performance.

2.2 Residual Stress

Residual stress is defined as a stress which remains in a stationary body in the absence of any external loads. It interacts with the in-service stresses [Withers and Bhadeshia, 2001], and the result of this interaction may be detrimental or beneficial to the endurance performance of the component, depending on the tensile or compressive nature of the residual stress [Zhang et al., 2018]. Residual stress may be categorized and analyzed by the characteristic length over which it self-equilibrates and by its origin.

2.2.1 Characteristic Length

Residual stress can be analyzed according to its characteristic length l_0 which is the length over which it self-equilibrates. Type I residual stress equilibrates over macroscopic scale ($l_0 \approx$ scale of structure), Type II equilibrates over a certain number of microstructure grains ($l_0 \approx$ 3-10 grains size) and Type III equilibrates over a certain number of atoms ($l_0 <$ grain size) [Withers and Bhadeshia, 2001]. The definition of the scale in which residual stress is analyzed depends on the problem in consideration. For example, in the design of composite materials, type II stresses are the main interest, as it is desired to know the interaction between the microstructure matrix and reinforcement. In the

life assessment of metallic components, as proposed in the current work, the attention is focused on type I residual stresses, as the main interest is in evaluating the macroscopic regions of potential failure.

2.2.2 Origin of Macroscopic Residual Stress (Type I) on Engineering Applications

Macroscopic residual stress may arise in engineering components in at least four different ways: due to interactions of different parts within an assembly; due to thermal, chemical, or plastic strain-induced misfits in different regions of the part.

An example of residual stress originating from the interaction of components in an assembly is given by a shrink-fit plug, whereas an oversized plug is fitted in a hole by cooling it down before the assembly. When the assembly temperature equalizes, an interference arises and both parts get loaded. An analogous test is the standard for the assessment of neutron diffraction stress measurement as part of the Versailles Agreement on Measurements and Standards working group TWA20 [Webster, 2000]. Thermal misfits are common in assemblies composed of parts with different materials which experience varying temperatures, as seen in electronic devices.

Macro residual stress may also be originated from inhomogeneous plastic strain formation input by mechanical means. The bending of a bar beyond its elastic limit is a simple way of introduction non-uniform plastic strain. Once a region is yielded, future loads would have to exceed previous load magnitudes to further yield the material in such regions. Several processes in the industry exploit this effect by previously yielding the material in the same direction as future loads to minimize future yielding. Examples of such processes include autofretagging of cylinders and gun barrels [Fletcher, 1985], overspeeding of rotating discs [Faupel and Fisher, 1981], prestressing of springs and overloading in pressure vessels [Leggatt and Davey, 1981]. Plastic strain formation can also be used to induce compressive superficial residual stress, to reduce the mean stress in future fatigue load cycles, improving the part lifetime. This phenomenon is also used in several industrial applications, such as shot peening and grinding [Schajer et al., 1996].

Another mean of generating residual stress by inhomogeneous plastic strain formation is by thermal loads. An example of thermal load is welding. Large thermal stress gradients are imposed due to the localized heating and subsequent cooling in the vicinity

of the heat-affected zone. These gradients can cause thermal cracks, distortions, and reduced service life on the welded component [Radaj, 1992]. Another well-known process that results in plastic strains due to thermal loads is the one imposed during cold water quenching in aluminum alloys, in which the heated component is suddenly submerged in a coolant media resulting in severe thermal gradients. The load imposed by such gradients might exceed the elastic limits of the material at the given instantaneous temperature and result in non-homogeneous in plastic strain formation [Robinson et al., 2014].

2.3 T6 Thermal Treatment Impact on Residual Stress

Controlled heat treatment of aluminum alloys is of great interest in engineering applications as it can improve the material mechanical properties, such as strength, ductility, and fracture toughness. In the heat treatment designation system for aluminum alloys, T6 corresponds to a sequence of three processes: solution heat treatment, quenching and artificial ageing.

2.3.1 Solution Heat Treatment

The solution heat treatment is done by keeping the parts at high enough temperatures for a long enough period to obtain the maximum concentration of solute in a solid solution. [Dahle, 2001]. The solution temperature is usually defined between 470 and 540 °C for most series 2000, 6000, 7000 and 8000 aluminum alloys [Davis, 1993]. At this temperature level, the yield strength of the alloy is significantly reduced and plasticity mechanisms relief the elastic strains through thermal activation of discordances. [James, 1987]. Then, the residual stress formed during the foundry is relieved during the solution heat treatment [Jeanmart and Bouvaist, 1985].

2.3.2 Quenching

After solution heat treatment, the parts must be cooled down quickly enough so the solute remains in a solid solution. Usually, the optimal mechanical properties are associated with high cooling rates [Dahle, 2001]. Thus, it is desirable to obtain the highest cooling rate possible in order to obtain the best achievable mechanical properties. However, thermal gradients induced by the high cooling rates create thermal stress which

may exceed the yield strength of the material for the given instantaneous temperature and may lead to the formation of inhomogeneous plastic strain, resulting in residual stress and distortion in the quenched parts [Jeanmart and Bouvaist, 1985; Prime and Hill, 2002; Earle et al., 2004; Dolan and Robinson, 2004; Koç et al., 2006]. Heated water, usually at temperatures between 50 and 80 °C [Dahle, 2001], can be used to avoid excessive residual stress and distortion.

2.3.3 Artificial Ageing

Artificial ageing promotes the controlled decomposition of the supersaturated solid solution into finely dispersed precipitates, which raises both yield and tensile strength. Such decomposition is obtained by slowly increasing the part temperature up to temperatures which stays usually between 100 to 200 °C and kept in these temperatures for periods between 2 to 48 h [Dahle, 2001] and then slowly cooling down to ambient temperature.

The long exposition of the parts at elevated temperatures activates the material macroscopic viscous effects, in which classical creep diffusion allows the loaded regions to counterbalance themselves, partially relieving the residual stress [James, 1987]. An example of the effect of temperature and time on the residual stress relaxation can be seen in Figure 2.1 for mild steel.

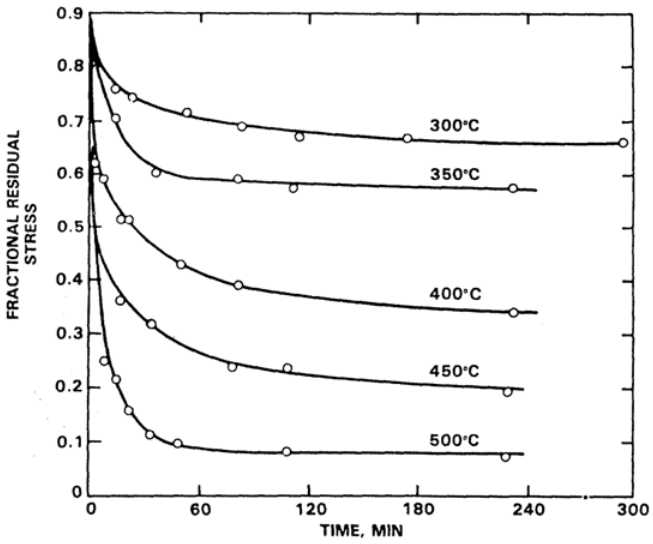

Figure 2.1 – Temperature and time effect on stress [Adeyemi et al., 1979].

2.4 Thermal Modeling of T6 Thermal Treatment for Residual Stress Prediction

The modeling of residual stress development can be done in a two-step analysis, in which a thermal model is proposed to evaluate the temperature profile history during the thermal treatment and then a structural model to predict the stresses and displacements resulting from the calculated thermal loads [Jeanmart and Bouvaist, 1985; Yang et al., 2013a; Louhichi et al., 2022]. The main challenge in the thermal model is the determination of the heat transfer rate from the body to the environment through its boundaries.

2.4.1 Thermal Modeling of Solution Heat Treatment

The modeling of the complete solution heat treatment is unimportant for the residual stress prediction in the T6 heat treatment as the residual stresses from previous manufacturing processes are nulled in this heat treatment phase [Jeanmart and Bouvaist, 1985]. As the parts are kept at elevated temperatures for a long period of time, they reach thermal equilibrium with the high ambient temperature in the furnace. A stress-free part at a constant temperature equal to the solution temperature is usually the initial condition for the modeling of the T6 thermal treatment found in previous work [Louhichi et al., 2022].

2.4.2 Thermal Modeling of Quenching

Most of the work published for residual stress prediction on heat treatment of aluminum alloys focus on the quenching [Louhichi et al., 2022; Zhang et al., 2013; Yang et al., 2013b] as it is the main factor for residual stress formation on the thermal treatment of aluminum alloys [Koç et al., 2006]. Quenched parts begin at a homogeneous temperature equal to the solution treatment temperature, and then they are submerged in a coolant media and let to cool down. The solution temperature for aluminum alloys is usually higher than 470 °C [Davis, 1993], which is higher than the water boiling temperature. This results in a specific cooling regime that is developed in three main stages [Babu and Prasanna Kumar, 2009]. Film boiling regime occurs when the solid surface is at a high temperature, where a thin vapor film is formed between the solid surface and water

preventing them from getting directly in contact. The film acts as an insulation, resulting in a relatively low and stable heat flux in this regime. Nucleate boiling regime occurs when the solid surface temperature drops below the minimum film collapse temperature, known as Leidenfrost temperature [Meduri et al., 2009]. The solid surface is almost in direct contact with the water, resulting in the formation of a large amount of vapor bubbles. The heat flux is relatively high at this regime due to the phase change in addition to the water agitation promoted by the bubbles. Nonboiling regime occurs when the solid surface temperature drops below water boiling temperature, resulting in a relatively low and stable heat flux [Tensi et al., 1994]. A schematic diagram is presented in Figure 2.2, showing the correlation between heat flux and the boiling regimes.

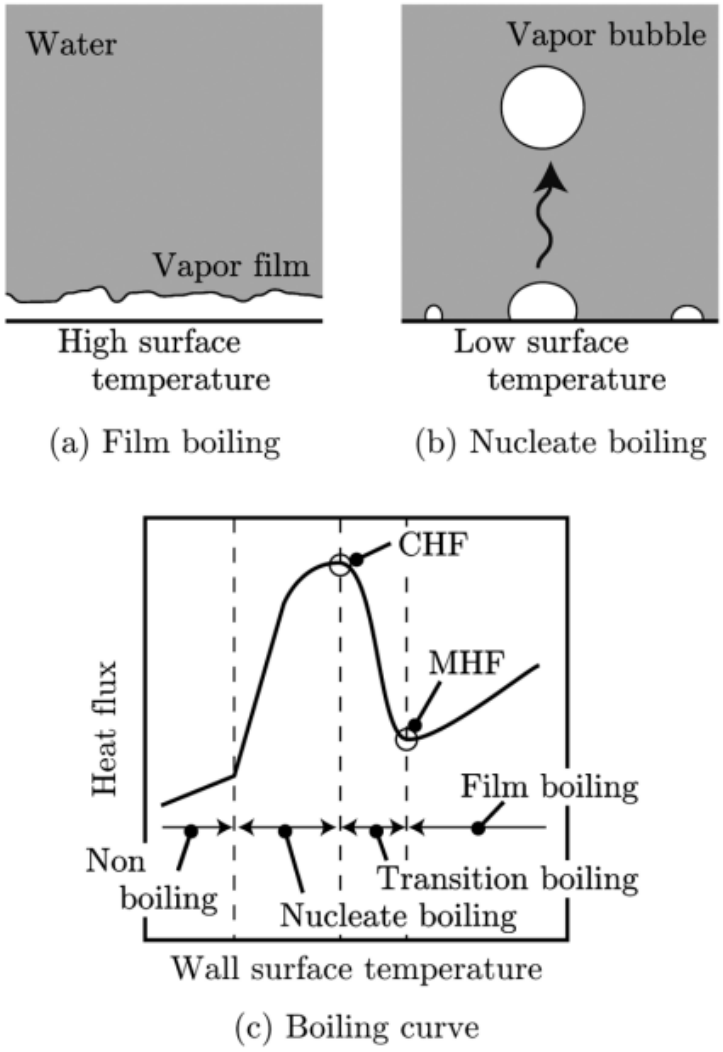

Figure 2.2 – Schematic diagram of boiling phenomenon [Kobayashi et al., 2016].

The heat flux modeling must capture the effects of the different boiling regimes

experienced by the quenched part during its cooling. The determination of the heat flux can be achieved by different methods. The boiling curve [Nukiyama, 1934] can be used in a thermal model to directly determine the heat transfer coefficient in function of the excess temperature, which is defined as the solid temperature T which exceeds the coolant saturation temperature T_{sat} [Jeanmart and Bouvaist, 1985; Faghri and Zhang, 2006].

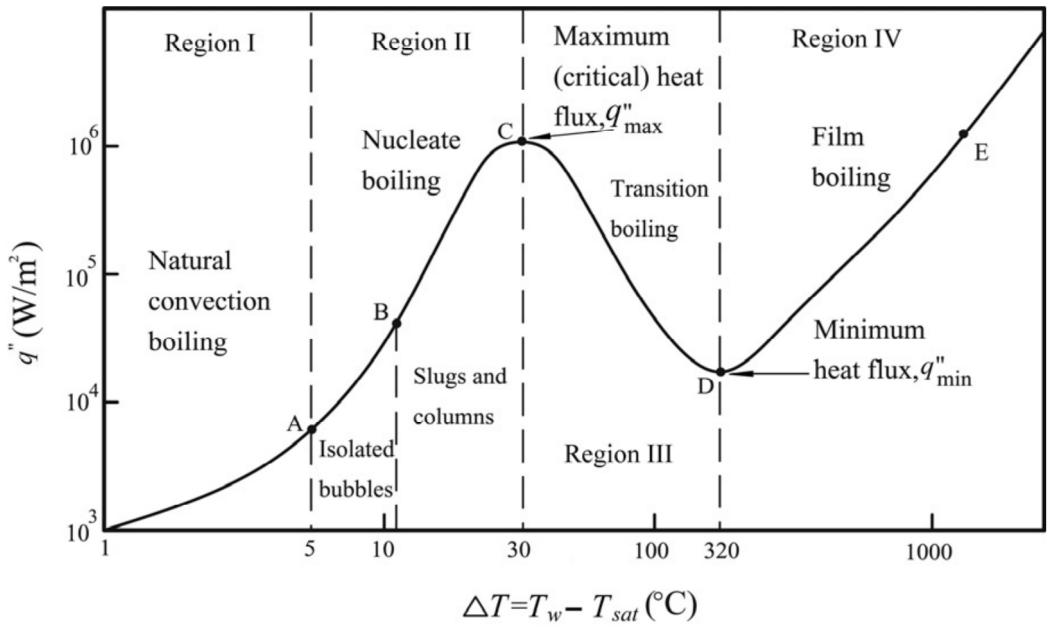

Figure 2.3 – Schematic temperature dependent heat flux during boiling [Faghri and Zhang, 2006].

The inverse heat transfer coefficient method can be used to determine the heat transfer coefficients through the numerical optimization of the coefficients using experimental data as a benchmark [Louhichi et al., 2022; Zhang et al., 2013; Yang et al., 2013b]. A computational fluid dynamics (CFD) model can be used to solve the water multiphase flow and the boiling regimes, resulting in a detailed profile of heat transfer coefficients [Kunugi, 2000; Kopun et al., 2014b]. Several works were published about quenching of aluminum engine heads with complex geometries using a CFD analysis [Kopun et al., 2014a; Jan and Nannapuraju, 2017].

2.4.3 Thermal Modeling of Artificial Ageing

The heating up and cooling down experienced by the parts submitted to the artificial ageing process is done at low heating and cooling rates, respectively. Usually, a

furnace is used to heat up the parts and the cooling down is done by letting the parts sit at ambient temperature. Both processes usually occur at still air, and most of the heat exchanged is done by natural convection. The modeling of still air convective heat transfer is of great interest for several research fields. Thus, there are several publications on this topic [Gartling, 1977; Padet, 2005], showing great agreement between numerical models and experimental tests. However, no specific work could be found about the thermal modeling of artificial ageing for aluminum alloys.

2.5 Mechanical Modeling of T6 Thermal Treatment for Residual Stress Prediction

With the determination of the temperature history in the part during the T6 thermal treatment, the temperature profiles can be applied to a structural model to predict the residual stress resulting from the thermal loads. The appropriate material models and their required material properties are essential to represent the material behavior, as the high temperatures experienced by the parts during the thermal treatment may lead to non-negligible plasticity and creep effects, resulting in residual stress formation and relaxation, and part distortion. [Lacarac et al., 2004; Louhichi et al., 2022].

2.5.1 Mechanical Modeling of Solution Heat Treatment

As previously mentioned, the solution heat treatment is unimportant for the residual stress prediction as the residual stresses from previous manufacturing processes are nulled in this heat treatment phase [Jeanmart and Bouvaist, 1985]. Most of the published aluminum alloy heat treatment simulations focus on quenching and artificial ageing [Zhang et al., 2013; Louhichi et al., 2022].

2.5.2 Mechanical Modeling of Quenching

Severe thermal gradients are imposed when the heated parts from solution treatment are suddenly submerged in water, resulting in stress gradients due to the inhomogeneous thermal expansion within the part. If such stresses exceed the elastic limits of the material for the given instantaneous temperature, inhomogeneous plastic strain, and thus, residual stress and distortion may be formed [Dolan and Robinson, 2004; Earle

et al., 2004]. Previous works used a finite element model to evaluate the stress/strain fields, in which a plasticity model was used to evaluate the plastic deformation accumulation during quenching. Ramberg-Osgood [Jeanmart and Bouvaist, 1985], isotropic hardening with Mises criterion [Koç et al., 2006; Li et al., 2007], elastic perfectly plastic [Zhang et al., 2013] and hyperbolic sine [Yang et al., 2013b] plasticity models were used in previous works to evaluate the plastic strain formation during quenching.

The temperature-dependent flow stress curves are necessary to define how the material behaves when the load exceeds the material yield strength for a given temperature. Tensile tests [Jeanmart and Bouvaist, 1985; Zhang et al., 2013] and data found in literature [Koç et al., 2006; Li et al., 2007; Yang et al., 2013b] were used to obtain the temperature-dependent flow stress curves and characterize the chosen plasticity models.

2.5.3 Mechanical Modeling of Artificial Ageing

The parts are heated up and kept at a constant temperature for a long period of time during the artificial ageing process [Dahle, 2001]. During this process, residual stress is partially relieved. The degree of stress relaxation depends mainly on the temperature, initial stress level and time. Different models can be used to represent the stress decay during artificial ageing in the numerical simulation. Uniaxial creep model [Lacarac et al., 2004; Godlewski et al., 2013], Zener-Wert-Avrami model [Yang et al., 2022] and phenomenological models proposed by the authors [Wang et al., 2022] were used in previous works. The material models' coefficients were fitted using an experimental stress relaxation test, in which a constant displacement is applied to a heated specimen and the reaction force necessary to maintain the constant displacement is monitored during a predetermined period. A stress versus time curve can be extracted from such test and used to calibrate the material model for different temperatures and initial stress levels.

2.6 Machining Impact on Residual Stress

Machining is a process in which a part is cut to is final shape and size by the controlled removal of material. Previous works have concluded that the local residual stress caused by machining is dependent on the utilized machining process and its parameters. The influence of cutting speed, feed rate, cutting depth, width of cut and cutting edge geometry on milling of aluminum alloys were investigated [Denkena et al., 2008;

Xiaoming H., 2013].

Extensive research has been done in the development of the modeling of local residual stress caused by different machining processes. Empirical [Fuh and Wu, 1995; El-Axir, 2002], analytical [Merwin and Johnson, 1963; McDowell, 1997] and finite element [Sasahara et al., 1996; Weber et al., 2021] models were proposed to predict the local residual stress due to machining. However, the residual stress input by machining is usually relevant only in the machined surfaces and a small depth below.

The modeling of machining in residual stress loaded components aims to capture the effects in the scale of the components, where usually local residual stress input by the interaction of the cutting tool and the cut material is neglected. Previous works used a bulk material removal modeling [Louhichi et al., 2022; Schulze et al., 2013; Li et al., 2007] to predict the distortion caused by machining. This method assumes an instantaneous single-step machining pass by removing the machined elements of the mesh and recalculating the new equilibrium state.

2.7 Fatigue Failure

Fatigue failures are said to be the ones caused by the application of cyclical loads, whose peak values are usually considerably smaller than the loads necessary to cause a static failure. Fatigue failures can occur in different forms. When it is caused by fluctuations in the externally applied stresses or strains, the failure is said to be due to mechanical fatigue. When the part is submitted to elevated temperatures concomitant to the mechanical cyclical load, the failure is classified as creep-fatigue; when the thermal loads also fluctuate, the induced failure is said to be due to thermomechanical fatigue. If the part is submitted to a chemical aggressive ambient, corrosion fatigue may arise [Suresh, 1998].

The Wöhler curve indicates the number of cycles to failure N_f a material can withstand for a given alternate load σ_a. This curve is given in a log-log diagram with the number of cycles to failure in the abscissa and the amplitude of the applied stress in the ordinate [Sendeckyj, 2001]. Figure 2.4 exemplifies a Wöhler curve built in a laboratory by applying different levels of a fully reversed uniaxial loading to a plain specimen until the breakage occurs. The Wöhler curve gives information about the material resistance to a fully reversed uniaxial load applied to a smooth surface specimen at room tempera-

ture. However, the fatigue response of engineering materials may be highly sensitive to many parameters, such as mean stress effect, temperature, geometrical features, surface treatments and roughness, metallurgical parameters and many others [Hertzberg, 1996; Pook, 2000; Stephens et al., 2000]. All previous parameters should be taken into account in the fatigue assessment as they can lead to an overall decrease in the component fatigue strength.

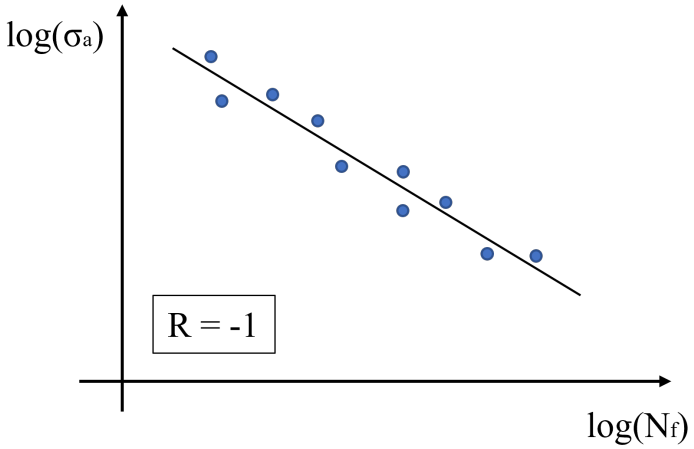

Figure 2.4 – Wöhler diagram for a load ratio R =-1.

The mean stress σ_m effect has an important role in the fatigue assessment of engineering materials. When a tensile static stress is imposed in a uniaxial fatigue loading, it is possible to see that the fatigue damage increases, leading to a premature failure when compared to a test without the imposed static stress. A similar effect is seen by increasing the load ratio R, which increases the mean stress and also has a detrimental effect on the fatigue performance [Susmel, 2009]. Both effects are schematically represented on Figure 2.5.

Experimental data for fatigue test with different mean stress levels are plotted in a non-dimensional diagram showed in the Figure 2.6 alongside selected mean stress correction models. The diagram shows the stress amplitude σ_a divided by the fatigue strength for a load ratio of -1 $\sigma_{a,R-=1}$ on its vertical axis and the mean stress σ_m divided by the ultimate tensile strength σ_{UTS} on its horizontal axis. The experimental data suggests that the fatigue performance of different materials has a different sensibility to mean stress and neither presented models can capture the behavior of all materials. The sensibility to mean stress load of the aluminum alloys (2014-T6, 2024-T4, 6061-T6 and

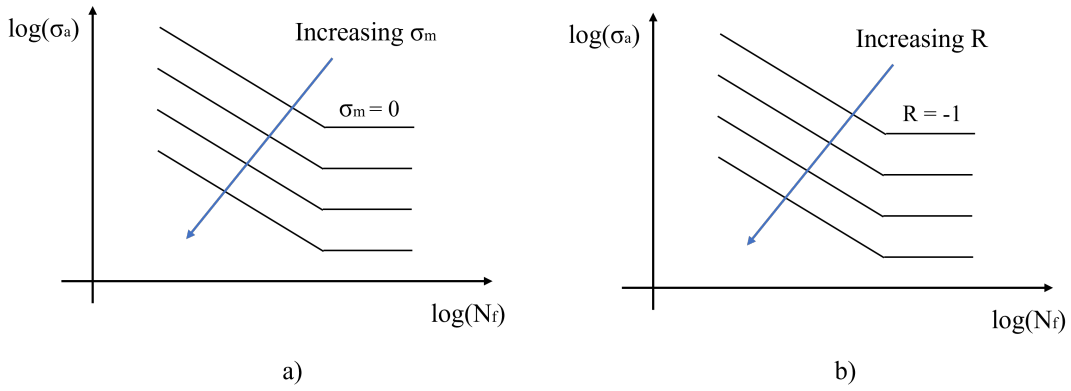

Figure 2.5 – Mean stress and (b) load ratio, R, effect under uniaxial fatigue loading. Adapted from [Susmel, 2009].

7075-T6) seems to be better represented by Dietman's and Gerber's models.

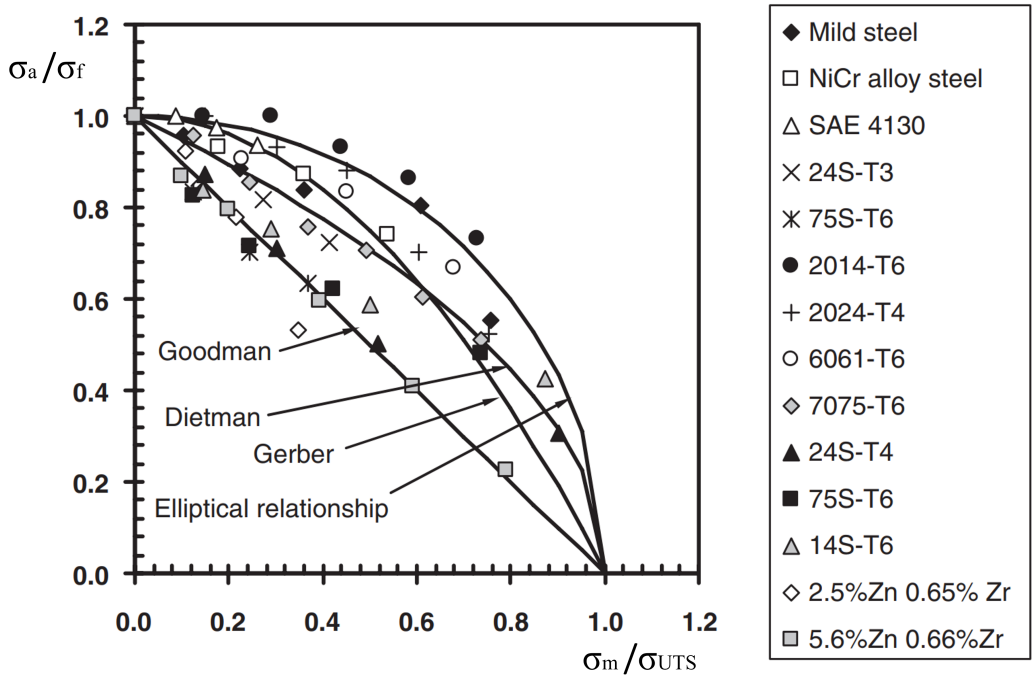

Figure 2.6 – Comparison experimental data and fatigue models to predict the mean stress effect under uniaxial fatigue loading [Frost et al., 1974]

2.7.1 Residual Stress Impact on Fatigue Failures

Residual stress can have a significant impact on fatigue failures. Tensile residual stress tends to accelerate the nucleation and growth of cracks, while compressive resi-

dual stress tends to prolong fatigue life [Webster and Ezeilo, 2001]. Thus, whenever the analyzed part was submitted to previous procedures which imposed residual stress it is necessary to account for it in order to obtain accurate fatigue life assessment. Most of the total life methods account for the mean stress impact on fatigue life by modifying the fatigue limits. Residual stresses may be considered to have a similar effect as a mean stress, as it may be assumed to remain constant during the load cycle in some situations [Rice, 1997]. However, this may not be the case, as residual stress can relax and redistribute during the service life of the component. Yielding, repeated cyclic loading, exposure to elevated temperatures and crack growth can cause significant changes in the residual stress field [McClung, 2007].

There is a great interest in the welding filed on the residual stress impact on fatigue life due to its vast application and potential implications on safety. Recent works proposed the residual stress calculation using finite element model, in which the residual stress is mapped in the same finite element mesh intended to evaluate the working loads. Then, the resulting stress field from the combined working load and residual stress is used to calculate the fatigue cycles and proceed to the life assessment. This workflow was used for evaluation of S355JR structural steel components [Chiocca et al., 2022], aero-engine blades [Xiao et al., 2022] and a welded T-joint [Zhang et al., 2018].

3 THEORETICAL REVIEW

The main objective of this chapter is to keep the text self-contained, providing a theory review of the chosen methods to model the thermal and mechanical behavior of the cylinders during the proposed thermal treatment, the subsequent endurance test and fatigue assessment.

3.1 Thermal Problem

The heat transfer problem to be solved is defined considering a three-dimensional body at temperature T, which occupies the domain Ω and is surrounded by surfaces Γ, such as the one showed in Figure 3.1. The body is subjected to prescribed temperatures thg in the surface Γ_g and prescribed heat flux thh normal to the surface Γ_h. Additionally, the body is subjected to heat generation per unit of body volume thf. The thermal boundary conditions are schematically represented in Figure 3.1.

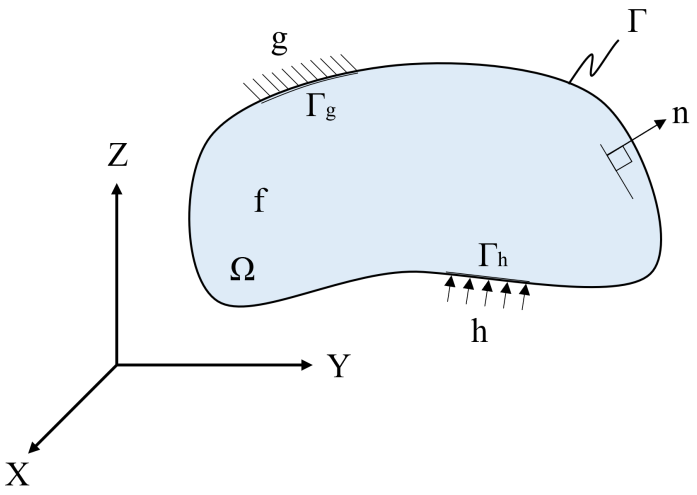

Figure 3.1 – Thermal boundary conditions schematic representation for heat transfer analysis.

Several boundary conditions are encountered in the heat transfer problems. A prescribed temperature thg is modeled by the Dirichlet boundary condition, given in Equation 3.1.

$$T\Big|_{\Gamma_T} = {}^{th}\,\mathrm{g} \tag{3.1}$$

The initial temperatures must be additionally defined for transient analysis.

$$T\Big|_{t=0} =^{th} \mathrm{g}_0 \tag{3.2}$$

Convective heat flux is modeled through the Neumann boundary conditions, in which a prescribed heat flux is imposed in a surface Γ_h of the body.

$$k\frac{\partial T}{\partial n}\Big|_{\Gamma_h} =^{th} \mathrm{h} \tag{3.3}$$

where, k is the body thermal conductivity, and n the unit normal vector pointing outwards the surface Γ_h.

The convective heat transfer is given in Equation 3.4:

$$q_{convection} = h_f(T_S - T_B) \tag{3.4}$$

where $q_{convection}$ is the convective heat flux, h_f is the film coefficient, T_B is the bulk temperature of fluid adjacent to the solid surface, and T_S is the temperature at the solid surface.

3.1.1 Strong and Weak Form for the Heat Transfer Boundary-Value Problem

Let q_i denote the Cartesian components of the heat flux vector, let T be the temperature and thf the heat supply per unit of volume. Assuming that the heat flux vector is defined in terms of temperature gradient according to the generalized Fourier law of heat conduction, given in Equation 3.5:

$$q_i = -\kappa_{ij}T_{,j} \tag{3.5}$$

where κ_{ij} is the conductive matrix, which assume the following form when the material is assumed to have isotropic conductivity:

$$\kappa_{ij}(x) = \kappa(x)\delta_{ij} \tag{3.6}$$

where δ_{ij} is the Kronecker delta.

Then, the strong form for the boundary-value heat conduction problem can be written as:

Given ${}^{th}\mathrm{f} : \Omega \to \mathbb{R}$; ${}^{th}\mathrm{g}_i : \Gamma_{g_i} \to \mathbb{R}$; ${}^{th}\mathrm{h}_i : \Gamma_{h_i} \to \mathbb{R}$, find $T \in \Omega$ such that

$$q_{i,i} =^{th} \mathrm{f}, \text{ in region } \Omega \tag{3.7}$$

$$T =^{th} \mathrm{g}, \text{ on surface } \Gamma_g \tag{3.8}$$

$$-q_i n_i =^{th} \mathrm{h}, \text{ on surface } \Gamma_h \tag{3.9}$$

where q_i is defined by Equation 3.5

where ${}^{th}\mathrm{g}$ and ${}^{th}\mathrm{h}$ are prescribed boundary temperature and heat flux, respectively. Equation 3.7 is a generalized Poisson Equation, 3.8 is a Dirichlet boundary condition and Equation 3.9 is a Neumann boundary condition.

The analytical solution for this problem is trivial. However, the main advantage of the finite element method is to propose an approximate solution for complex situations in which the exact solutions are not possible. The weak form of the problem is proposed to obtain such approximate solutions.

To define the weak form of the heat conduction problem, two new classes of functions must be introduced. The first set of functions ζ is called trial solution and satisfies the Dirichlet boundary conditions $u(1) =^{th} \mathrm{g}$. The second set ν of functions is called weighting functions, and they are the homogeneous counterpart of the Dirichlet boundary conditions $w(1) = 0$. The H^1-functions are the functions that belong to Hilbert space and satisfy Equation 3.10:

$$\int_0^1 (u_{,i})^2 dx < \infty \tag{3.10}$$

Then, the sets of trial solution and weighting functions can be defined as:

$$\begin{aligned} \zeta &= \{u | u \in H^1, u(1) =^{th} \mathrm{g}\} \quad \text{(trial solutions)} \\ \nu &= \{w | w \in H^1, w(1) = 0\} \quad \text{(weighting functions)} \end{aligned} \tag{3.11}$$

The corresponding weak form of the heat conduction problem is stated as:

Given ${}^{th}\mathrm{f} : \Omega \to \mathbb{R}$; ${}^{th}\mathrm{g}_i : \Gamma_{g_i} \to \mathbb{R}$; ${}^{th}\mathrm{h}_i : \Gamma_{h_i} \to \mathbb{R}$, find $u \in \Omega$ such that

$$-\int_{\Omega} w_{,i} q_i \, d\Omega = \int_{\Omega} w^{th}\mathrm{f} \, d\Omega + \int_{\Gamma_h} w^{th}\mathrm{h} \, d\Gamma_h \tag{3.12}$$

where q_i is defined by Equation 3.5

The Bubnov-Galerkin method can be used to obtain the approximate solution to the boundary-value problem given in the weak formulation. These collections of the approximation functions are denoted by ζ^h and ν^h, being subsets of ζ and ν, respectively.

$$\begin{aligned} &\zeta^h \subset \zeta \quad (\text{i.e., if } u^h \in \zeta^h, \text{ then } u^h \in \zeta) \\ &\nu^h \subset \nu \quad (\text{i.e., if } w^h \in \nu^h, \text{ then } w^h \in \nu) \end{aligned} \tag{3.13}$$

If $u^h \in \zeta$ and $w^h \in \nu$, then:

$$u^h(1) =^{th} \mathrm{g} \tag{3.14}$$

$$w^h(1) = 0 \tag{3.15}$$

Then, u^h can be written as:

$$u^h = w^h +^{th} \mathrm{g}^h \tag{3.16}$$

Which still meets the boundary conditions requirements:

$$\begin{aligned} u^h(1) &= w^h(1) +^{th} \mathrm{g}^h(1) \\ &= 0 +^{th} \mathrm{g} \end{aligned} \tag{3.17}$$

Then, the Bubnov-Galerkin form of the boundary-value problem can be written as:

Given ${}^{th}\mathrm{f}_i : \Omega \to \mathbb{R}$; ${}^{th}\mathrm{g}_i : \Gamma_{g_i} \to \mathbb{R}$; ${}^{th}\mathrm{h}_i : \Gamma_{h_i} \to \mathbb{R}$, find $u^h = v^h +^{th} \mathrm{g}^h \in \zeta^h$ such that for all $w^h \in \nu^h$,

$$\int_{\Omega} w^h_{,i} \, \kappa_{ij} \, v^h_{,j} \, d\Omega = \int_{\Omega} w^h \, {}^{th}\mathrm{f} \, d\Omega + \int_{\Gamma_h} w^h \, {}^{th}\mathrm{h} \, d\Gamma_h - \int_{\Omega} w^h_{,i} \, \kappa_{ij} \, {}^{th}\mathrm{g}^h_{,j} \, d\Omega \tag{3.18}$$

The approximation functions can be written in terms of the linear combination of the shape functions N, which have the following properties:

$$N_A(1) = 0, \qquad A = 1, 2, ..., n \tag{3.19}$$

And,

$$N_{n+1}(1) = 1 \tag{3.20}$$

Let the continuous domain Ω be discretized into the domain Ω^e which is composed by n_{el} elements, as seen in Figure 3.2.

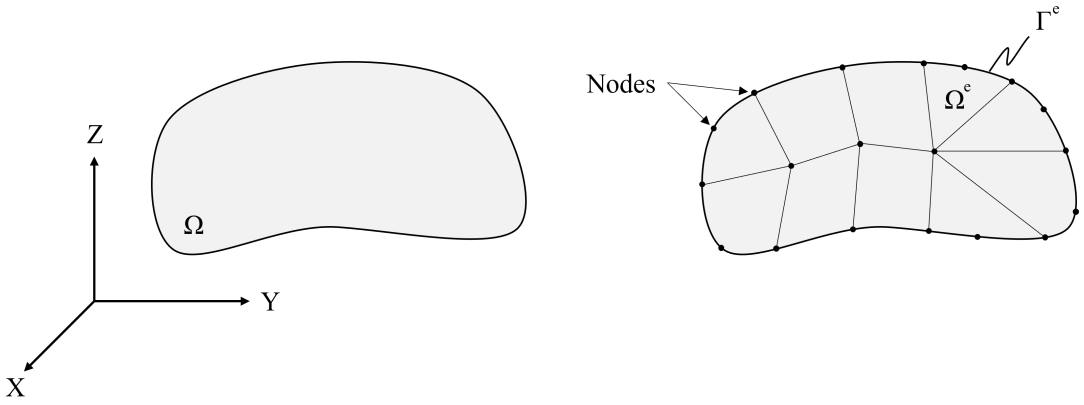

Figure 3.2 – Domain Ω discretization on element domains Ω^e.

Let $\eta = \{1, 2, ..., n_{np}\}$ be the set of global node numbers, n_{np} the number of nodes, $\eta_{g_i} \subset \eta$ be the set of nodes at which $u_i^h =^{th} \mathrm{g}_i$, and $\eta - \eta_{g_i}$ be the complement of η_{g_i}. The nodal values of u_i^h is to be determined for each node in $\eta - \eta_{g_i}$.

With these definitions, v_i^h, ${}^{th}\mathrm{g}_i^h$ and w_i^h can be written as:

$$w_i^h = N_{jA} c_A \ , \ A \in \eta - \eta_{g_i} \tag{3.21}$$

where N_A is the shape function associated with node number A and c_A a constant.

$$v_i^h = N_{jA} d_A \ , \ A \in \eta - \eta_{g_i} \tag{3.22}$$

where d_A is the unknown temperature at node A and

$${}^{th}\mathrm{g}_i^h = N_{jA} \, {}^{th}\mathrm{g}_A \ , \ A \in \eta_{g_i} \tag{3.23}$$

where ${}^{th}\mathrm{g}_i^h$ is the nodal interpolation of the prescribed temperature ${}^{th}\mathrm{g}$.

Replacing v_i^h, ${}^{th}\mathrm{g}_i^h$ and w_i^h in this form on the Bubnov-Galerkin form for the boundary-value problem yields the following Equation:

$$\int_\Omega N_{A,i}\,\kappa_{ij}\,N_{B,j}\,d\Omega\;\; d_{kB} = \int_\Omega N_A\,{}^{th}\mathrm{f}\,d\Omega + \int_\Gamma N_A\,{}^{th}\mathrm{h}\,d\Gamma - \int_\Omega N_{A,i}\,\kappa_{ij}\,N_{B,j}\,d\Omega\;\; {}^{th}\mathrm{g}_{jB}$$
$$A \in \eta - \eta_{g_i};\; B \in \eta_{g_j}$$
$$1 \leq i,j \leq n_{eq} \tag{3.24}$$

where n_{sd} is the number of space dimensions, n_{dof} the number of degrees of freedom, d_B are the unknown of this system of n_{dof} Equations, which can be written in a more concise form as:

$$\kappa_{ij} T_{,j} = q_i \tag{3.25}$$

where κ_{ij} is the conductive matrix, $T_{,j}$ the temperature vector, and q_i the heat flux vector, as shown below:

$$\begin{aligned}
\kappa_{ij} &= \int_\Omega N_{A,i}\,\kappa_{ij}\,N_{B,j}\,d\Omega \\
T_{,j} &= d_{kB} \\
q_i &= \int_\Omega N_A\,{}^{th}\mathrm{f}\,d\Omega + \int_\Gamma N_A\,{}^{th}\mathrm{h}\,d\Gamma - \int_\Omega N_{A,i}\,\kappa_{ij}\,N_{B,j}\,d\Omega\;\; {}^{th}\mathrm{g}_{lF}
\end{aligned} \tag{3.26}$$

The global stiffness matrix and force vector are defined as the sum of the elemental contributions, given on Equations 3.27 and 3.28 and schematically represented in Figure 3.3.

$$\kappa_{ij} = \sum_{e=1}^{n_{el}} \kappa_{ij}^e = \int_\Omega N_{A,i}\,\kappa_{ij}\,N_{B,j}\,d\Omega \tag{3.27}$$

$$q_i = \sum_{e=1}^{n_{el}} q_i^e = \int_{\Omega^e} N_A\,{}^{th}\mathrm{f}\,d\Omega + \int_{\Gamma^e} N_A\,{}^{th}\mathrm{h}\,d\Gamma - \int_{\Omega^e} N_{A,i}\,\kappa_{ij}\,N_{B,j}\,d\Omega\;\; {}^{th}\mathrm{g}_{jB} \tag{3.28}$$

The solution of Equation 3.25 demands the solution of the integrals showed on Equation 3.26, which can be efficiently done by a numerical integration (quadrature) method. However, this method demands an integration over the domain [-1, 1]. The finite element method proposes a local domain which is defined to meet this requirement, and the integrals showed in Equation 3.26 are solved in this local domain. This solution

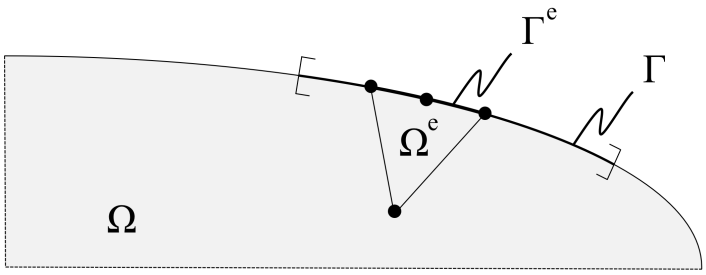

Figure 3.3 – Schematic illustration of the elemental form of Γ^e.

approach demands a coordinate change which maps the global coordinates to the local ones.

The relation of the local coordinates ξ_i to global coordinates $\mathbf{x}_i$ (and vice-versa) is given in Equation 3.29.

$$\mathbf{x}_i(\xi_j) = N_a(\xi_j)\mathbf{x}^e_{ia} \; ; \; a = 1, ..., 4 \tag{3.29}$$

Figure 3.4 show the schematic local and global domains for a quadrilateral element.

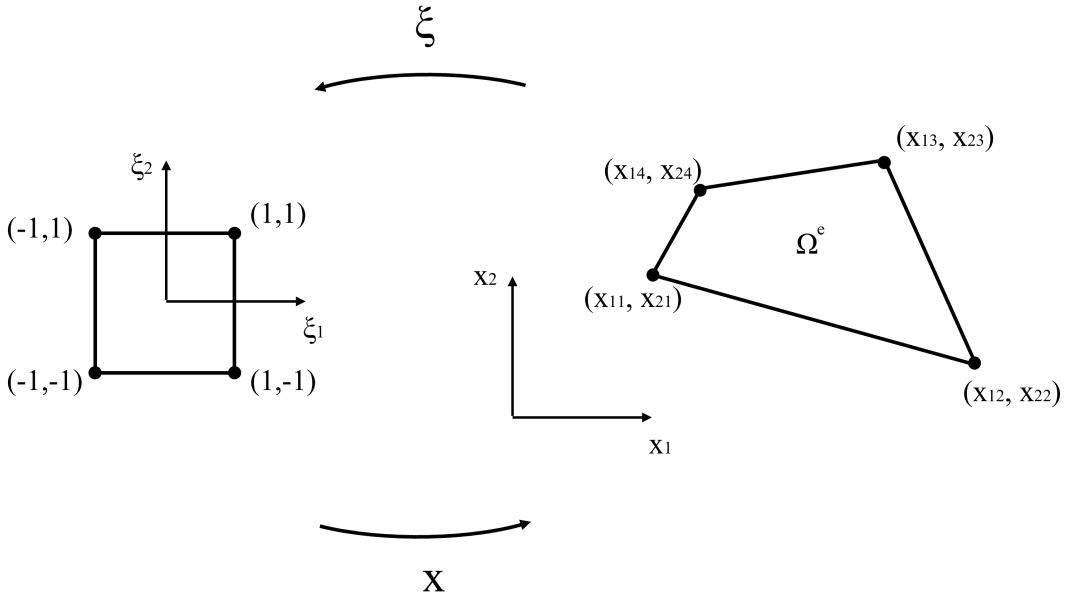

Figure 3.4 – Schematic local and global domains for a quadrilateral element in two-dimensional space.

If the N_a function used in the mapping is the same used in the element shape

function given in Equation 3.29, the element is said to be isoparametric.

The boundary-value problem can be solved using one of the several commercial finite element codes available to obtain the approximate solution.

More information about the strong and weak form for the heat transfer boundary-value problem can be found in [Hughes, 1987; Bathe, 2019].

3.2 Inverse Heat Transfer Problem

In a classical heat transfer problem, the temperature field is the unknown quantity that relies on the known parameters of the material and boundary conditions (initial-value problem). The inverse heat transfer method consists in the numerical determination of the input information of a classical heat transfer problem, such as unknown boundary conditions [Reinhardt et al., 2007] or initial temperature distribution [Pereverzyev et al., 2008] of a given thermal system through the utilization of temperature history experimental measurements. The numerical determination of the boundary conditions can be done by a numerical optimization, in which the deviation of the calculated temperature from the measured temperature is minimized by changing the convective heat transfer coefficients in the calculation. Thus, an appropriate numerical optimization method must be used to find the set of inputs - convective heat transfer coefficients - which results in the global minimum value of the cost function for a given set of restrictions.

The numerical optimization problem to be solved is stated in the following form:

Find x that minimizes the cost function f

$$\min_{x} f(x) \tag{3.30}$$

subjected to the constraints g_k and h_k:

$$Cg_k(\{x\}) \leq 0 \; \forall \; k = 1, 2, ..., K \tag{3.31}$$

$$Ch_l(\{x\}) = 0 \; \forall \; l = 1, 2, ..., L \tag{3.32}$$

This problem can be solved using several optimization algorithms. However, the result quality may be significant different depending on the utilized solver. Ansys DesignXplorer module is capable to solve the optimization problem, as it is already integrated with the finite element solver. The procedure based on this solver package was chosen

since it is the commercial package available to solve the multiphysics problem. Among the options, the Adaptive single-objective (ASO) algorithm was chosen due to its capabilities of global search for minimum value for a single objective cost function.

3.2.1 Adaptive Single-Objective

The adaptive single-objective (ASO) algorithm combines and optimal space-filling (OSF) design of experiment (DOE), a Kriging response surface and a mixed-integer sequential quadratic programming (MISQP). It consists in a gradient-based algorithm which provides a global optimized result based on a surface response.

The ASO schematic workflow is given in Figure 3.5.

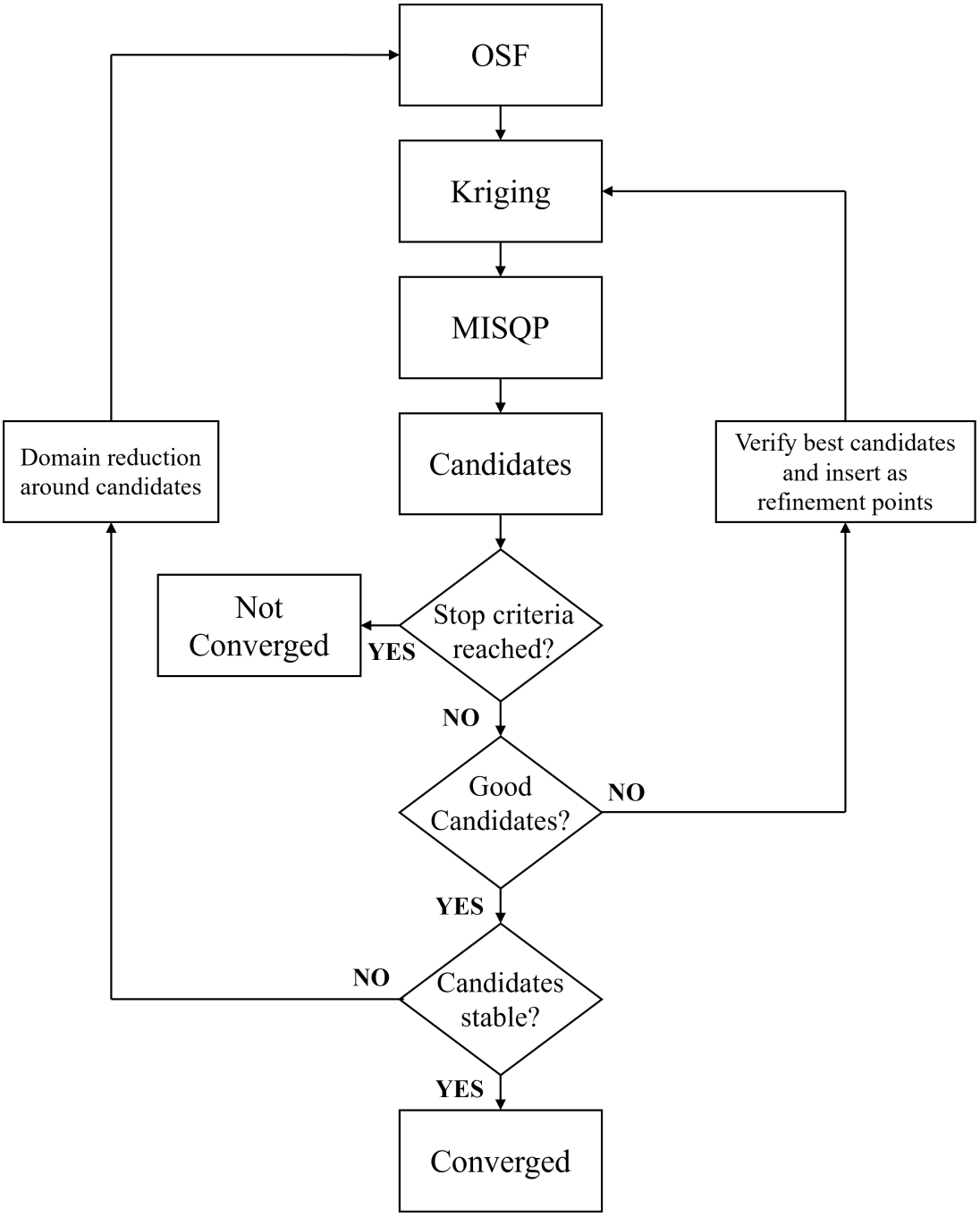

Figure 3.5 – ASO algorithm schematic workflow.

ASO algorithm can be divided in the following macro steps:

a) OSF Sampling

OSF sampling is used for the Kriging construction. The number of samples is equal to the number of divisions per axis. One sample is set at each division, in order to fill the solution space. When a new OSF is generated, the new reduced OSF have the same number of divisions as the original OSF within the new reduced bounds. New

design points are added until there is a point at each division of the new domain. Figure 3.6 schematically represents this routine.

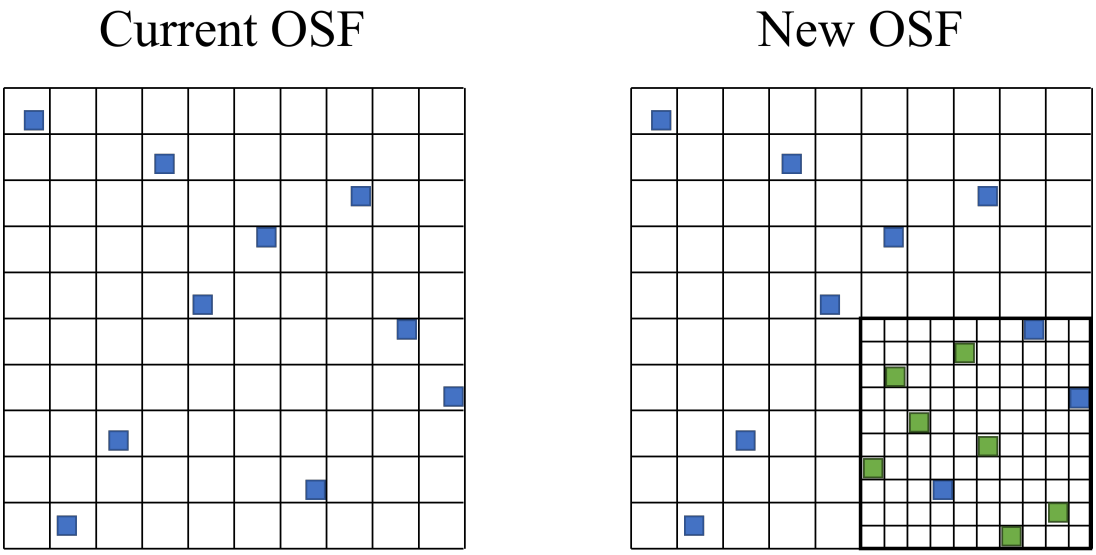

Figure 3.6 – OSF schematic domain reduction.

b) Kriging Generation

a response surface is created for each output, based on the current OSF and its boundaries. The response surface is created by a combination of a polynomial model plus departures of the form given by Equation 3.33:

$$Ky(x) = Kf(x) + KZ(x) \tag{3.33}$$

where, $Ky(x)$ is the unknown function of interest, $Kf(x)$ is a polynomial function of x and $KZ(x)$ is the realization of a random Gaussian normal distribution with mean equals to zero and non-zero covariance. More information about Kriging algorithm on the original article [Krige, 1951].

c) MISQP

MISQP is run on the current Kriging response surface to find potential candidates. MISQP solves mixed-integer nonlinear programming problems by a modified sequential quadratic programming (SQP) method. More information about this method can be found in [Exler and Schittkowski, 2006].

d) Candidates Point Validation

all the obtained candidate points are either validated or not, based on the Kriging error predictor. Then, the candidate is checked to validate if its selection would change with further domain refinement. A candidate is considered acceptable when there is no other potential better candidate, according to the error predictor. If that is the case, a further domain refinement is done. Otherwise, the other potential candidate is calculated as a verification point.

3.3 Mechanical Problem

The general elasticity problem to be solved is defined considering a three-dimensional body which occupies the domain Ω and is surrounded by surfaces Γ, such as the one showed in Figure 3.1. The body is fixed in the coordinate system X, Y, Z by the prescribed displacements ^{me}g applied on the surface area Γ_g and it is subjected to surface tractions ^{me}h on the surface area Γ_h. Additionally, the body is subjected to prescribed body forces per unit of volume ^{me}f.

Let u_i the displacement vector and ε the infinitesimal strain tensor, defined in Equation 3.34.

$$\varepsilon_{ij} = \frac{u_{i,j} + u_{j,i}}{2} \tag{3.34}$$

The Cauchy stress tensor σ_{ij} is defined in terms of the strain tensor by the generalized Hooke's law, given in Equation 3.35:

$$\sigma_{ij} = C_{ijkl}\varepsilon_{kl} \tag{3.35}$$

where C_{ijkl} is the elasticity tensor.

3.3.1 Elastic Strain

The total strain for viscoplastic problems with thermal loads can be decomposed as the sum of thermal ε^{th}, elastic ε, plastic ε^{pl}, and creep ε^{cr} strains. Thus, the elastic strain vector can be written as:

$$\varepsilon_{ij} = \varepsilon_{kl}^{total} - \varepsilon_{mn}^{th} - \varepsilon_{op}^{pl} - \varepsilon_{qr}^{cr} \tag{3.36}$$

3.3.2 Thermal Strains

The thermal strain ε^{th} for isotropic materials is evaluated using Equation 3.37:

$$\varepsilon^{th}_{mn} = \Delta T \alpha^{se}_{ij} \delta_{ij} \tag{3.37}$$

where ΔT is the temperature difference from instantaneous temperature to zero thermal strain temperature and α^{se} is the Secant coefficient of thermal expansion.

3.3.3 Creep Strain: Rate-Dependent Plasticity

Creep deformation can be represented in the incremental form through the creep strain rate formulation. A hardening creep rate model was chosen for having parameters for stress level, temperature and time, and due to its compatibility for parallel usage with the other chosen material models. The hardening creep strain rate Equation is given in Equation 3.38.

$$\dot{\varepsilon^{cr}} = C_1 \sigma^{C_2} t^{C_3} e^{-\frac{C_4}{T}} \tag{3.38}$$

where $\dot{\varepsilon}_{cr}$ is the creep strain rate, C_1 to C_4 are material constants, σ is the equivalent stress, t is the time at the end of the substep, e is the natural logarithm base and T is the absolute temperature. The material constants must be defined to fit the numerical response to the experimental data.

More information about the time hardening creep model can be found in [ANSYS, 2022].

3.3.4 Plastic Strain: Rate-Independent Plasticity

The plastic strain ε^{pl} is evaluated using a plasticity model, which is used to represent the non-linear behavior exhibited by some materials when loaded beyond their elastic limits, where a nonrecoverable plastic strain develops. Figure 3.7 shows the typical material behavior under such conditions.

When a load σ' beyond the yield stress σ_y is applied an associated total strain ε' arises. The plastic strain development is given by the plasticity model. The multi-linear isotropic hardening model was chosen among the implemented plasticity model on Ansys

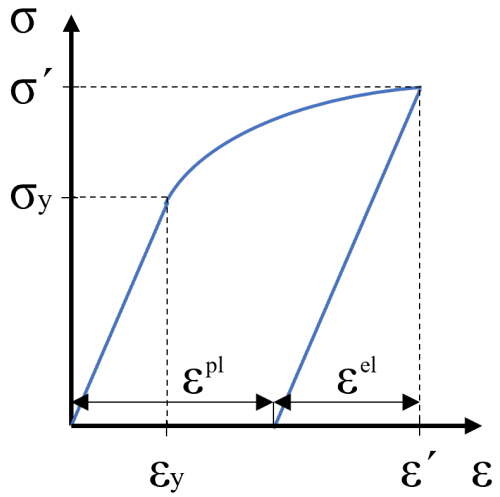

Figure 3.7 – Schematic non-linear stress versus strain curve.

APDL due to the simplicity of its formulation and as there is no intent to model cyclical loads.

3.3.4.1 Isotropic Hardening Rule

The change in the yield criterion due to the loading level is called hardening. The isotropic hardening model can represent the material behavior under monotonic loading and elastic unloading. When the material exceeds its elastic limit, the isotropic hardening causes a uniform increase in the size of the yield surface and an increase in the yield stress. The isotropic hardening rule is given below on its general formulation.

$$F(\sigma) - \sigma_y(\xi') = 0 \tag{3.39}$$

where $F(\sigma)$ is a scalar function of stress and $\sigma_y(\xi)$ is the yield stress dependent of a set ξ' of history dependent internal variables.

A stress increase from $F(\sigma(t_1))$ to $F(\sigma(t_2))$, beyond the elastic limit, increases the yield stress by an uniform increase in the size of the yield surface, as illustrated in Figure 3.8.

The flow stress curve is described by a piece-wise linear stress-plastic strain curve, the Multilinear Isotropic Hardening model (MISO), presented in Figure 3.9, where E is the modulus of elasticity. The first point corresponds to the yield stress and the subsequent

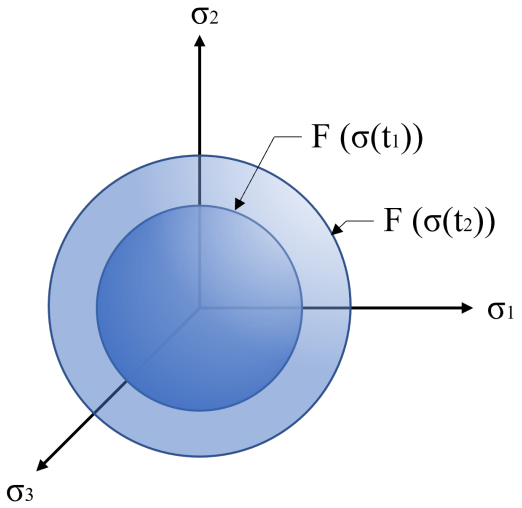

Figure 3.8 – Yield surface increase illustration.

points correspond to the material elastic plastic response.

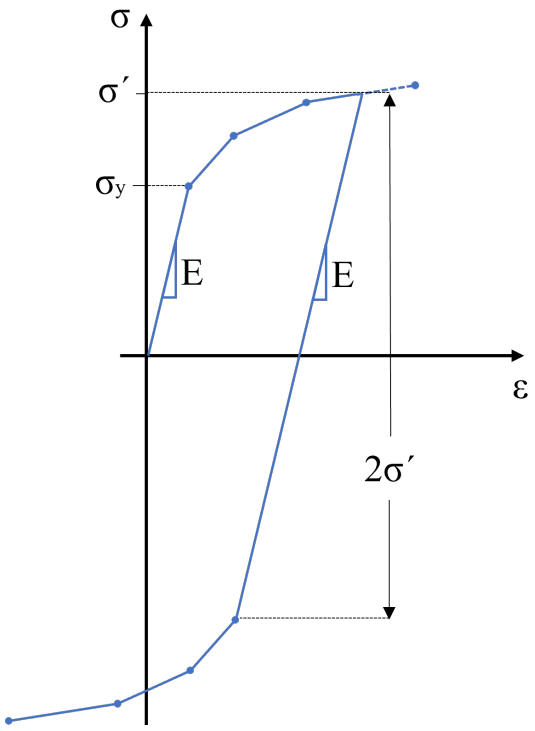

Figure 3.9 – Multilinear isotropic hardening model schematic representation.

The von Mises yield criterion is widely used in the plasticity models to verify if the material exceeded its elastic limit, and is given on its general form on Equation 3.40:

$$f(\sigma, \sigma_y) = \sigma_e - \sigma_y = 0 \tag{3.40}$$

where σ_y is the yield stress in uniaxial stress loading and σ_e is the von Mises equivalent stress, defined in Equation 3.41:

$$\sigma_e = \sqrt{\frac{3}{2}\left(\sigma_{ij}\sigma_{ij} - \frac{1}{3}(\sigma_{kk})^2\right)} \tag{3.41}$$

This results in a cylindrical yield surface in the principal stress space, and a yield criterion independent of the hydrostatic stress, as shown in Figure 3.10.

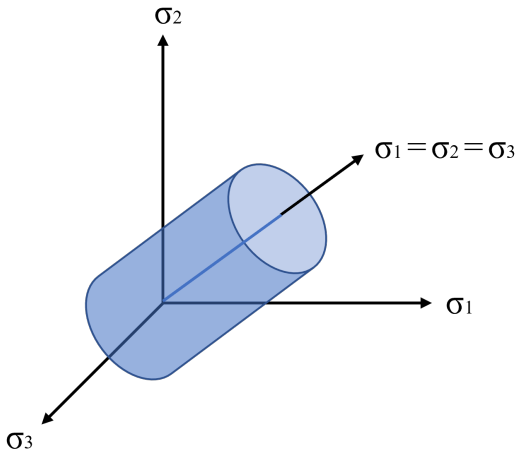

Figure 3.10 – Von Mises yield surface illustration.

The evolution of the plastic strain is determined by the flow rule, given in Equation 3.42.

$$d\varepsilon^{pl} = d\lambda \frac{\partial Q}{\partial \sigma} \tag{3.42}$$

where λ is the magnitude of the plastic strain increment and Q is the plastic potential.

For an associated flow rule, the plastic potential is equal to the yield criterion given in Equation 3.40, the plastic strain increment is normal to the yield surface and proportional to the deviatoric stress. The associated flow rule is given in Equation 3.43 .

$$d\varepsilon^{pl} = \left(\sigma - \frac{1}{3}\sigma_{kk}\right) \tag{3.43}$$

More information about plasticity models can be found in [Jean and Chaboche,

2009].

3.3.5 Strong and Weak Forms of the Linear Elastostatics Equilibrium Boundary-Value Problem

The strong form of the liner elastic static equilibrium boundary-problem is given below:

Given ${}^{me}\mathrm{f}_i : \Omega \to \mathbb{R}$; ${}^{me}\mathrm{g}_i : \Gamma_{g_i} \to \mathbb{R}$; ${}^{me}\mathrm{h}_i : \Gamma_{h_i} \to \mathbb{R}$, find $u_i : \Omega \to \mathbb{R}$ such that the set of Equations 3.44 are fulfilled.

$$\begin{aligned} &\sigma_{ij,i} + {}^{me}\,\mathrm{f}_i = 0, \text{ in } \Omega \\ &u_i = {}^{me}\,\mathrm{g}, \text{ on surface } \Gamma_g \\ &\sigma_{ij,i} n_j = {}^{me}\,\mathrm{h}_i, \text{ on surface } \Gamma_{h_i} \end{aligned} \tag{3.44}$$

where u_i is the displacement, ${}^{me}\mathrm{f}_i$ the prescribed body force per unit of volume, ${}^{me}\mathrm{g}$ the prescribed boundary displacements, n_j the vector normal to the surface, and ${}^{me}\mathrm{h}_i$ the prescribed boundary tractions.

The weak form of the static equilibrium is stated in Equation 3.45 using the sets of trial solution and weighting functions similar to the ones defined on the boundary-value heat conduction problem.

Given ${}^{me}\mathrm{f}_i : \Omega \to \mathbb{R}$; ${}^{me}\mathrm{g}_i : \Gamma_{g_i} \to \mathbb{R}$; ${}^{me}\mathrm{h}_i : \Gamma_{h_i} \to \mathbb{R}$, find $u_i \in \zeta$ such that for all $w_i \in \nu_i$,

$$\begin{aligned} &\int_\Omega w_{(i,j)} \sigma_{ij} d\Omega = \int_\Omega w_i \, {}^{me}\mathrm{f}_i d\Omega + \sum_{i=1}^{n_{sd}} \left(\int_{\Gamma_{h_i}} w_i \, {}^{me}\mathrm{h}_i d\Gamma \right) \\ &\sigma_{ij,i} n_j = {}^{me}\,\mathrm{h}_i, \text{ on surface } \Gamma_{h_i} \end{aligned} \tag{3.45}$$

this formulation is also known as virtual work, where the w are the virtual displacements.

The Bubnov-Galerkin method is used to obtain the approximate solution to the boundary-value problem given in the weak formulation, analogously to boundary-value heat conduction problem, yielding the following Equations.

Given ${}^{me}\mathrm{f}_i : \Omega \to \mathbb{R}$; ${}^{me}\mathrm{g}_i : \Gamma_{g_i} \to \mathbb{R}$; ${}^{me}\mathrm{h}_i : \Gamma_{h_i} \to \mathbb{R}$, find $u^h = v^h + {}^{me}\,\mathrm{g}^h \in \zeta^h$ such that for all $w^h \in \nu^h$,

$$\int_\Omega w^h_{,i}\, D_{ij}\, v^h_{,j}\, d\Omega = \int_\Omega w^h\, {}^{me}\mathrm{f} dx + \int_\Gamma w^h\, {}^{me}\mathrm{h}\, d\Gamma - \int_\Omega w^h_{,i}\, D_{ij}\, {}^{me}\mathrm{g}^h_{,j}\, d\Omega \tag{3.46}$$

where Dij is the stiffness matrix.

With these definitions, v^h, ${g^h}_i$ and w^h can be written as:

$$\begin{aligned} v^h_i &= v^h_i e_i \\ &= \left(\sum_{A \in \eta - \eta_{g_i}} N_A d_{iA} \right) e_i \text{ (no sum on } i) \end{aligned} \tag{3.47}$$

$$\begin{aligned} {}^{me}\mathrm{g}^h_i &= {g^h}_i e_i \\ &= \left(\sum_{A \in \eta_{g_i}} N_A g_{iA} \right) e_i \text{ (no sum on } i) \end{aligned} \tag{3.48}$$

$$\begin{aligned} w^h_i &= {w^h}_i e_i \\ &= \left(\sum_{A \in \eta - \eta_{g_i}}^{n} N_A c_{iA} \right) e_i \text{ (no sum on } i) \end{aligned} \tag{3.49}$$

where i is the degree of freedom number, A is the global node number, and e_i the ith Euclidean basis vector.

Replacing v^h, ${}^{me}\mathrm{g}^h_i$ and w^h - defined respectively in Equations 3.47, 3.49 - in this form on the Bubnov-Galerkin form for the boundary-value problem yields Equation

$$\begin{aligned} \sum_{j=1}^{n_{dof}} \left(\sum_{B \in \eta - \eta_{g_j}} \int_\Omega (N_A e_i)_{,i}\, D_{ij}\, (N_B e_j)_{,j}\, d\Omega\, d_{jB} \right) &= \int_\Omega N_A e_i\, {}^{me}\mathrm{f}\, d\Omega + \int_\Gamma N_A e_i\, {}^{me}\mathrm{h}\, d\Gamma \\ &\quad - \sum_{j=1}^{n_{dof}} \left(\sum_{B \in \eta_{g_j}} \int_\Omega (N_A e_i)_{,i}\, D_{ij}\, (N_B e_j)_{,j}\, d\Omega\, g_{jB} \right) \\ &\quad A \in \eta - \eta_{g_i},\ 1 \le i \le n_{sd} \end{aligned} \tag{3.50}$$

where n_{sd} is the degree of freedom per node.

The n_{dof} value of displacements d_B are the unknown of this system of n_{dof} Equations, which can be written in a more concise form as:

$$D_{PQ} d_Q = F_P \tag{3.51}$$

where D_{ij} is the stiffness matrix, $u_j i$ the displacement vector, and F_i the force vector, as shown below:

$$\begin{aligned} K_{PQ} =& \int_\Omega (N_A e_i)_{,i} \, D_{ij} \, (N_B e_j)_{,j} \, d\Omega \\ d_Q =& d_{jB} \\ F_P =& \int_\Omega N_A e_i \, {}^{me}\mathrm{f} \, d\Omega + \int_\Gamma N_A e_i \, {}^{me}\mathrm{h} \, d\Gamma \\ & - \sum_{j=1}^{n_{dof}} \left(\sum_{B \in \eta_{g_j}} \int_\Omega (N_A e_i)_{,i} \, D_{ij} \, (N_B e_j)_{,j} \, d\Omega \, g_{jB} \right) \\ P =& ID(i, A), \quad Q = ID(j, B) \end{aligned} \tag{3.52}$$

The indexes P and Q are defined through the ID array, given in Equation 3.53.

$$ID(i, A) = \begin{cases} P_{ID} & if \ A \in \eta - \eta_{g_i} \\ 0 & if \ A \in \eta_{g_i} \end{cases} \tag{3.53}$$

where $1 \leq i \leq n_{dof}$ and P_{ID} the global Equation number. The first argument of the ID array is the degree of freedom number, while the second argument is the global node number. ID array has the dimension $n_{dof} \times n_{np}$.

The set of Equations given in 3.26 can be solved using the local solution approach proposed in the finite element method, analogously to the one described on chapter 3.1.1, using one of the several commercial finite element codes available to obtain the approximate solution for displacements in a given boundary-value problem.

More information about the strong and weak forms of the linear elastostatics equilibrium boundary-value problem can be found in [Hughes, 1987; Bathe, 2019].

3.4 Fatigue Failure Problem

A simple fatigue assessment can be realized by the comparison of the resulting stress amplitude σ_a, defined in Equation 3.54, to the fatigue strength for a fully reversible

loading σ_f, given in the Wöhler curve. A mean stress correction must be done in the cases in which $R \neq -1$ or in the cases in which a non-zero mean stress σ_m - defined in Equation 3.55 - is present, as the Wöhler curve data is given for a load ratio R - defined in Equation 3.56 - equals to -1.

$$\sigma_a = \frac{\sigma_{max} - \sigma_{min}}{2} \tag{3.54}$$

$$\sigma_m = \left| \frac{\sigma_{max} + \sigma_{min}}{2} \right| \tag{3.55}$$

$$R = \frac{\sigma_{min}}{\sigma_{max}} \tag{3.56}$$

Several attempts have been made to propose a general prediction of the mean stress effect in fatigue [SUSMEL et al., 2005]. Most of them are variations of the m, n and f coefficients of Martin's general Equation [Marin, 1956], given in Equation 3.57.

$$\left(\frac{\sigma_a}{\sigma_f}\right)^n + \left(f\frac{\sigma_m}{\sigma_{UTS}}\right)^m = 1 \tag{3.57}$$

where, σ_a is the load amplitude, σ_f the fatigue limit for a fully reversible loading, σ_m the mean load, σ_{UTS} the tensile ultimate strength and f, m and n are the fatigue model parameters.

Gerber's parabola is obtained by setting $n = 1$, $m = 2$ and $f = 1$, yielding Equation 3.58.

$$\sigma_a = \sigma_f \left[\left(1 - \frac{\sigma_m}{\sigma_{UTS}} \right)^2 \right] \tag{3.58}$$

The endurance safety factor SF_e can be evaluated assuming a constant load ratio R, given by Equation 3.59 and schematically represented in Figure 3.11.

$$SF_e = \frac{\bar{AC}}{\bar{AB}} = \frac{\sqrt{(1 - {\sigma_m}'^2)^2 + {\sigma_m}'^2}}{\sqrt{\sigma_a^2 + \sigma_m^2}} \tag{3.59}$$

von Mises equivalent stress σ_{vm}, defined in Equation 3.60 can be used in the multiaxial stress cases to obtain an equivalent stress which can be compared to the uniaxial stress data.

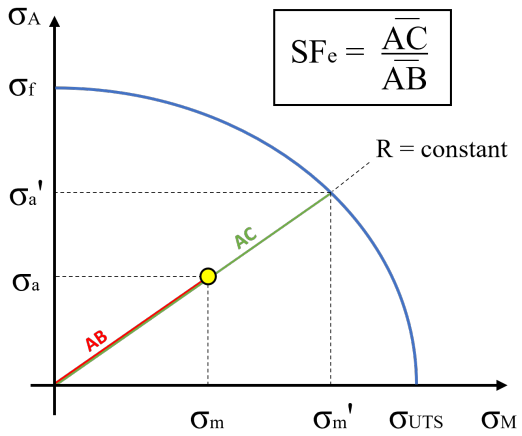

Figure 3.11 – Endurance safety factor SF_e schematic representation.

$$\sigma_{vm} = \sqrt{\frac{1}{2}\left[(\sigma_{11}-\sigma_{22})^2 + (\sigma_{22}-\sigma_{33})^2 + (\sigma_{33}-\sigma_{11})^2 + 6(\sigma_{23}^2+\sigma_{31}^2+\sigma_{12}^2)\right]} \tag{3.60}$$

More information about uniaxial fatigue models and mean stress correction can be found in [Budynas et al., 2021].

4 METHODOLOGY

The main objective of the present work is to propose a method capable of predicting the residual stress formation due to the cylinder manufacturing processes and its influence on the bench test endurance performance. To accomplish that, it is necessary to evaluate the thermal history on the components during the thermal treatment and the residual stress resulting from it, including creep phenomenon. Then, a fatigue model is used to numerically evaluate the endurance safety factors (SF_e) for the bench test load with and without the influence of the calculated residual stress. Finally, both numerical approaches are compared with the fatigue experimental data. This methodology is presented in detail in the following.

Figure 4.1 shows the schematic diagram of the proposed methodology. Initially, experimental cooling curves were obtained by installing thermocouples in the parts submitted to the thermal treatment. The temperature curves were used as input in the inverse heat transfer coefficient (IHTC) method and later to verify the resulting temperature history in the numerical model. The inverse heat transfer coefficient problem was solved by using a numerical optimization of the convection heat transfer coefficients applied to a thermal finite element model. The cost function utilized was the difference between the model response and the experimental data. The output of the optimization was the convective heat transfer curves which best represent the measured experimental data for the proposed thermal model.

The same thermal finite element model was used to calculate the temperature history in the treated part using the convective heat transfer coefficients found in the solution of the inverse heat transfer problem as boundary conditions. The numerical solution was compared to the experimental data to verify the model's accuracy. The temperature history was then imported into a mechanical finite element model, where the appropriate material models were used to calculate the formation and relaxation of the residual stress during the heat treatment process and subsequent machining.

The part is finally submitted to a fatigue bench test in which a pulsating load is applied. The part must sustain a specified number of cycles without presenting any fatigue failures to be approved in the given test. A numerical model of the bench test was used to calculate the alternate and mean stresses in the part during the load application cycle.

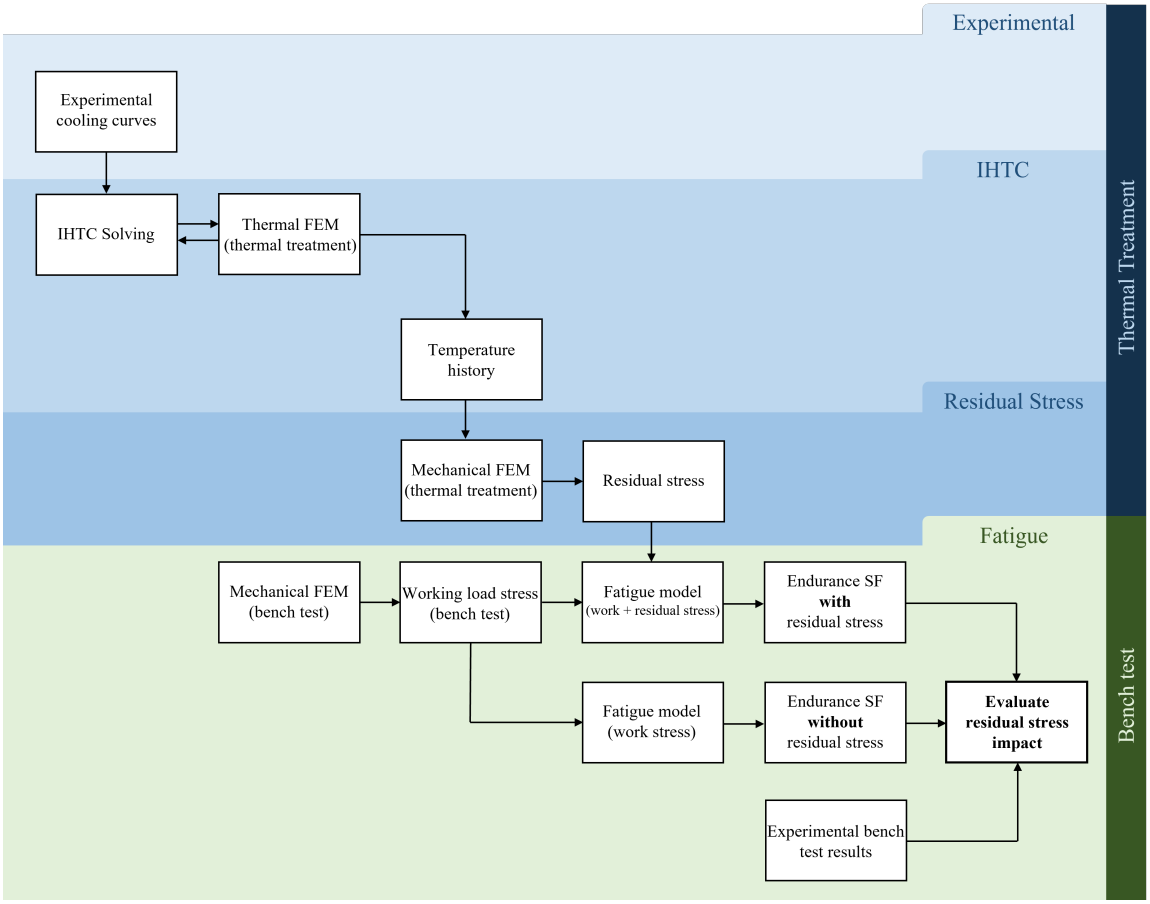

Figure 4.1 – Calculation diagram.

These stresses were then used in a fatigue model to calculate the SF_e with and without residual stress consideration. Both results were then compared to the experimental fatigue failures seen in the bench test to evaluate the impact of the residual stress in the SF_e and if the prediction accuracy was improved by the consideration of the residual stress.

The proposed methodology is divided and further analyzed in the four sections listed below:

- Experimental measurements.
- Solution of the inverse heat transfer coefficient problem.
- Residual stress calculation.
- Bench test simulation and fatigue assessment.

4.1 Experimental measurements

The aim of the temperature history measurements is to use them as part of the cost function in the optimization problem solved in the inverse heat transfer coefficient method and for the verification of the numerical thermal model.

The temperature history was measured in the parts during the T6 thermal treatment. During the treatment, the parts are confined in a furnace at elevated temperatures and submerged in water, so the measurement instrument must be adequate for such conditions. Thermocouples were used due to their resistance to water submersion and flexibility to installation in confined spaces. As high cooling rates are created within the part during quenching, it is desirable to use thermocouples with the low response time to accurately represent the cooling rate. Among the available thermocouples, the 1 mm diameter, type-J with inox 304 sheath thermocouple was chosen due to its resistance to the elevated furnace temperatures, water submersion, and low response time.

The used data acquisition device is compatible with type-J thermocouples and have eight channels for parallel measurement. Despite of the capability for higher acquisition rates, a 10 Hz rate was considered a good trade-off between an accurate representation of the highest cooling rates and excessive data writing and processing. More acquisition channels could be beneficial to the heat transfer coefficients calibration and numerical model verification; however, the usage of channels was limited by the available data acquisition device.

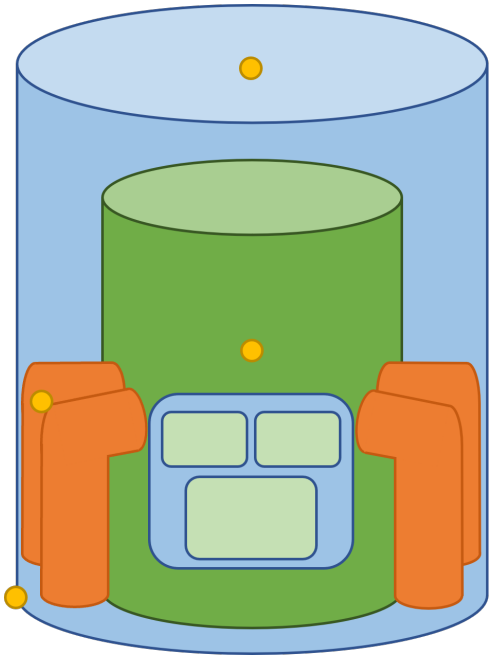

Figure 4.2 – Schematic representation of the measurement locations.

Four measurement points were measured in two cylinders (referred as experimental A and B) at the same time to increase the reliability of the measurements (Figure 4.2). The measurement points were defined in regions where different cooling rates were expected, aiming to get the optimal representation of the thermal gradients with the available number of data acquisition channels. The data acquisition device has built-in capability of data filtering; however, it was chosen to use no filtering during the data acquisition, as the cooling rates have great significance for the proposed work and the filtering could significantly modify the cooling rates.

4.2 Determination of the Heat Transfer Coefficients

The temperature history during the thermal treatment was calculated using a transient thermal analysis, in which the heat transfer was calculated through a convective model. However, the convective heat transfer coefficients $h_{convection}$ were previously unknown for the different thermal treatment processes. The heat flux during quenching was modeled through a simplification of the boiling curve, as proposed by [Faghri and Zhang, 2006], as the part is submerged into water in a temperature that greatly exceeds the water boiling temperature. Figure 4.3 shows the comparison of the boiling curve and the adopted simplified boiling curve.

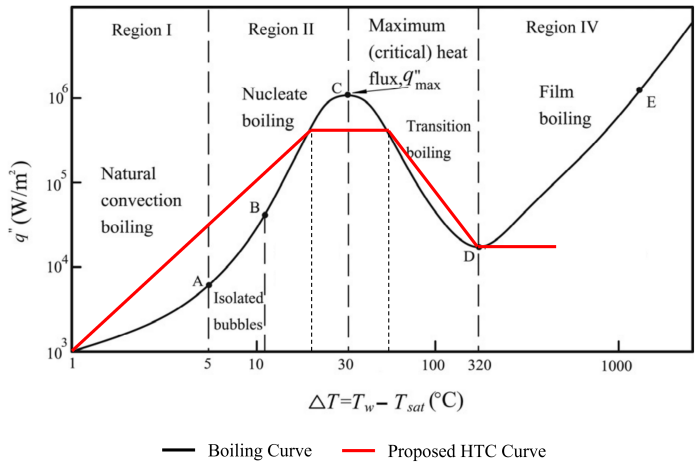

Figure 4.3 – Proposed temperature dependent convective heat transfer coefficient curve and boiling curve (adapted from [Faghri and Zhang, 2006]).

An inverse heat transfer coefficient method was used determine the heat transfer coefficients during the quenching. The method consists in minimizing the difference between the calculated temperature and the measured temperature on specific regions at specific instants. The variables to be optimized are the h_1, to h_3 coefficients, which define the proposed temperature-dependent convective heat transfer coefficient curve presented in Figure 4.4, assuming water boiling temperature at 100 °C.

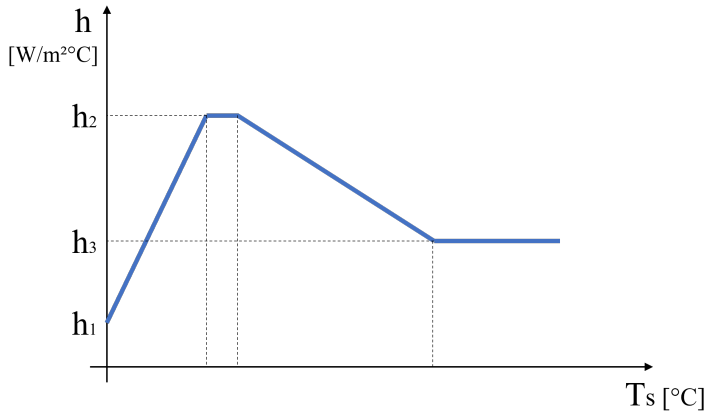

Figure 4.4 – Temperature dependent convective heat transfer coefficient curve.

Different heat transfer conditions may result in different regions, mainly due to freshwater flow restrictions. The surfaces where similar heat transfer conditions are expected were grouped in three sets and a heat transfer coefficient curve was assigned to each of them, as schematically shown in Figure 4.5.

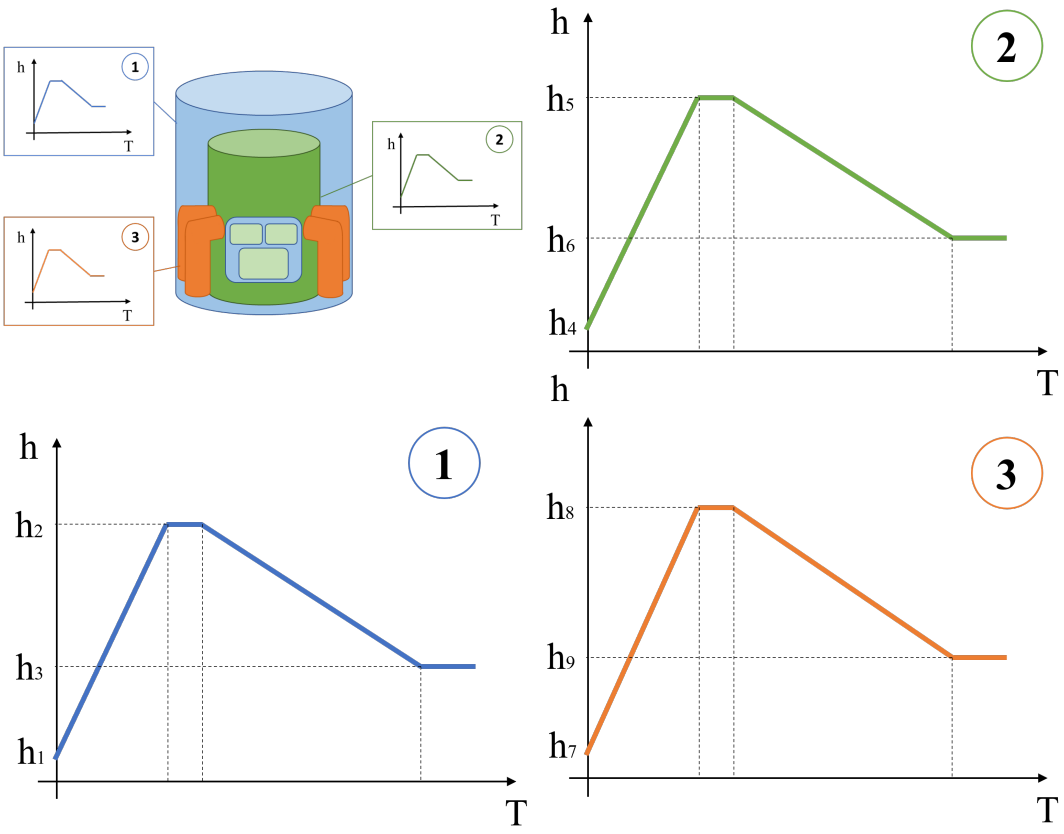

Figure 4.5 – Convective heat transfer coefficient curve assignment.

The optimization of the 9 parameters used to define the three curves were found by solving the inverse heat transfer coefficient problem using the adaptive single-objective (ASO) algorithm available in the parametric optimization module on Ansys Workbench. An initial population of 57 candidate points was used with 20 domain reductions, resulting in a maximum of 237 candidate point evaluations.

The cost function $f(h_1, h_2, ..., h_9)$ given in Equation 4.1 was defined as the sum of the squared difference of the calculated temperature T_{calc} from the experimental temperature T_{exp} at the four thermocouples locations L on ten time instants t, resulting in the verification of 40 temperatures per calculation. The instants were defined with higher density on the initial part of the cooling curve to have a higher weight on the optimization. This definition was adopted as there is a greater interest in having an accurate result in the initial instants, when the higher thermal gradients occur. The chosen experimental temperatures T_{exp} used as targets on the cost function are highlighted in Figure 4.6.

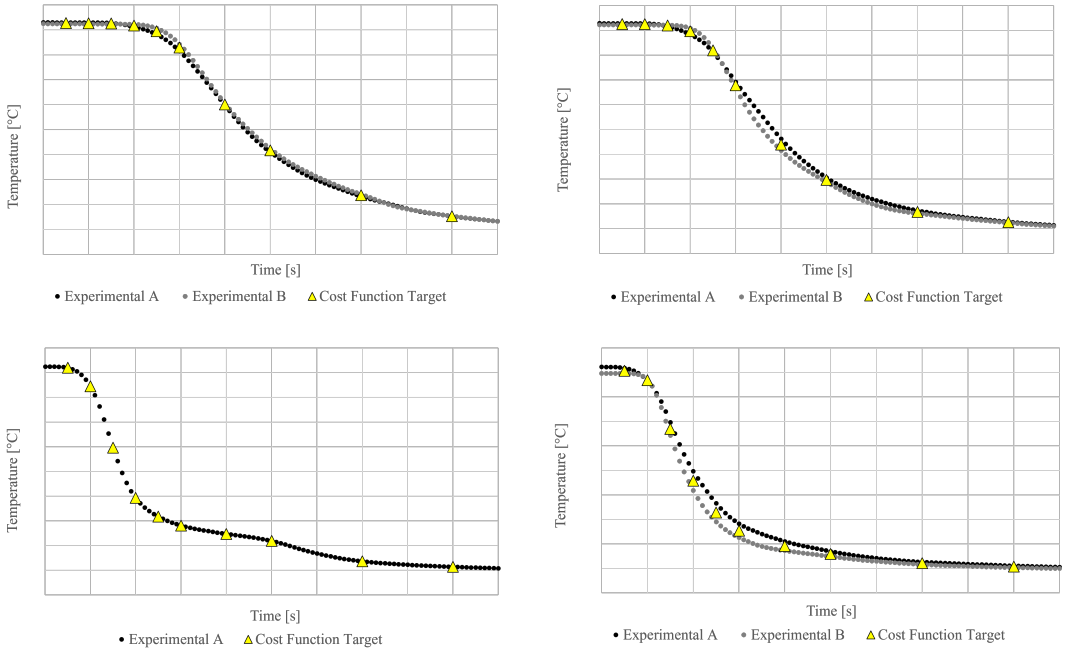

Figure 4.6 – Experimental temperatures T_{exp} used as target on the cost function.

$$f(h_1, h_2, ..., h_9) = \sum_{L=1}^{4} \sum_{t=1}^{10} \left((T_{calc})_{Lt} - (T_{exp})_{Lt}\right)^2 \tag{4.1}$$

The convective heat transfer coefficients which defines the peak of the cooling curves - h_3, h_5 and h_8 were bounded with inferior h_{min} and superior h_{max} limits, as shown on Equations 4.3 and 4.2, respectively. The boiling curve was used as reference for the definition of the boundary values. The top boundary h_{max} is 100 times higher than the low boundary h_{min}, resulting in a wide range that remains within the order of magnitude of the typical heat transfer coefficient for cooling problems [Faghri and Zhang, 2006]. This saves solver time by avoiding that the optimization algorithm evaluates unrealistic convective heat transfer coefficients, such as negative coefficients.

$$-h_k + h_{min} \leq 0 \; \forall \; k = 2, 5, 8 \tag{4.2}$$

$$h_k - h_{max} \leq 0 \; \forall \; k = 2, 5, 8 \tag{4.3}$$

The other variables were defined as a factor α of the peak value of each curve to ensure that the curve has a trapezoidal shape with the peak at the intermediate temperatures. The coefficient relationships are given in the Equations 4.4 to 4.6.

$$h_i = \alpha_i * h_2 \; \forall \; i = 1, 3 \tag{4.4}$$

$$h_j = \alpha_j * h_5 \; \forall \; j = 4, 6 \tag{4.5}$$

$$h_k = \alpha_k * h_8 \; \forall \; k = 7, 9 \tag{4.6}$$

In which,

$$0 < \alpha_l \leq 1 \; ; \; l = 1, 3, 4, 6, 7, 9 \tag{4.7}$$

Thus, the optimization algorithm optimizes the α_i values, rather than the h_i values, for $i = 1, 3, 4, 6, 7, 9$ due to the relationship of optimized parameters.

The output of the optimization algorithm is the set of variables $\{h_1, h_2, ..., h_9\}$ which results in the lowest temperature deviation from the experimental data on the evaluated locations while respecting the proposed constraints. This set was used to define the three temperature-dependent convective heat transfer coefficient curves utilized as boundary condition on the thermal model to represent heat flux on the cylinder surfaces during the quenching process, represented in Figure 4.5.

4.3 Residual Stress

An uncoupled thermal-thermomechanical finite element model was used to evaluate the residual stress created during the T6 thermal treatment. The temperature history was calculated in the thermal model and subsequently imported in the thermomechanical model, in which the plastic and creep strain accumulation resulting from the thermal load was calculated. Finally, the machining was simulated using the bulk removal method to obtain the residual stress distribution in the cylinder's final geometry.

4.3.1 Thermal FE Model

A transient thermal finite element model was used to calculate the temperature history during the quenching and artificial aging processes, schematically represented in Figure 4.7. Ansys Mechanical code was used for the simulation pre-processing, solving

and post-processing.

The cylinder geometry was meshed using the Ansys Mechanical integrated mesh algorithm using Ansys APDL SOLID186 (20-node hexahedron) and SOLID187 (10-node tetrahedron) elements, suited for the meshing of complex geometries. Both elements are second-order and tri-dimensional. The resulting mesh for the thermal analysis has 193.649 elements.

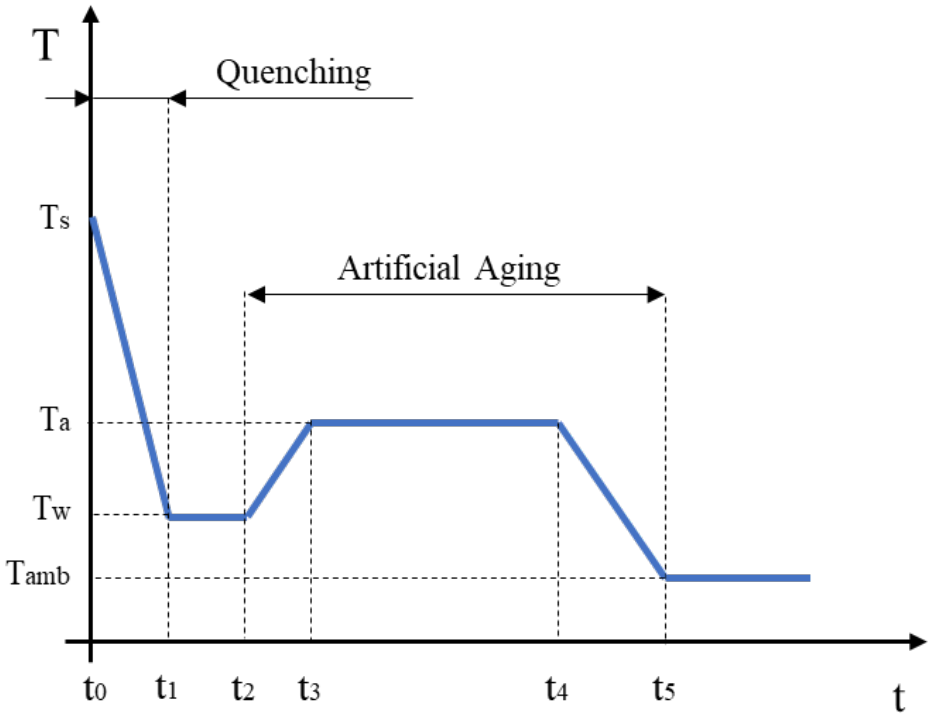

Figure 4.7 – Schematic calculated temperature history.

A mesh convergence study was performed using three mesh sizes (1, 2 and 3 times the characteristic length arbitrarily defined). The evaluated mesh sizes had a very low impact on the calculated temperature profile. The highest difference among the cooling curves was approximately 0.5% on the measured points. Figure 4.8 shows the cooling curves on region 1 for the three mesh sizes compared to the experimental data. The 3x characteristic length size was chosen as it does not have a significant impact on the temperature prediction, and further mesh size increase resulted in a poor representation of the geometry as the mesh size approaches the size of the geometry thickness in some regions.

Figure 4.7 shows the schematic representation of the calculated thermal treatment

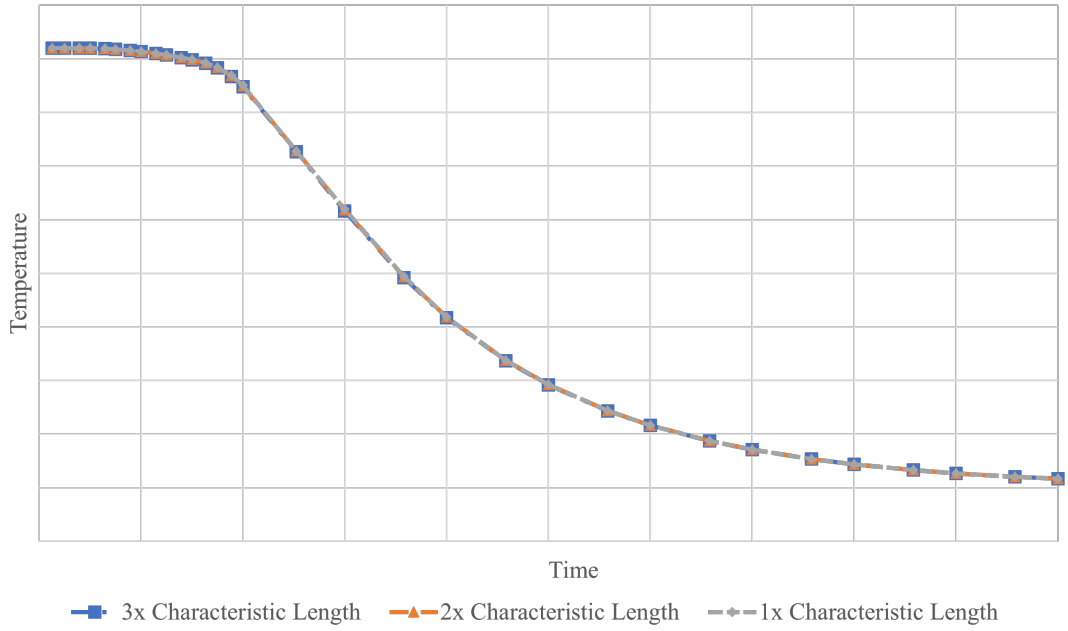

Figure 4.8 – Mesh convergence analysis for different mesh sizes.

processes. The thermal model starts at the end of the solution process at the instant t_0, where the cylinder is at homogeneous temperature T_s. A convective heat transfer model is applied on the cylinder surfaces to model the heat exchange with water during the quenching process. The utilized convective heat transfer coefficients were determined by solving the inverse problem, presented in section 4.2, which resulted in three temperature dependent convective heat transfer coefficient curves, assigned to their correspondent surfaces. The ambient temperature T_∞ in the convection model was considered to be constant and equal to the water temperature T_w. Quenching ends at instant t_1 when the parts reach homogeneous water temperature T_w.

Additionally, the convective heat transfers were gradually activated in different regions of the cylinder to represent the water entrance effect, which accentuates the asymmetry in the resulting thermal profile and contributes for residual stress formation. Figure 4.9 schematically represents three instants t_A, t_B and t_C during the water entrance and the respective surfaces in which the heat transfer was activated. The waiting time for the activation of the heat transfer in each region was determined by manual fitting of the experimental measurements. The number of the divisions was defined according to the need for a good fit with the experimental data.

The artificial aging process starts at the instant t_2, which is virtually the same as

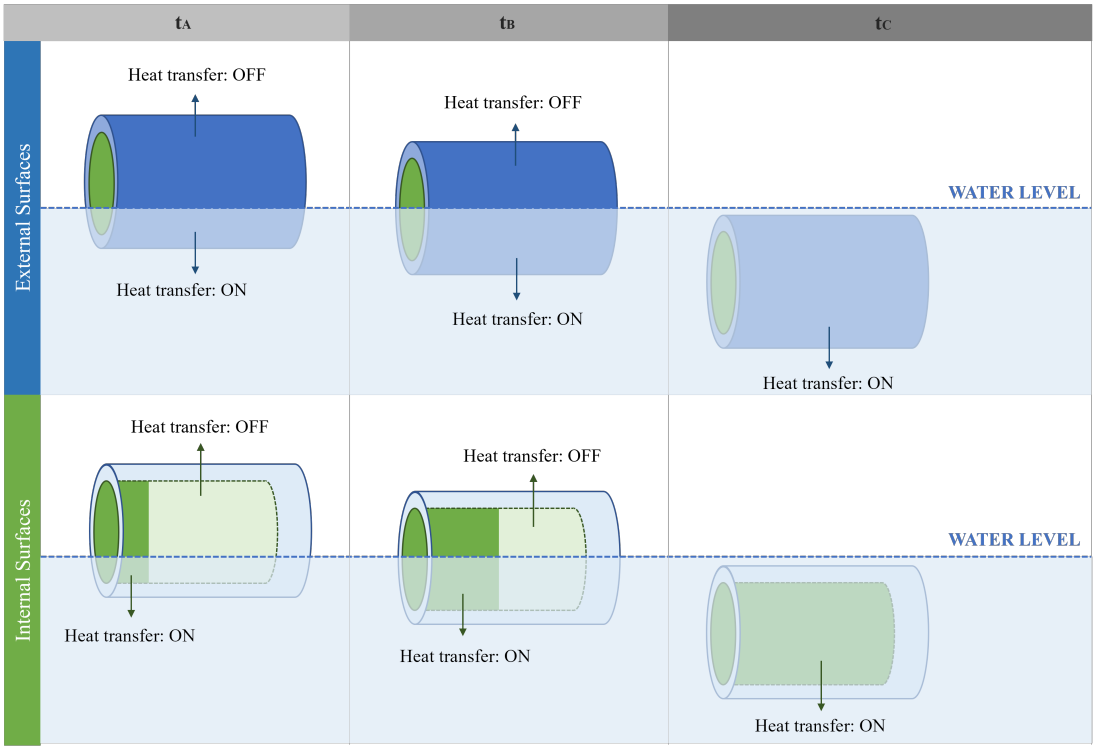

Figure 4.9 – Schematic representation of water entrance effect on heat transfer.

the instant t_1 in the calculation. As this process occurs at a low heat transfer rate, a constant convective heat transfer could be used to model the temperature ramp-up to the artificial aging temperature T_a, used as the ambient temperature T_∞ in the convective model. The parts reach such temperatures at the instant t_3 and are kept at constant temperature until the instant t_4, where the ambient temperature T_∞ was set at room temperature to model the temperature ramp-down to ambient temperature. The artificial aging ends at the instant t_5, where the parts are at constant room temperature T_{amb}.

4.3.2 Thermomechanical FE Model

Once the temperature history was evaluated for all the relevant thermal treatment processes, it was imported into a mechanical finite element model to evaluate the resulting residual stresses. The thermal and thermomechanical models are uncoupled; thus, the thermomechanical model was solved subsequently to the thermal model solution.

The mesh for the mechanical model was also created using the meshing algorithm integrated with Ansys Mechanical and using the APDL elements SOLID186 and SOLID187. However, the strain calculation required a finer mesh to reach the spatial

discretization convergence, resulting in a mesh with 603.229 elements.

Figure 4.10 schematically represents the residual stress creation and modification of a virtual critical point for each of the thermal treatment processes imported into the thermomechanical model.

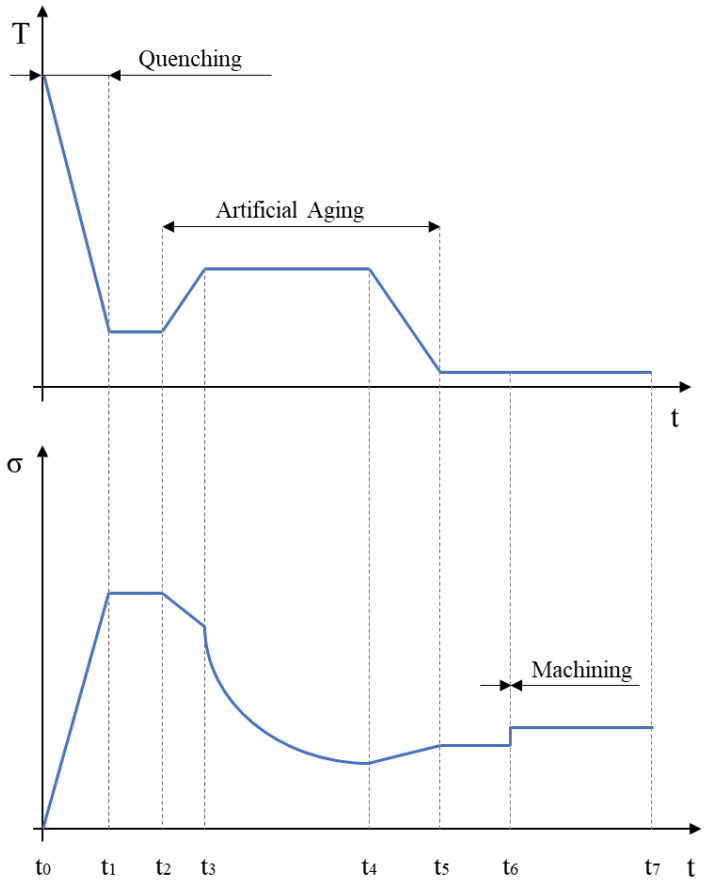

Figure 4.10 – Relationship between temperature and stress histories.

Quenching begins at the instant t_0 in which the parts are stress-free due to the prior stress relief promoted by the solution process. During the quenching, residual stress is created within the parts due to inhomogeneous plastic strain formation resulting from the severe thermal gradients. A temperature-dependent multilinear isotropic hardening model (MISO) was used to model the material plastic flow at elevated temperatures.

The plastic strain accumulation is a non-linear phenomenon; thus, an appropriate time-step calculation is required for an accurate numerical model response. The plastic strain accumulation convergence was studied for different time-step sizes, in order to ensure that the temporal discretization would not have a significant impact in the model plastic strain prediction. The total plastic strain accumulation value for 0.1, 0.25 and

0.5 second time-steps and the correspondent solver time are shown in the Figure 4.11 using the base case of 0.25 s as 100%. A 0.25 s time-step size was chosen as the further refinement to 0.1 s led to an difference of only 1.1% in the plastic strain accumulation and an increase of 99% in the solver time.

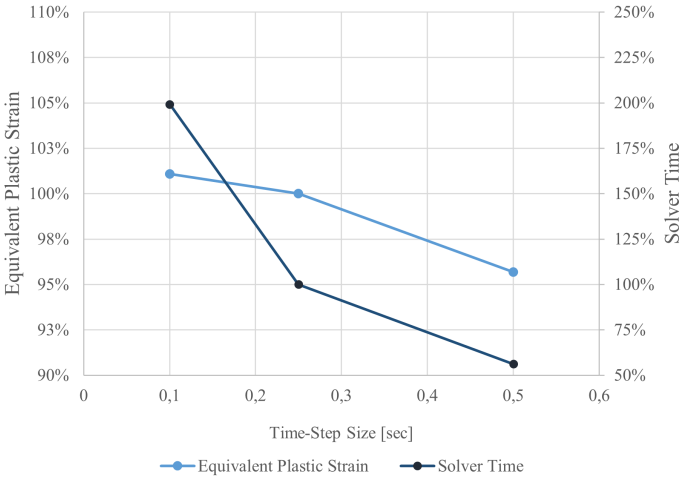

Figure 4.11 – Plastic strain convergence and solver time for different time-step sizes.

From the instant t_2 and t_3 the part experiences a stress relaxation due to the elastic modulus softening resulting from the increasing temperature and the opposite behavior can be seen between instants t_4 and t_5. These phenomena are modeled through the temperature dependent elastic modulus defined in the isotropic linear material model.

At instant t_3 the parts reach the artificial aging temperature T_a and are kept at this temperature for a long period of time. Between the instants t_3 and t_4 a time-stress dependent creep rate law was activated to model the residual stress relaxation due to the elastic strain conversion to creep strain. At instant t_4 onward, the creep law is deactivated.

An experimental test at treatment temperature was conducted on the material, and the creep model, given in Equation 3.38, had its constants C_1 to C_3 determined by a curve fitting method using the experimental stress relaxation curves as reference. As this event occurs at a constant temperature, the temperature dependency was neglected by setting the constant C_4 to zero. The curves were measured at the aging temperature T_a on two different initial stress levels σ_A and σ_B. The numerical model response and the experimental data for stress relaxation are shown in Figure 4.12.

The inherent time-dependency of the creep model requires an appropriate calculation time-step for an accurate stress relaxation prediction. A uniaxial model was used

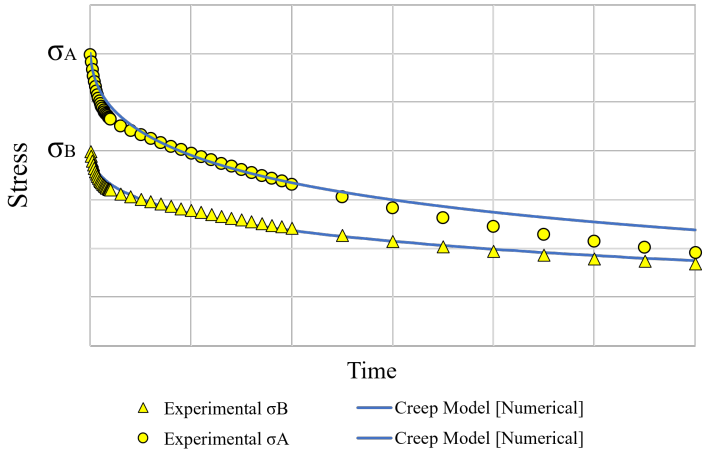

Figure 4.12 – Creep model curve fitting on experimental stress relaxation test.

to evaluate the stress convergence using different time-step sizes. The stress relaxation rate is higher at the initial phase of the relaxation curve; thus, it was chosen to define the time-step sizes according to the stress percent change to obtain a finer time-step in the regions with a higher stress relaxation rate. The convergence graph is given in Figure 4.13. The calculated step-size was set to match every 2 % stress variation as it yielded a deviation of 10 % to the experimental data.

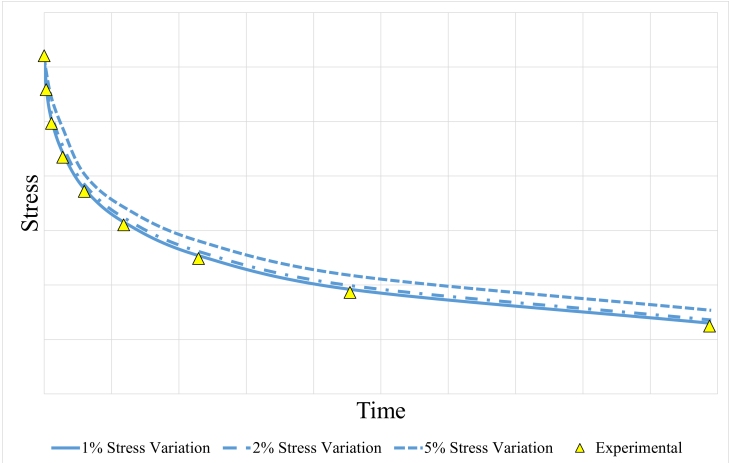

Figure 4.13 – Numerical stress relaxation response to different time-step sizes and comparison to experimental stress relaxation data.

At the instant t_6 the machining is modeled by killing the mesh elements in the removed geometry using the birth-and-death feature available in Ansys Mechanical. This feature lowers the stiffness of the defined elements to a near zero value; thus, their con-

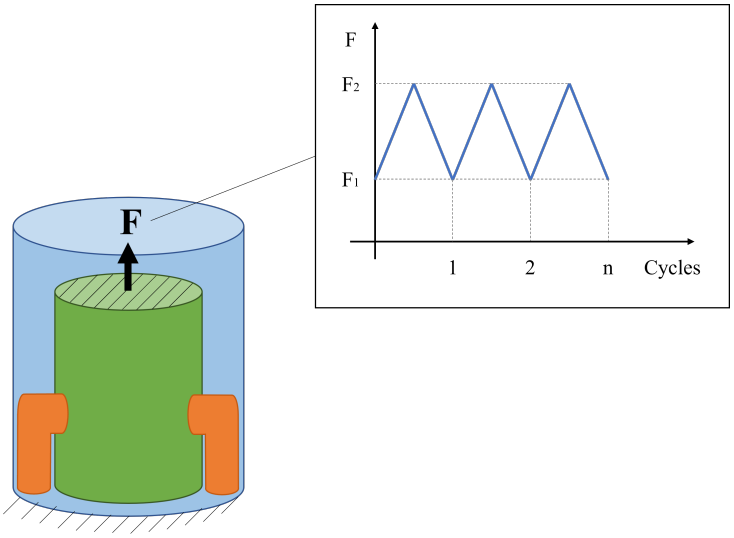

Figure 4.14 – Bench test load history.

tribution for the part stiffness becomes negligible. This modifies the part stiffness and rearranges the residual stress to achieve the new equilibrium state. All other machining loads were neglected.

Finally, at the instant t_7 the cylinder has its final geometry and residual stress resulting from the manufacturing processes. The stress tensors for all mesh nodes are exported at this instant to be included in the subsequent fatigue calculation.

4.4 Bench Test

A bench test is used to evaluate the fatigue strength of cylinders, in which the cylinder must sustain n pulsating load application cycles without presenting fatigue failures. The resulting stress distribution during the bench test run is obtained through a finite element model simulation, in which the bench test equivalent forces F_1 and F_2 are applied in the cylinder head. A schematic representation of the bench test is given in the Figure 4.14. The resulting stress tensors for these two scenarios are then exported to be evaluated in the subsequent fatigue calculation.

4.4.1 Fatigue Calculation

The stress tensors obtained from the bench test simulation are combined to form the stress amplitude σ_a and mean stress σ_m tensors. These tensors are used in Gerber's model for the endurance safety factor calculation.

To evaluate the influence of the residual stress in the safety factors, the calculated residual stress tensor σ_{RS} was summed with the mean stress tensor and the endurance safety factors were reevaluated with the modified mean stress $\sigma_{m_{RS}}$ and all other parameters unaltered.

$$\sigma_{m_{RS}} = \sigma_m + \sigma_{RS} \tag{4.8}$$

4.4.2 Endurance Safety Factor Validation

The resulting endurance safety factors with and without the residual stress consideration were finally compared to the experimental bench test results. A consolidation table was made with the fatigue failures occurrences per region and the corresponding endurance safety factors with and without residual stress consideration. The results were compared to check if the regions which presented the most fatigue failure occurrences matched the regions with the lowest safety factors and if the consideration of residual stress increases the endurance safety factors accuracy.

5 RESULTS

The calculation results and their analysis are presented in this chapter. The results are presented in three groups:

- Thermal treatment temperature history calculation.
- Influence of residual stress on the cylinder durability on bench test.

5.1 Thermal treatment temperature history calculation

The temperature history for quenching and artificial ageing were calculated using a transient thermal analysis using the finite element method. The boundary conditions were found by solving the inverse heat transfer problem. The temperature history is used subsequently as a thermal load in the mechanical model used for the residual stress calculation.

5.1.1 Inverse heat transfer problem

The heat flux on the cylinder surfaces during quenching was obtained by solving the inverse heat transfer problem. The cost function which evaluates the deviation between the model prediction and the experimental data was minimized using an adaptive single-objective solver. A total of 421 scenarios were evaluated with different values for the 9 heat transfer coefficients h_1 to h_9, schematically defined on Figure 4.4.

Figure 5.1 shows the 11 lowest cost function values, which will be called as best candidates. Candidate point 1 showed the lowest cost function value among the 421 tested candidates. However, the other best candidates presented similar cost function values and further analysis should be done to define which one of them is the most appropriate solution for the proposed quenching modeling.

Figures 5.2 to 5.5 show the resulting cooling curves from the best candidates. The experimental data used to build the cost function are also given for comparison. The closer the model prediction to the experimental data, the better.

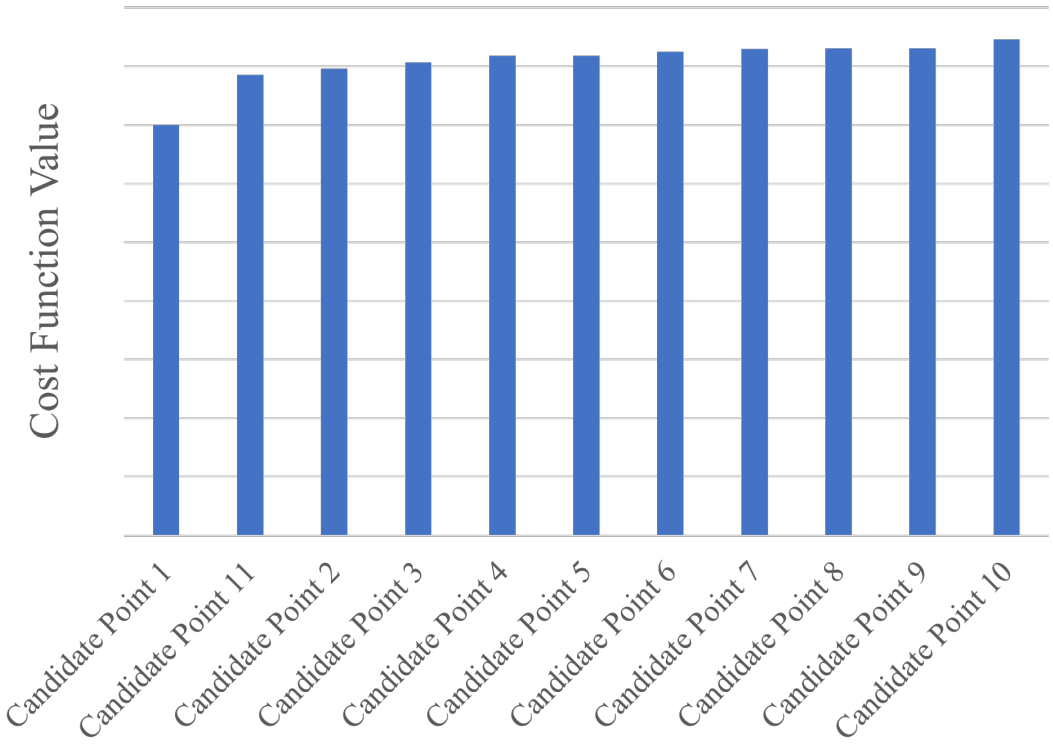

Figure 5.1 – Cost function values for the top 11 best candidates.

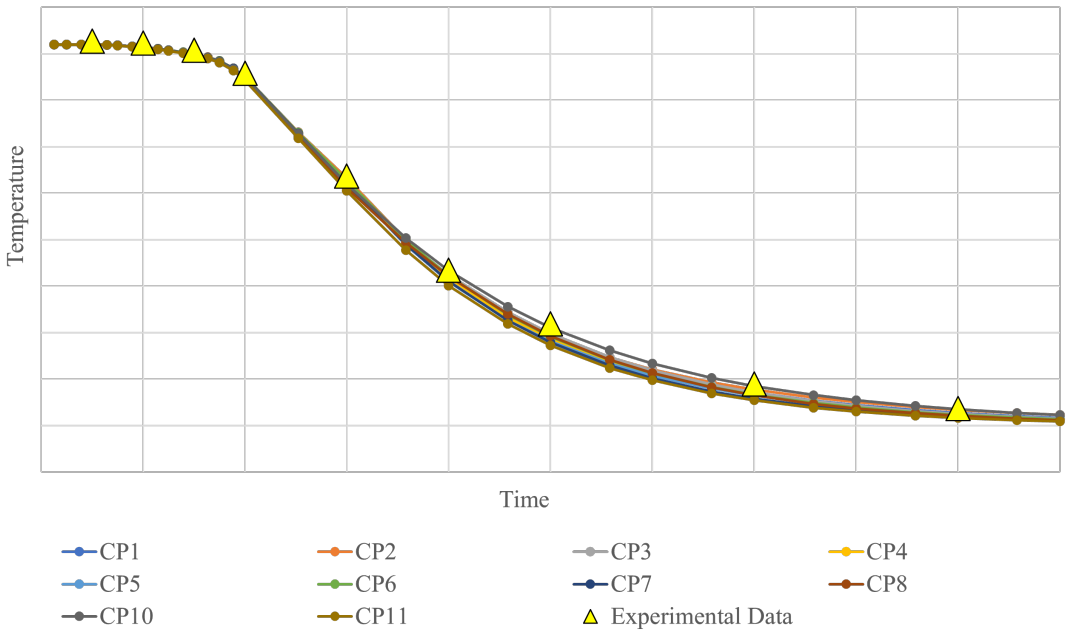

Figure 5.2 – Temperature history on region 1 for the top 11 best candidates from the optimization in comparison to the optimization targets.

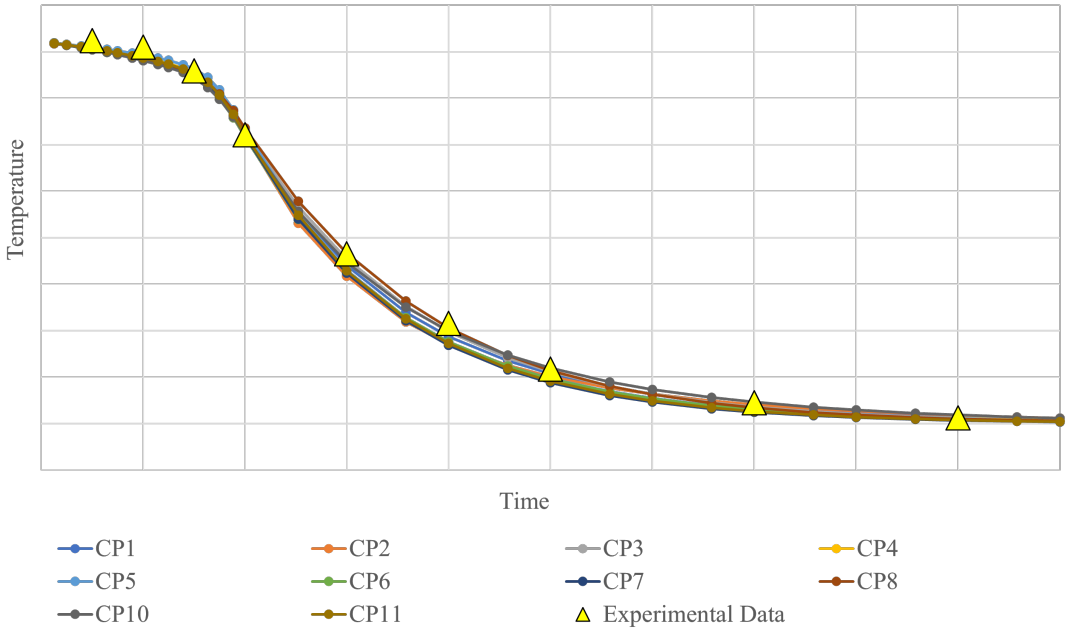

Figure 5.3 – Temperature history on region 2 for the top 11 best candidates from the optimization in comparison to the optimization targets.

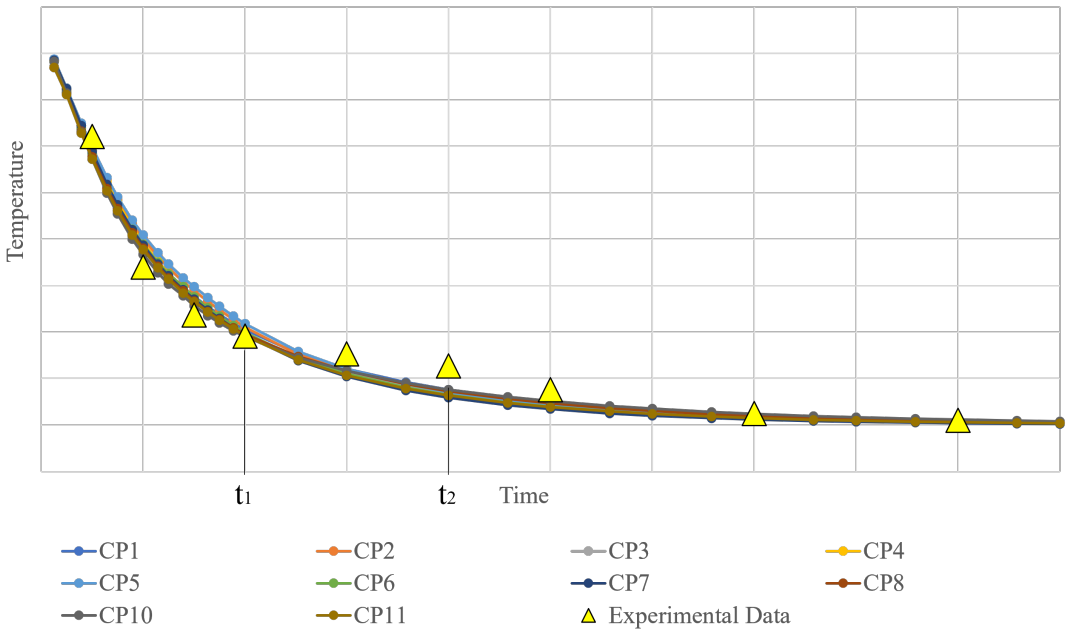

Figure 5.4 – Temperature history on region 3 for the top 11 best candidates from the optimization in comparison to the optimization targets.

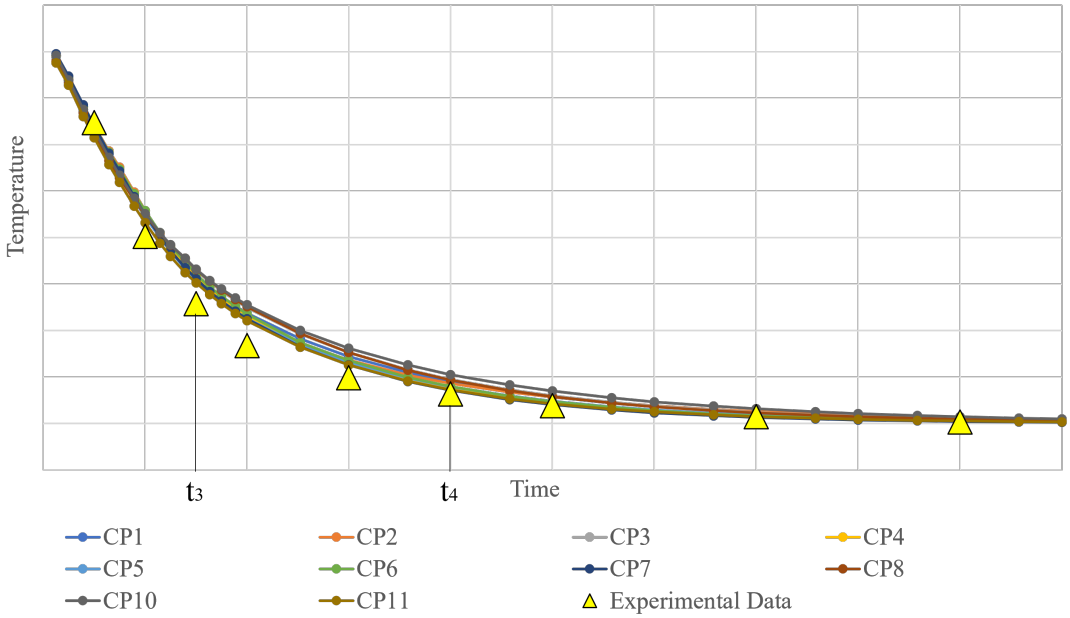

Figure 5.5 – Temperature history on region 4 for the top 11 best candidates from the optimization in comparison to the optimization targets.

The results obtained by the optimization algorithm for the best candidates are similar to each other and in accordance with the experimental data. Small deviations can be seen for all candidates in regions 3 and 4, in Figures 5.4 and 5.5, respectively.

The experimental measurement in region 3 shows an atypical change in the heat transfer rate on the indicated interval defined by the instants t_1 and t_2. This rate change is believed to be caused by trapped water vapor, which creates an insulation layer between the part and liquid water. As the fluid dynamics and phase change are not modeled, the solver could not reproduce such behavior, resulting in a temperature curve that approximates the measured data average behavior.

Region 4 shows a deviation in the interval defined by the instants t_3 and t_4. It is believed that the heat transfer coefficients could not fit the temperature in this region due to the linear definition of the temperature-dependent heat transfer coefficient curve. It could be beneficial if the solver could modify the coefficients in a non-linear manner, especially in lower temperatures.

Figure 5.6 shows the temperature-dependent convective heat transfer coefficient curves for the best candidates found by the optimization algorithm. All curves have the proposed trapezoidal shape, indicating that the constraints could control the parameters

and keep the curves according to the proposed modeling. The coefficients which define the curve at upper and lower temperatures (h_1, h_3, h_4, h_6, h_7 and h_9) showed a high dispersion among the best candidates. While the coefficients which define the curve peak (h_2, h_5 and h_8) showed a smaller dispersion.

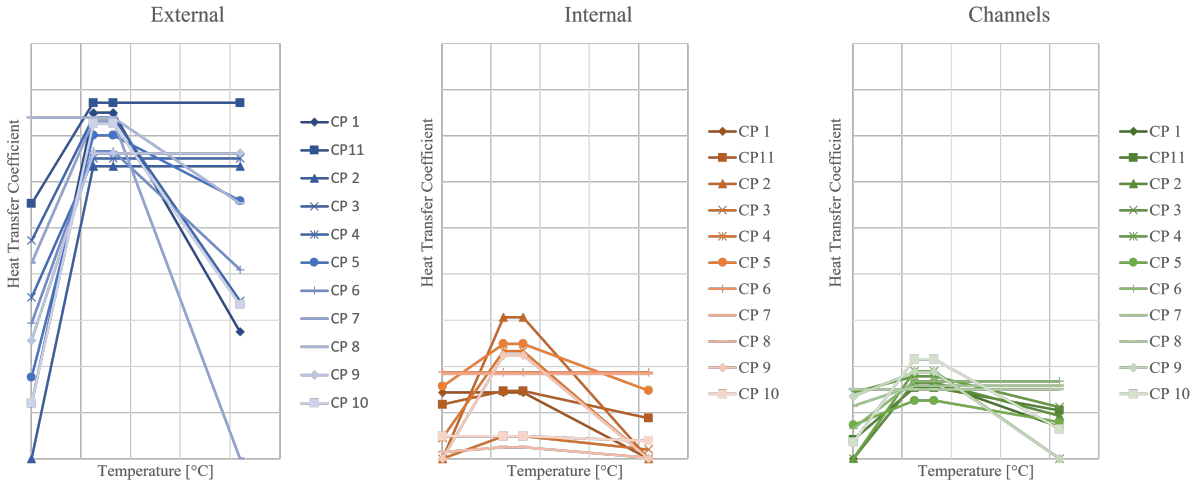

Figure 5.6 – Heat transfer coefficient curves for the top 11 best candidates.

Candidate Point 1 was used as reference to run a parameter sensitivity analysis, to further investigate the dispersion seen in the heat transfer coefficient curves, shown in Figure 5.6. The impact of a variation on each variable on the cost function value is evaluated in this analysis. Figure 5.7 shows the variation of the cost function for a unit change on each variable. The cooling curves resulting from the sensitivity analysis are found in the Appendix A.

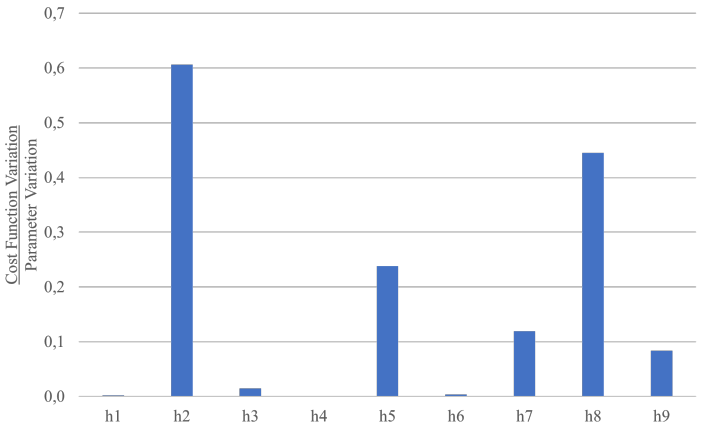

Figure 5.7 – Cost function variation for a unitary change on each variable.

The parameters which showed a higher dispersion on Figure 5.6 (h_1, h_3, h_4, h_6, h_7 and h_9) have only a marginal impact on the cost function value, as can be seen in Figure 5.7. While the parameters which showed a lower dispersion (h_2, h_5 and h_8) have a greater impact on the cost function. This explains the high dispersion seen in the least sensitive parameters and also indicates the optimization algorithm's capability to refine the solution on the most important parameters to minimize the cost function.

The cost function showed a high sensitivity for the variation of the parameters which define the peak values of the heat transfer coefficient curves (h_2, h_5 and h_8). This behavior was expected as these parameters have a high influence in the curve, due to the variable definition presented in equations 4.4 to 4.6. These parameters define not only the peak of the coefficient curve, but also modify the curve at both lower and higher temperatures.

The parameter h_2 defines the peak of the curve for the external region, which has the largest surface area (among the three defined regions) and is in contact with fresh water; thus, it is expected that most of the heat would be transferred through the external cylinder boundaries. This explains why parameter h_2 is the most sensitive to variations in the cost function. A lower heat transfer is expected in the internal and channel regions as the water flow is constrained by the part itself, limiting the supply of fresh water and retaining water vapor.

The optimization results can also be analyzed for each variable independently, despite the cost function value being dependent of the combination of all parameters. Figures 5.8, 5.9 and 5.10 show the cost function value resulting from the 421 cases evaluated during the optimization. The top three candidates (CP1, CP11 and CP2) are highlighted for better visualization.

Figure 5.8 shows the cost function values resulting for the parameters (h_1, h_2 and h_3) which define the external convective heat transfer coefficient curve. Parameters h_1 and h_3 have a wide range which results in similar low cost function values and the top three candidate points are spread along this range. This further reinforces that the cost function has a low sensitivity to the variation of these parameters. Parameter h_2 shows a narrow range of values which results in low cost function values and the top three candidates are concentrated in this narrow range, indicating that the cooling curves at the evaluated locations are highly sensitive to the variation of this parameter, in accordance with the

sensitivity study.

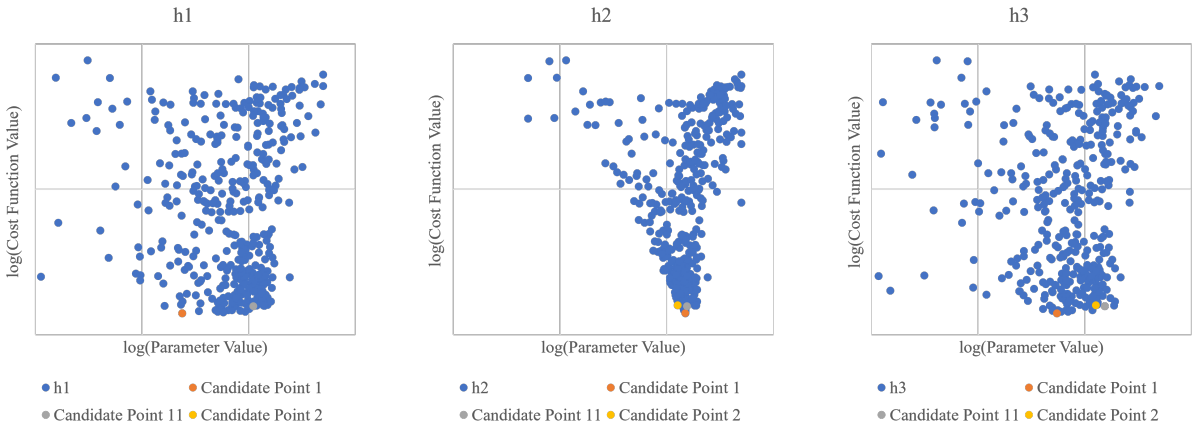

Figure 5.8 – Cost function values for every h_1, h_2 and h_3 variable values evaluated during the optimization process and the top 3 candidates for best solution.

Figure 5.9 shows the cost function values in function of the parameters (h_4, h_5 and h_6) which define the internal convective heat transfer coefficient curve. Parameters h_4 and h_6 show a wide range which results in similarly low cost function values, which indicates a low impact on the cost function and is in line with the sensitivity study. The lowest cost function values are seen in a wider region on parameter h_5 than seen in parameter h_2, which indicates a lower sensitivity and is in line with the sensitivity study results. Candidate Points 1 and 2 for the parameter h_6 are zero, thus; cannot be represented in the logarithmic scale.

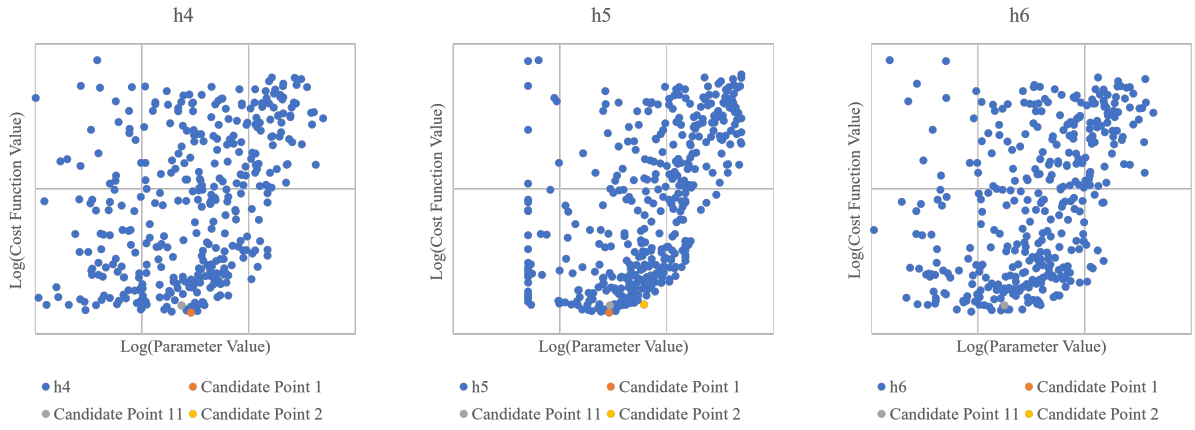

Figure 5.9 – Cost function values for every h_4, h_5 and h_6 variable values evaluated during the optimization process and the top 3 candidates for best solution.

Figure 5.10 shows the cost function values for each of the parameters (h_7, h_8 and h_9) which define the convective heat transfer coefficient curve on the channels. Parameter h_8, which defines the curve peak, shows a narrow range of values which results in lower cost function values. The range is not as narrow as seen in h_2 and not as wide as seen in h_5, thus; an intermediate sensitivity is expected and proved by the sensitivity analysis. Candidate Points 1 and 2 for the parameter h_7 are zero; thus, cannot be represented in the logarithmic scale.

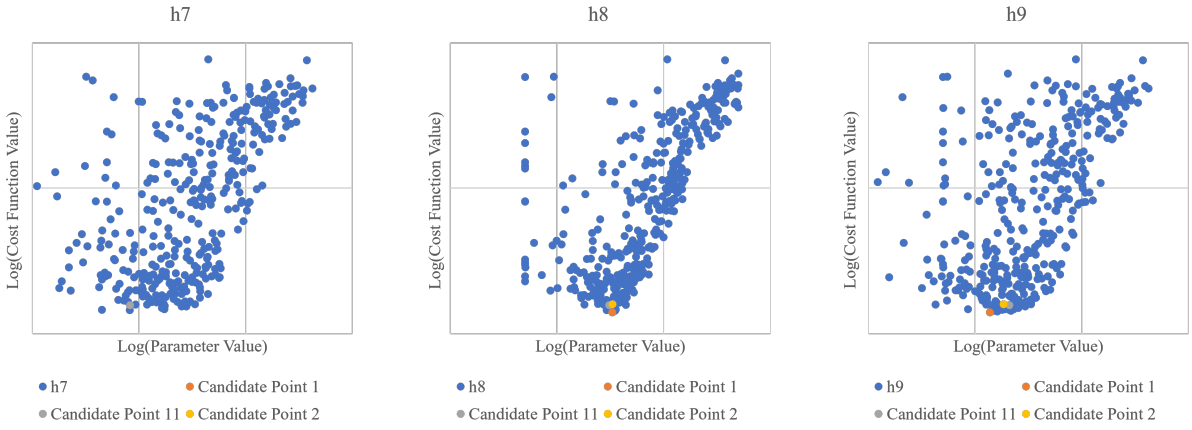

Figure 5.10 – Cost function values for every h_7, h_8 and h_9 variable values evaluated during the optimization process and the top 3 candidates for best solution.

The optimum values for the variables h_2, h_5 and h_8 are defined within the proposed range, which shows that the solver is not constrained by the chosen range. Other variables show their optimum values near the lower boundary of the defined range (particularly h_6 and h_7), which were set as zero. However, the range could not be further increased as it would result in negative convective heat transfer coefficients, which violates the modeled physics.

Despite the relative dispersion, all best candidates showed similar cooling curves due to the lower sensitivity of the parameters which presented the highest dispersion. Thus, any of the best candidates would represent the cooling curves with reasonable accuracy on the four analyzed regions. However, nothing can be said about the result quality for the regions which were not experimentally measured.

The deviation on the cooling curves resulting for the best candidates were evaluated in the regions where the experimental data is not existent by measuring the temperature on every mesh node in three time instants (t_A, t_B and t_C in Figure 5.11) for all best

candidates. The node which presented the highest temperature variation among the best candidates was selected and its cooling curve is plotted on Figure 5.11 for all best candidates. Nodes in edges and corners were excluded on this analysis as they have a high surface to volume ratio, which results in steep temperature gradients.

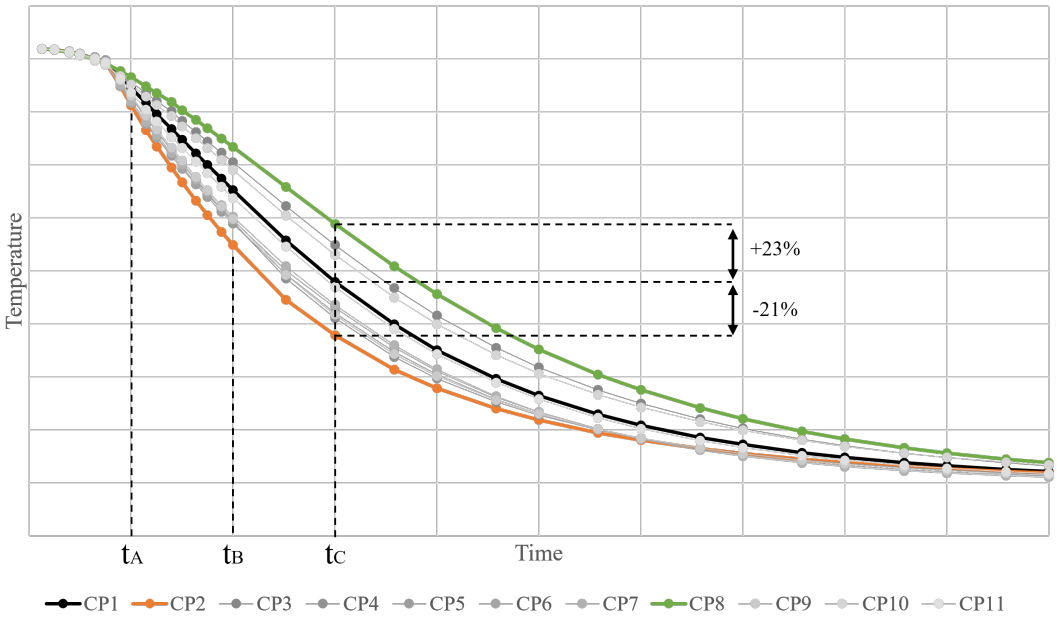

Figure 5.11 – Comparison of the cooling curves for the top 11 best candidates in the region which showed the highest deviation.

The highest and lowest cooling rates are seen in the candidate points 2 and 8, highlighted in Figure 5.11. The highest deviation is seen in instant t_C, where CP8 showed an instant temperature 23% higher than CP1, while CP2 showed an instant temperature 21% lower. The solver could not penalize the solution which deviates from the real temperatures as there is no experimental data for this region. Thus, the solution could be further refined if more experimental data was available, especially in the region analyzed in Figure 5.11, which showed the highest temperature dispersion among the best candidates.

All candidate points among the best candidates showed feasible heat transfer coefficient curves, in accordance with the proposed modeling. The resulting cooling curves are similar to each other and in accordance with the available experimental data, despite showing a higher dispersion on other region where the experimental data is unknown. Candidate point 1 was chosen to represent the quenching boundary conditions as it resulted in the lowest cost function among the tested scenarios for the available experimental

data. Additionally, CP1 showed an average result among the best candidates in the region showed in Figure 5.11. As the experimental data is unknown in this region, the choice of the mean behavior minimizes the potential deviation from the model prediction to the real temperature.

The temperature dependent heat transfer coefficient curves defined from the candidate point 1 are given in detail on the Figure 5.12.

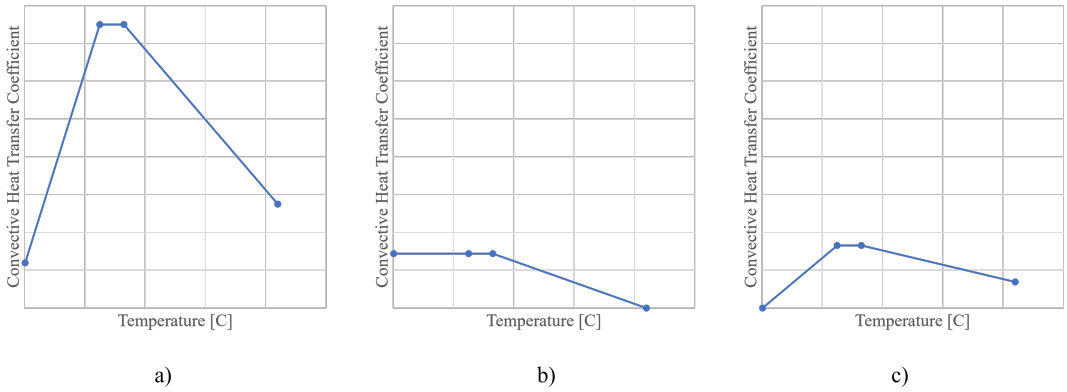

Figure 5.12 – Chosen temperature dependent convective heat transfer coefficient curves for the a) external b) internal and c) channel regions resulting from the optimization process.

The calculated cooling curves resulting from the chosen temperature dependent convective heat transfer coefficient curves are plotted alongside the experimental cooling curves in the Figures 5.13 to 5.16 for the four evaluated regions.

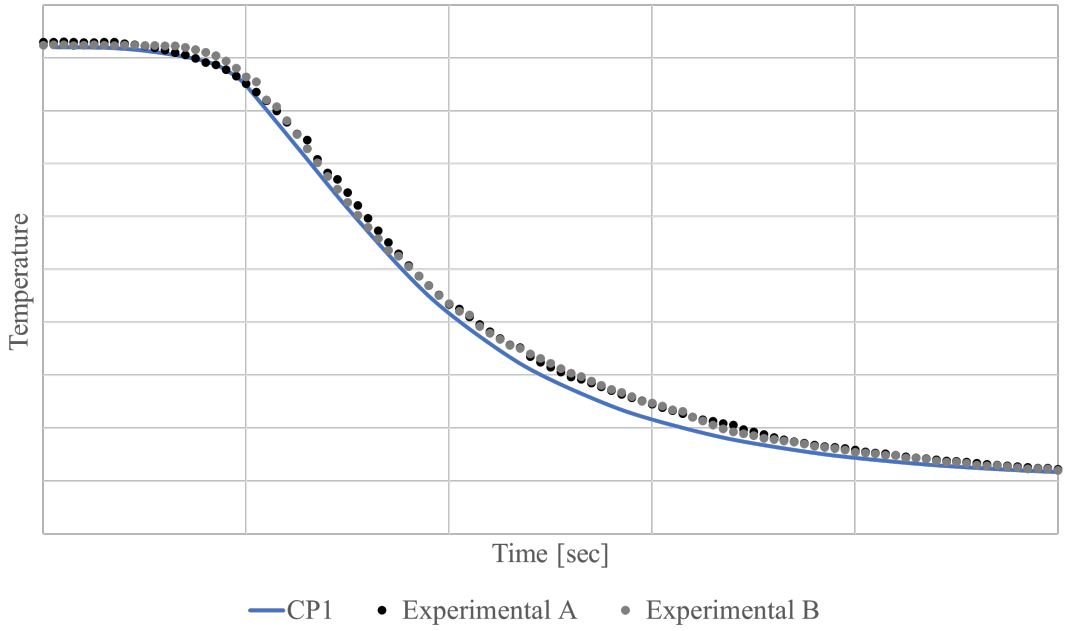

Figure 5.13 – Resulting temperature history for the chosen HTC curves in comparison to measured data on region 1.

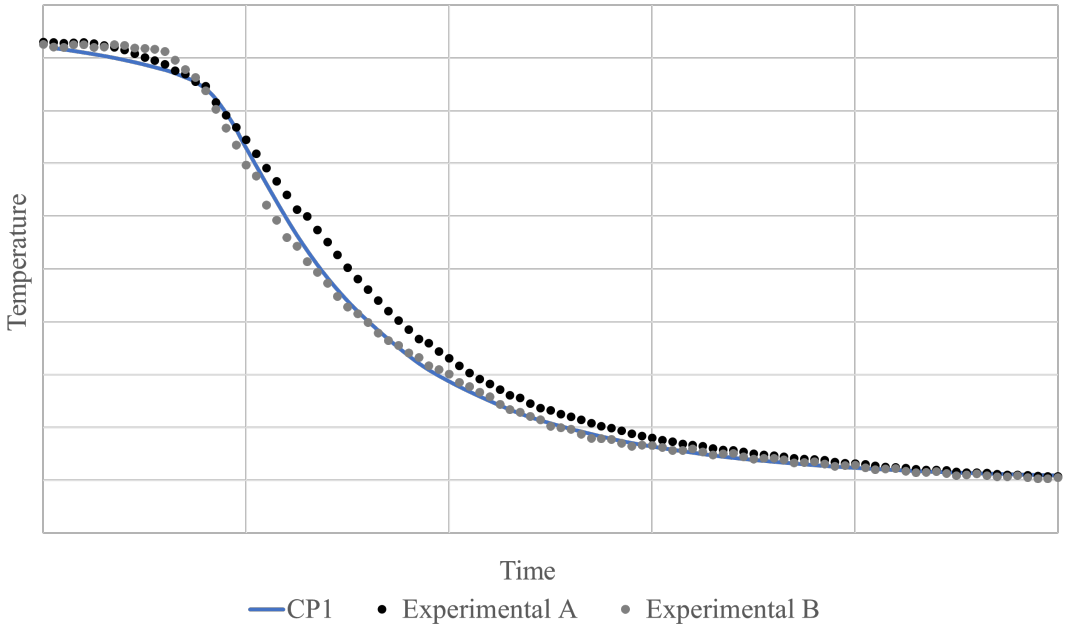

Figure 5.14 – Resulting temperature history for the chosen HTC curves in comparison to measured data on region 2.

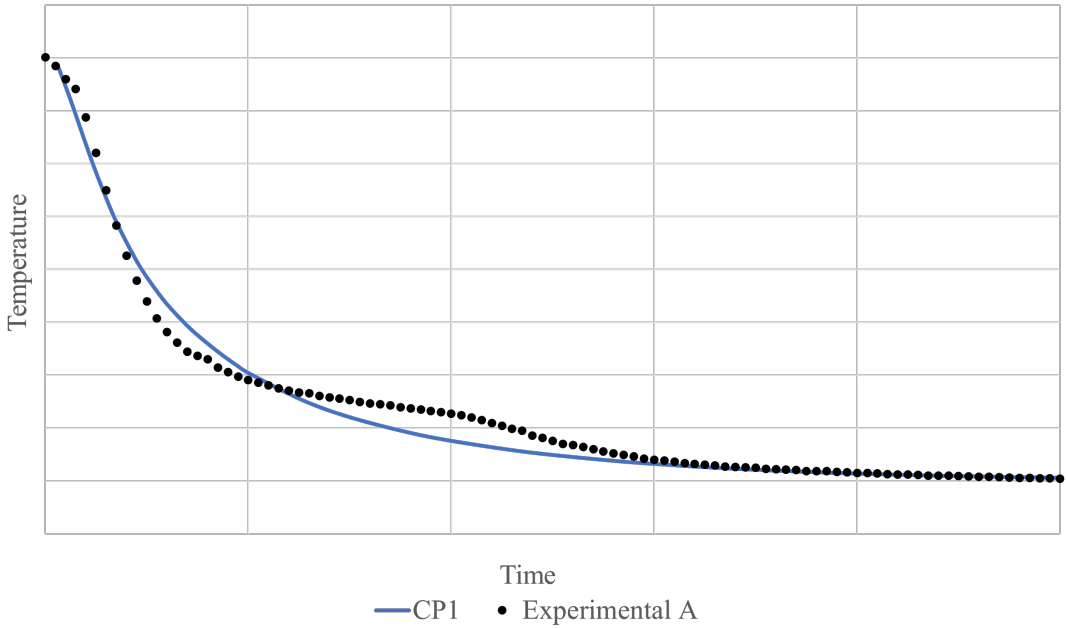

Figure 5.15 – Resulting temperature history for the chosen HTC curves in comparison to measured data on region 3.

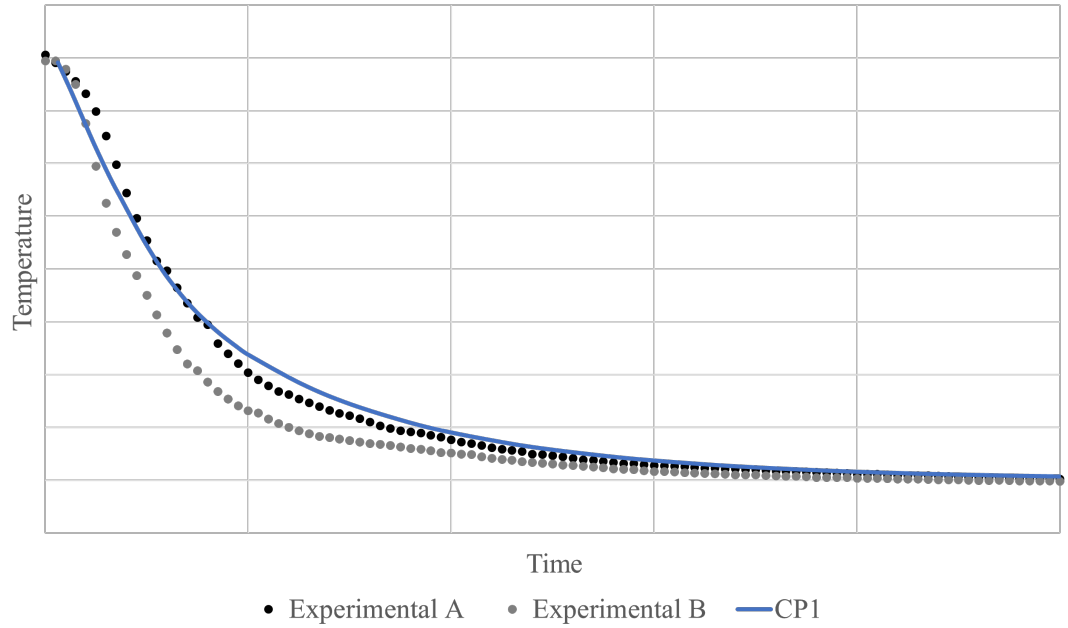

Figure 5.16 – Resulting temperature history for the chosen HTC curves in comparison to measured data on region 4.

5.1.2 Artificial ageing

A constant convective heat transfer coefficient was used to represent the temperature ramp-up and cooling-down during the artificial ageing process as both processes occur at still air. The heat flux in the surfaces are low and both temperature ramp-up and cooling-down occur almost at homogeneous temperatures within the cylinder. The temperature history is given in Figure 5.17 for the 4 analyzed regions, which are practically identical as the temperature gradients are low. The ordinate seen in Figure 5.17 is the same as used in all other temperature graphs, but the abscissa is modified as the artificial ageing process lasts hours and the quenching lasts only a few seconds.

The temperature plateau is the most important effect to be modeled on this process as the temperature increase partially relaxes the residual stress due to the elastic modulus softening and the process long duration at high temperatures causes stress relaxation due to viscous effect. The cylinder reaches the temperature plateau at homogeneous temperature and remains at a constant temperature for the specified period. Thus, all important features for the residual stress calculation are captured by the model.

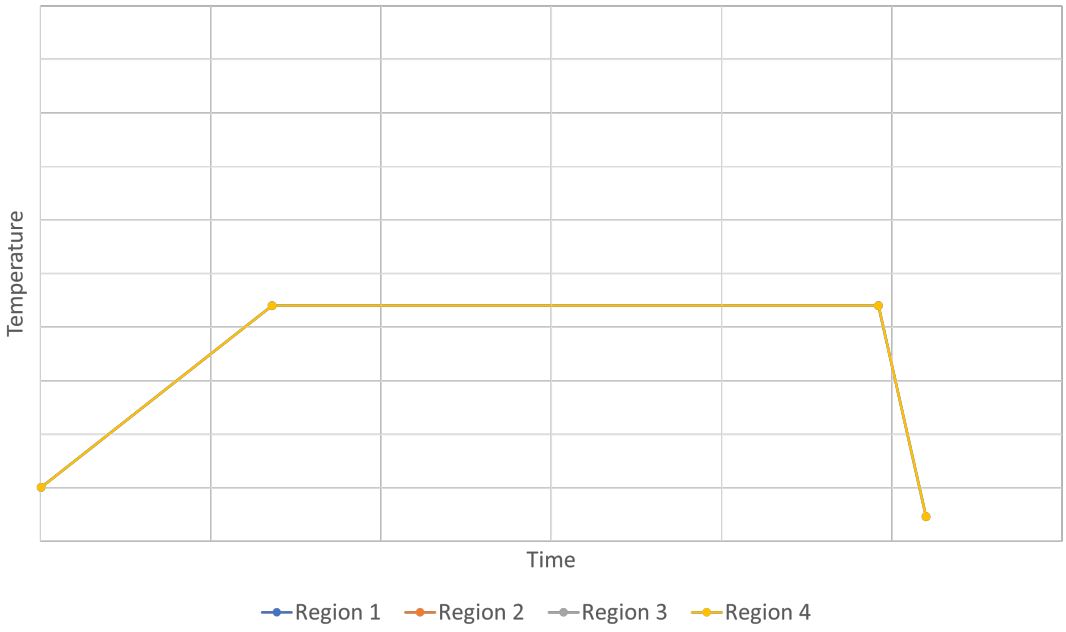

Figure 5.17 – Resulting temperature history during artificial ageing process.

5.2 Influence of residual stress on the cylinder durability on bench test

The residual stress (RS) impact on fatigue performance is evaluated by considering the residual stress as an additional constant stress in the load cycle. Two scenarios are compared to evaluate the effect of the residual stress in the fatigue failure prediction. The first scenario uses the stress mean and amplitude resulting only from the bench test cyclical load. The second scenario considers the same stress amplitude, but the mean stress is composed by the sum of the bench test and residual stress loads. These two scenarios, respectivelly, with and without residual stress, are then compared to the bench test experimental data in the regions A, B, C and D, schematically represented in Figure 5.18. These regions are known to be critical for fatigue failures and cracks were observed in the prototypes built during the initial phases of the cylinder project. The residual stress evolution during the manufacturing is then analyzed in the most critical node for each of the selected regions.

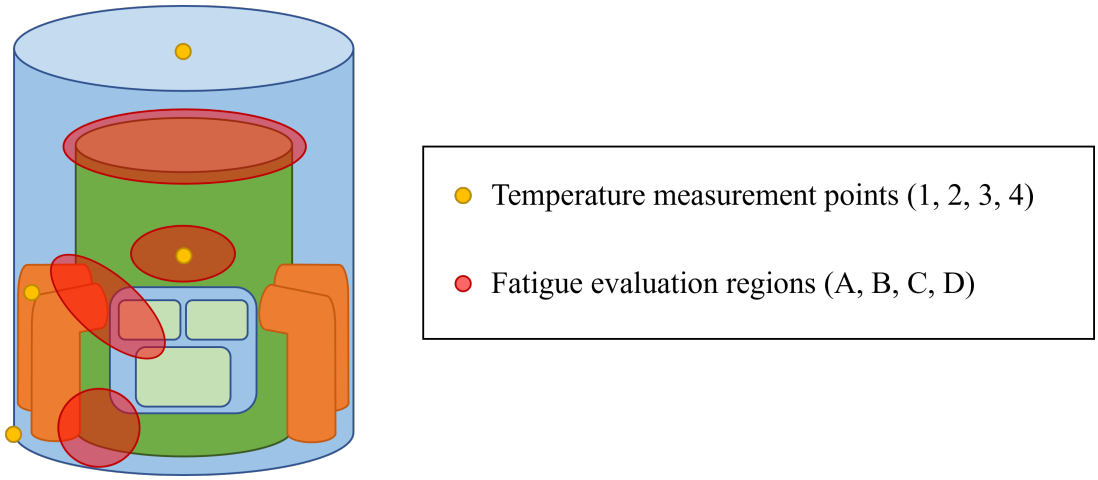

Figure 5.18 – Schematic representation of evaluated regions.

In order to preserve the data confidentiality, the stress and fatigue data will be presented in normalized values. The Haigh diagram, usually given with the stress amplitude σ_a in the ordinate and the mean stress σ_m in the abscissa, is given instead in terms of σ_a/σ_f and σ_m/σ_{UTS}, respectively. The relative comparison to the material limits remains unchanged; thus, there is no loss in the data analysis.

Figures 5.19 to 5.22 show the stress data resulting from the finite element analysis (FEA) of the FEA bench test with and without residual stress resulting from CP1. The

endurance safety factors (FS_e) are calculated to determine the most critical node to fatigue failure, which is then highlighted and presented in red color in the Figures 5.19 to 5.22.

Region A was the second most critical region for fatigue failures during the bench test. Figure 5.19 shows the alternate and mean stress data for region A. The stress data without residual stress is distributed in a linear manner, which is coherent to the constant load ratio R applied in the cylinder during the bench test. The stress data with the consideration of the residual stress is mostly shifted to higher values of mean stress (right-hand side in the figure). This shows a predominant tensile residual stress in this region, which is detrimental to fatigue performance. However, the most critical node for both scenarios (with and without RS - highlighted in red) are very close to each other, which indicates a low residual stress impact on the fatigue performance of this specific region.

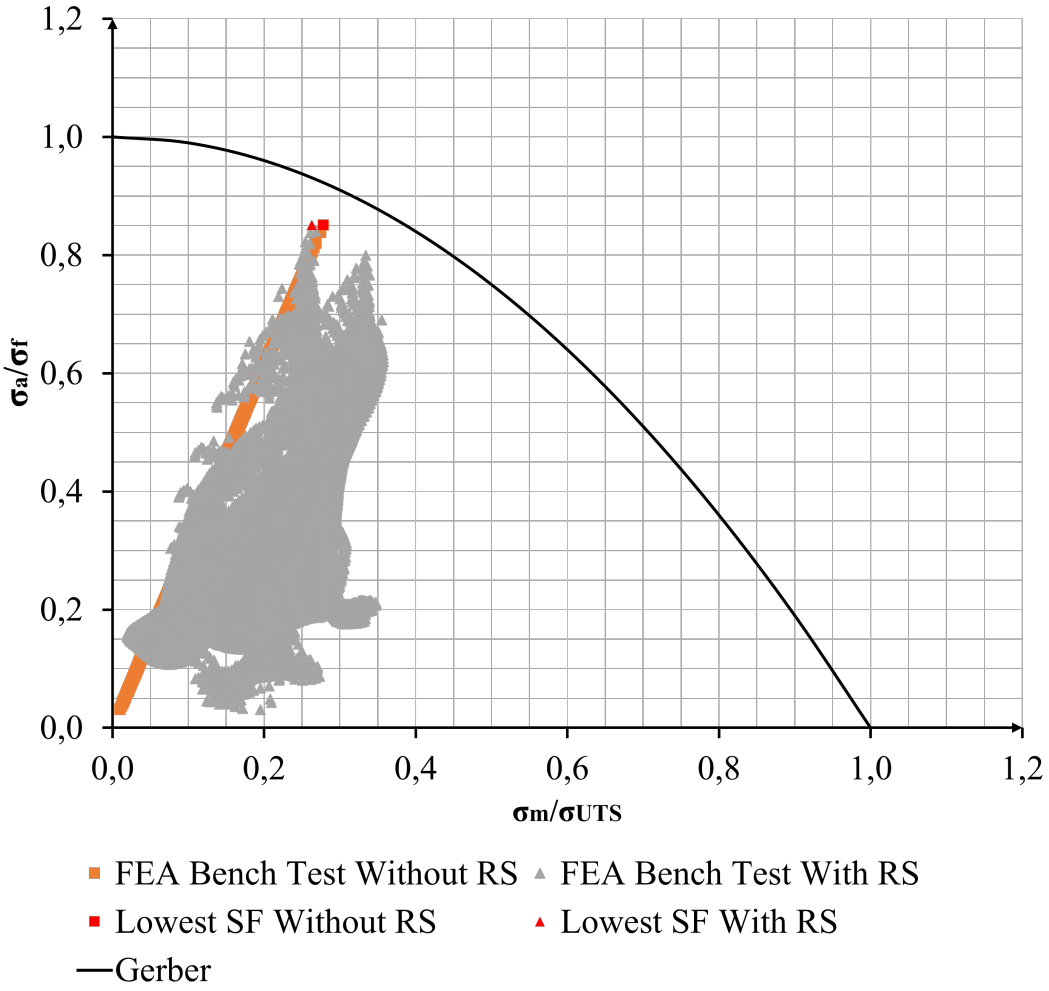

Figure 5.19 – Amplitude and mean stress (with and without RS) in comparison to the material limits predicted by Gerber's model on region A.

Region B is located near a fixation element and was the third most critical region for fatigue failure during the bench test. Figure 5.20 shows the alternate and mean stress data for region B. The stress data without residual stress is not distributed in a linear manner, such as seen in region A. This is explained due to the proximity of this region to a fixation element. The nodes which are closer to the fixation element are highly influenced by the fixation static load, which impacts the mean stress. Several nodes in the stress data without residual stress are outside the safe region predicted by Gerber's model, despite the survival of this region in the bench test. When residual stresses influence is accounted, almost all nodes are shifted to lower values of mean stress, indicating a predominant compressive residual stress in this region, which is beneficial to fatigue performance. This might partially explain why this region does not fail in the bench test.

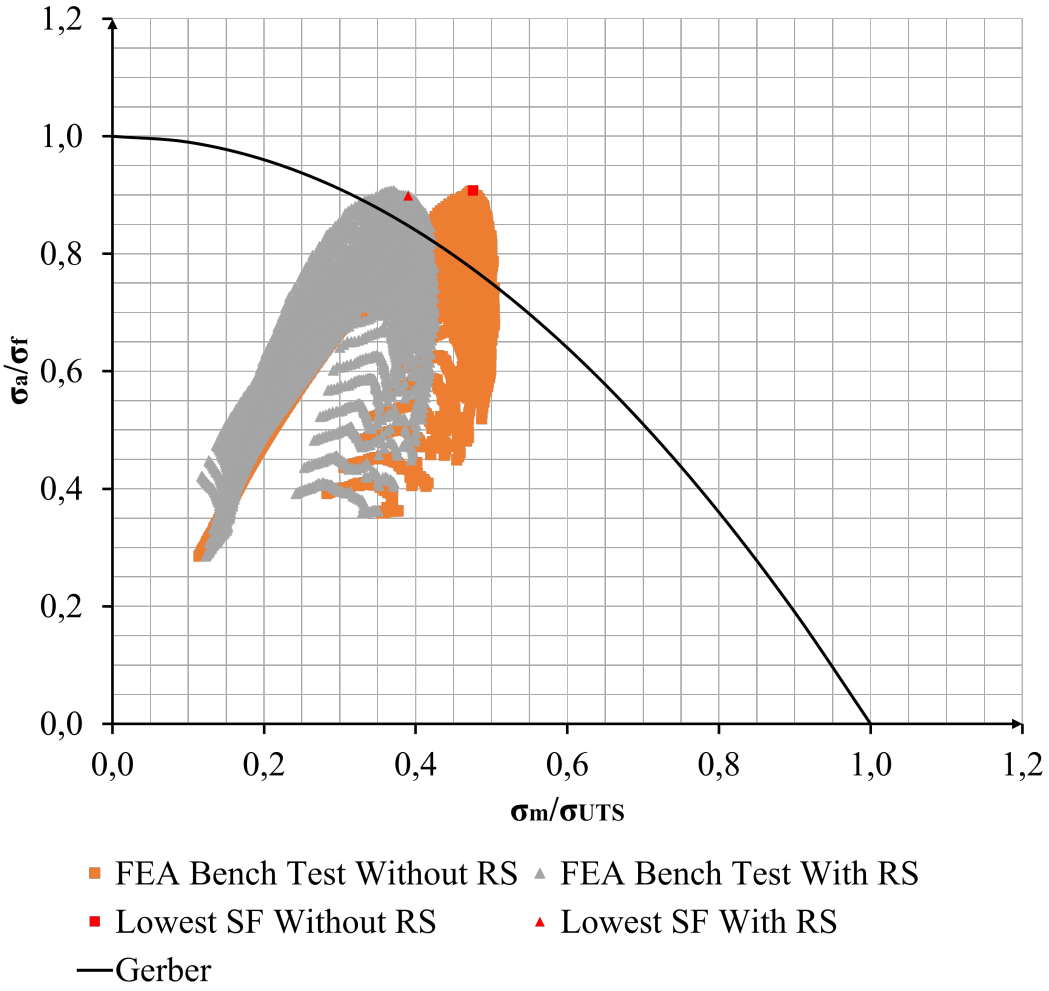

Figure 5.20 – Amplitude and mean stress (with and without RS) in comparison to the material limits predicted by Gerber's model on region B.

Region C was the region which presented most failures during the bench test. Figure 5.21 shows the alternate and mean stress data for region C. The stress data without residual stress is distributed in a linear manner, similar as seen in region A, as this part is also far from any fixation element. The stress data without residual stress is fully located within the safe region predicted by Gerber's model. When residual stresses are taken into account, the stress data is strongly shifted to higher mean stress values, which results in the movement of the data to a region out of the safe region predicted by Gerber's model. This indicates a predominant tensile residual stress in this region, which is detrimental for fatigue performance and seems to have a high influence in the failures seen in this region.

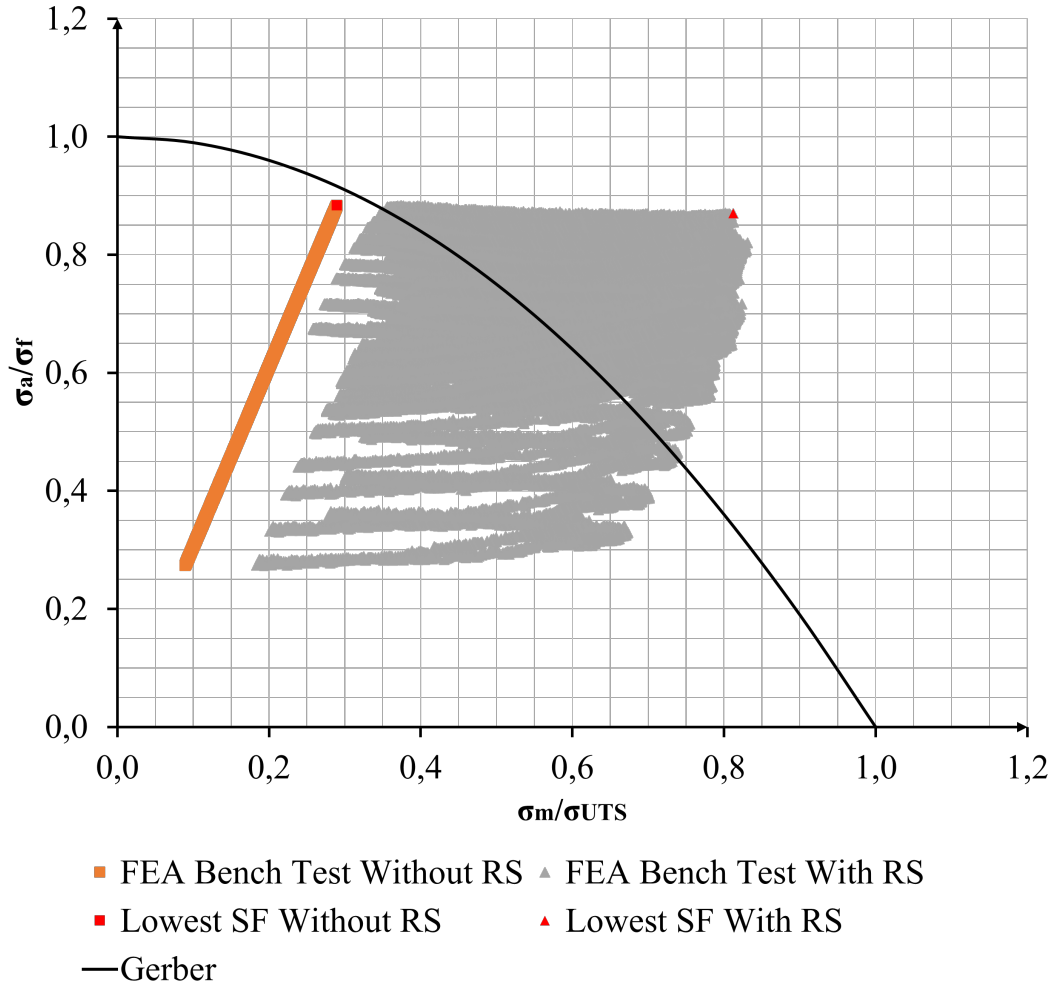

Figure 5.21 – Amplitude and mean stress (with and without RS) in comparison to the material limits predicted by Gerber's model on region C.

Region D did not present any failures in the bench test. Figure 5.22 shows the alternate and mean stress data for region D. The stress data without residual stress is distributed in a linear manner, similar as seen in region A and C, as this part is also far from any fixation element. The comparison of regions C and D with no residual stress suggests a similar behavior in expected fatigue performance, which was not seen in the bench test. While region C presented a predominant tensile residual stress, region D presented a variation of compressive and tensile residual stress spread across this region. However, the most critical region presented a predominant compressive residual stress, which improves the fatigue performance. Thus, the addition of the residual stress could improve the prediction of both regions.

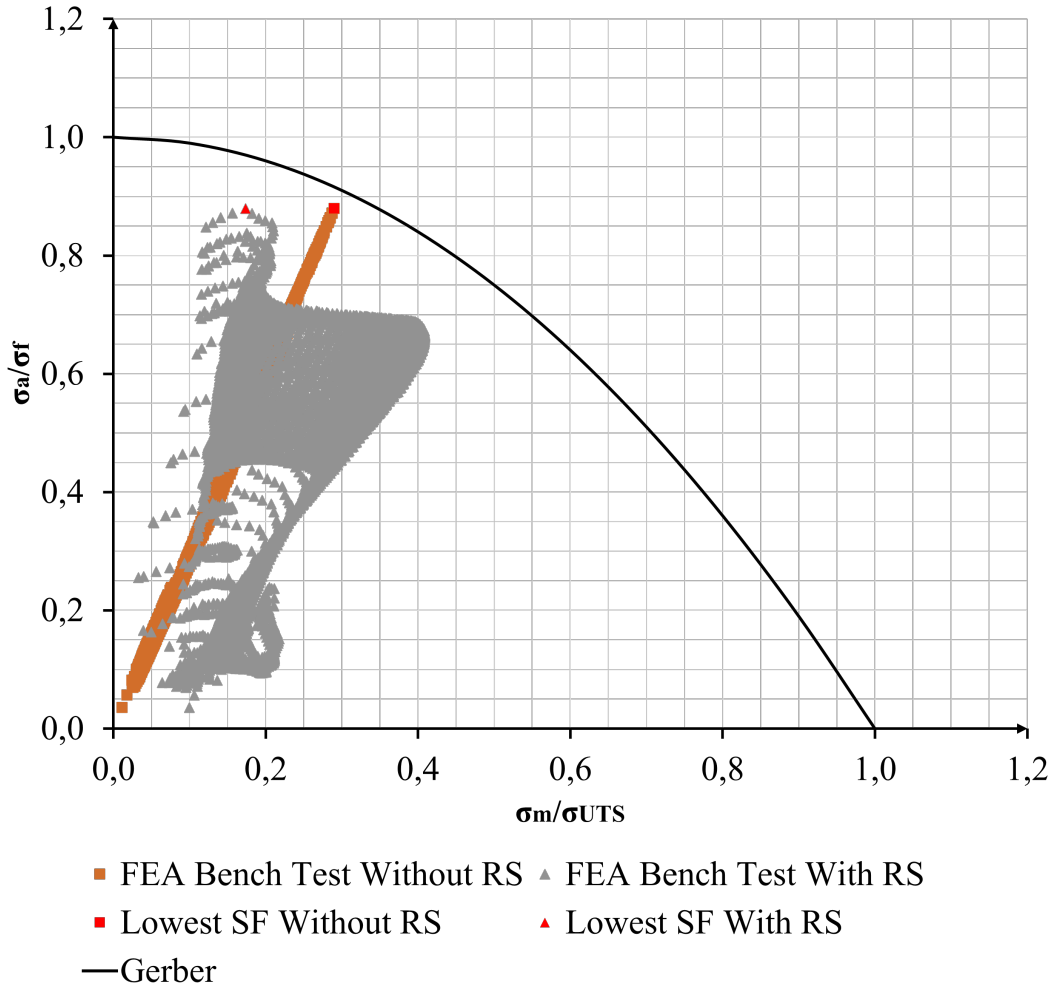

Figure 5.22 – Amplitude and mean stress (with and without RS) in comparison to the material limits predicted by Gerber's model on region D.

Figure 5.23 shows an overview of the residual stress impact on the most critical node for each of the four analyzed regions. Region A was only slightly modified by RS. Region B showed a shift towards the safe region predicted by Gerber's model, but not enough to enter such region. Region C was the most impacted by the residual stress, as the most critical node was shifted to a zone far from the material limits (the point without residual stress is almost coincident to the similar point of region D; thus, it is almost not visible in the image). Region D was close to the material limits and was shifted inwards the safe region when the RS was taken into account.

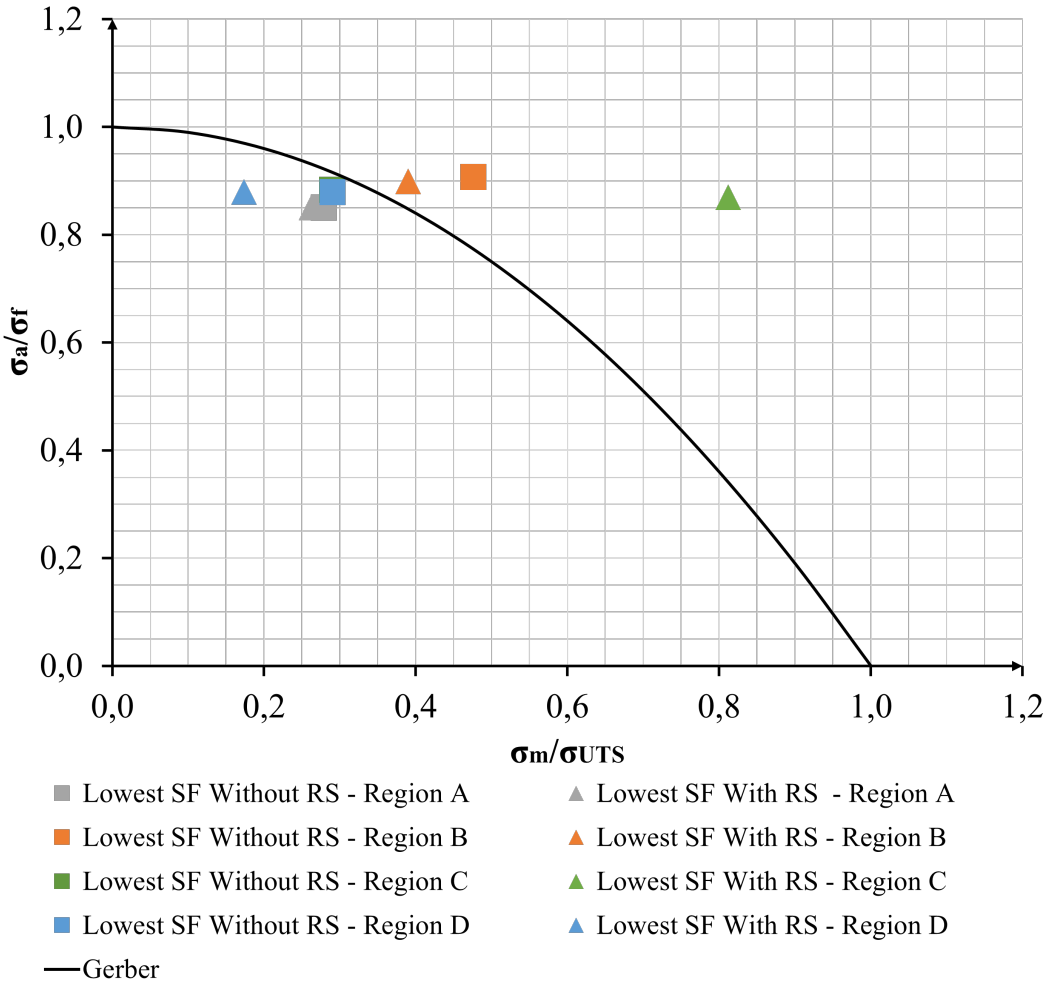

Figure 5.23 – Overview of the residual stress impact on the most critical node for each of the four analyzed regions.

Figure 5.24 shows the classification of the regions according to number of occurrences of fatigue failure seen in the FEA bench test and the failures predicted by Gerber's model with and without residual stress. Ideally, the lowest SF_e would represent the most critical region for failure in the bench test and the highest SF_e value would represent the least critical region. The SF_e with and without residual stress are given on table 5.1 for the four analyzed regions.

Region C is the most critical for fatigue failures in the FEA bench test, as 57% of the failures occurred in this region. Region A is the second most critical, presenting 28% of the failures. The remaining 15% of the failures were detected on region B and no failures were detected on region D, but it was considered on the analysis as this is a common region for failures during the bench test.

Table 5.1 – Bench test SF_e with and without RS.

	SF Without RS	SF With RS (CP1)	ΔSF (%)
Region A	1,02	1,03	+0,98
Region B	0,90	0,96	+6,67
Region C	1,03	0,74	-28,16
Region D	1,03	1,10	+6,80

The comparison of the FEA bench test results to the SF_e shows that the order of the SF_e without RS does not match the order seen in the experimental bench test, where the four positions are in the wrong order. When RS are taken into account, the most and the least critical regions now match the order seen in the bench test, while the second and third places are inverted, region B and A, respectively.

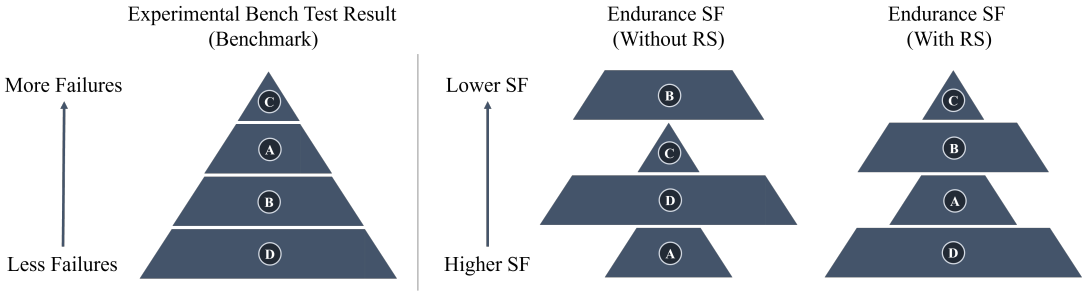

Figure 5.24 – Classification of the most to the least critical regions for fatigue failures seen in the bench test and predicted by Gerber's model with and without residual stress.

Region B showed high a stress amplitude, which are higher than 90% of the fatigue limit for the fully reversed load (σ_f). The RS effect on this region resulted in a shift of the nodes to lower values of mean stress, however, the shifted data is still approximately in the half of the distance that it would have to go through to get in the safe region. This indicates a residual stress with twice of the current magnitude would be needed to get in the safe zone predicted by Gerber's model. This might indicate that there are other influence factors that are not taken into account in the current method. This region is close to a fixation element, which might have additional effects on the fatigue performance. The stresses seen in this region are close to the yield strength of the material, which could also have an impact on fatigue performance.

Figure 5.25 shows the normalized maximum principal stress (divided by the ultimate tensile stress at room temperature) evolution during quenching, artificial ageing and

machining. The stress is evaluated in a similar location as the most critical node seen in the previous four analyzed regions. During quenching, it can be seen that high magnitude maximum principal stress arises only in region C, as region D shows low stress and regions A and B shows almost negligible stresses. During artificial ageing the stresses are partially relaxed in all regions, which brings the stress level of regions A, B and D to very low magnitudes. When the material is removed by the machining, the stress level seen in region C is sharply increased to a similar level as seen previous to the artificial ageing. By the end of the manufacturing process, region C is the only one that has a significant maximum principal stress magnitude, which is coherent to the mean stress shift to higher values on region C, as seen in Figure 5.21

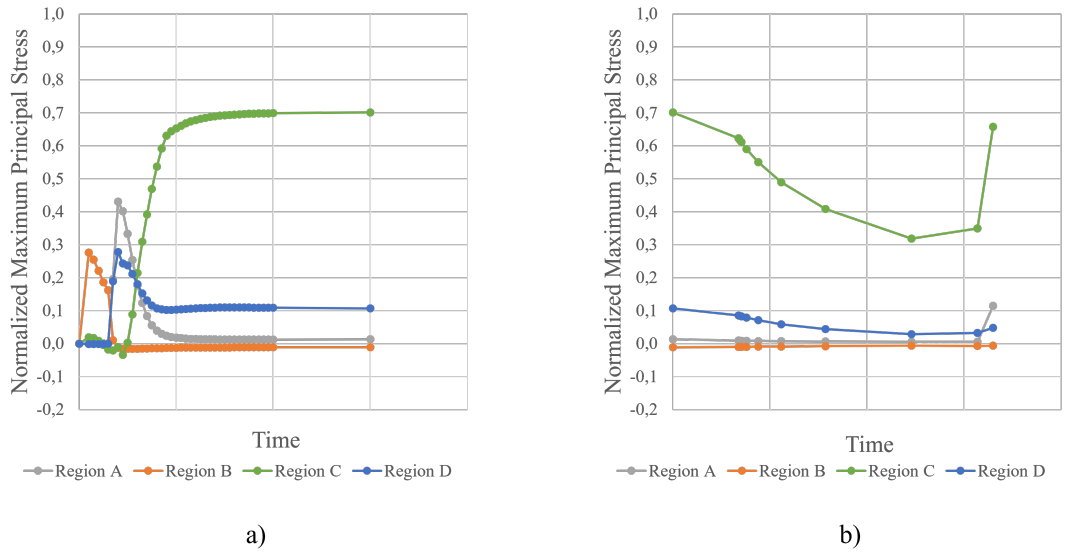

Figure 5.25 – Evolution of the normalized maximum principal stress during a) quenching and b) artificial ageing and machining.

Figure 5.26 shows the normalized minimum principal stress (divided by the ultimate tensile stress at room temperature) evolution during quenching, artificial ageing and machining. In quenching, region B presented the highest magnitude of minimum principal stress among the analyzed regions, but only approximately 40% of the ultimate tensile stress σ_{UTS} (used as reference in the absence of the ultimate compressive stress). Region A presented lower magnitudes, approximately 20% of σ_{UTS}. The remaining regions presented even lower magnitudes. In the artificial ageing process, all regions are partially relaxed, resulting in a decrease in the minimum principal stress magnitude. The

machining process further decreased the stress magnitude in all regions. By the end of the manufacturing process, region B is the only one which remained with significant minimum principal stress magnitude, which is coherent to the mean stress shift to lower values on region B, as seen in Figure 5.20.

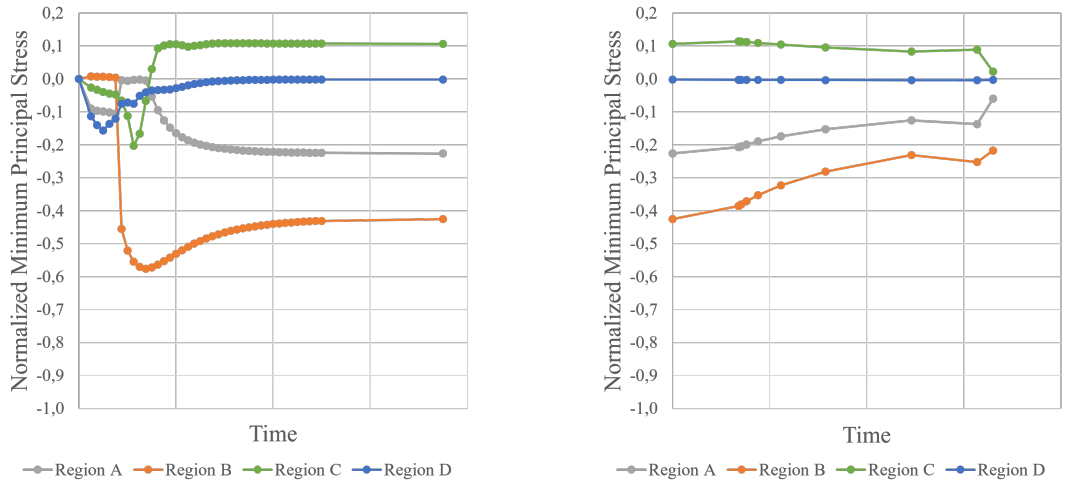

Figure 5.26 – Evolution of the normalized minimum principal stress during a) quenching and b) artificial ageing and machining.

The thermal profiles from CP2 and CP8 were also used to calculate the residual stress and, subsequently, the endurance safety factors. This procedure allows us to evaluate the model sensitivity to the variation of the imported thermal profile. These profiles presented the greatest deviation from CP1, as can be seen in Figure 5.11. A similar analysis as done in CP1 was carried on, and the dispersion seen among the residual stress resulting from the three thermal histories was analyzed.

Figure 5.27 shows the comparison of the normalized alternate and mean stress resulting from the bench test on region A using CP1, CP2 and CP8 as input for the calculation of the residual stress. Figure 5.11 shows that the highest cooling rate is the one resulting from CP2, the intermediate cooling rate is seen on CP1 and the lowest cooling rate is seen on CP8. A direct correlation is seen in the residual stress magnitude on region A, where the highest cooling rates (CP2) resulted in a higher predominant tensile residual stress. This effect can be seen in the overall shifting of the points and also the critical point to higher mean stress values on CP2. The points from CP8 have an

overall shift to higher mean stresses, but the critical point is shifted to a lower mean stress value. CP1 showed an intermediate behavior between CP2 and CP8, which reinforced the correlation to the cooling rate and the level of residual stress formation on this region.

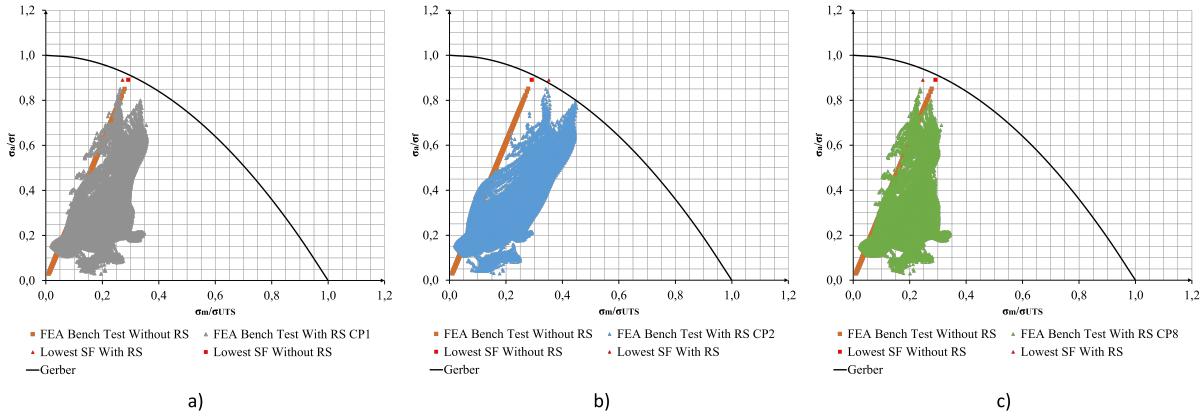

Figure 5.27 – Comparison of the mean and alternate stress resulting from the bench test on region A using the thermal history from a)CP1 b)CP2 and c)CP8.

Figures 5.28 and 5.29 shows that region B and C have a lower sensitivity to the variation of the thermal profile, among the tested variants. Only a marginal difference can be seen in the residual stress resulting from CP1, CP2 and CP8.

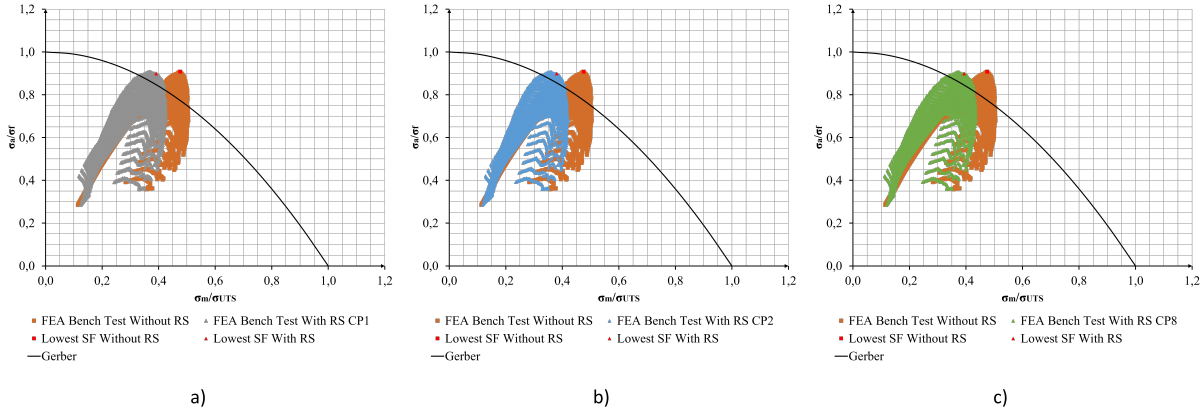

Figure 5.28 – Comparison of the mean and alternate stress resulting from the bench test on region B using the thermal history from a)CP1 b)CP2 and c)CP8.

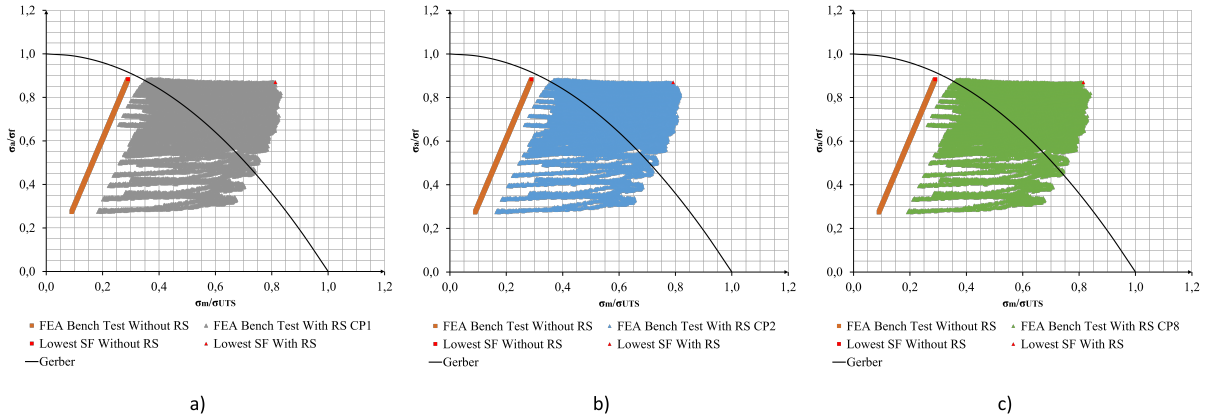

Figure 5.29 – Comparison of the mean and alternate stress resulting from the bench test on region C using the thermal history from a)CP1 b)CP2 and c)CP8.

Figure 5.30 shows the opposite correlation between residual stress and cooling rate as seen in region A. The highest cooling rate (CP2) induced the creation of the highest compressive predominant residual stress on the most critical node, as can be seen on the shifting of the critical node to lower mean stress values. The lower cooling rate (CP8) induced the creation of the least compressive predominant residual stress on the same node, as can be seen in the smaller shift on the critical node to smaller mean stress values on the critical node from CP8. Similarly, as seen in region A, CP1 showed an intermediate behavior between CP2 and CP8, which further reinforces the correlation of the cooling rate and residual stress formation.

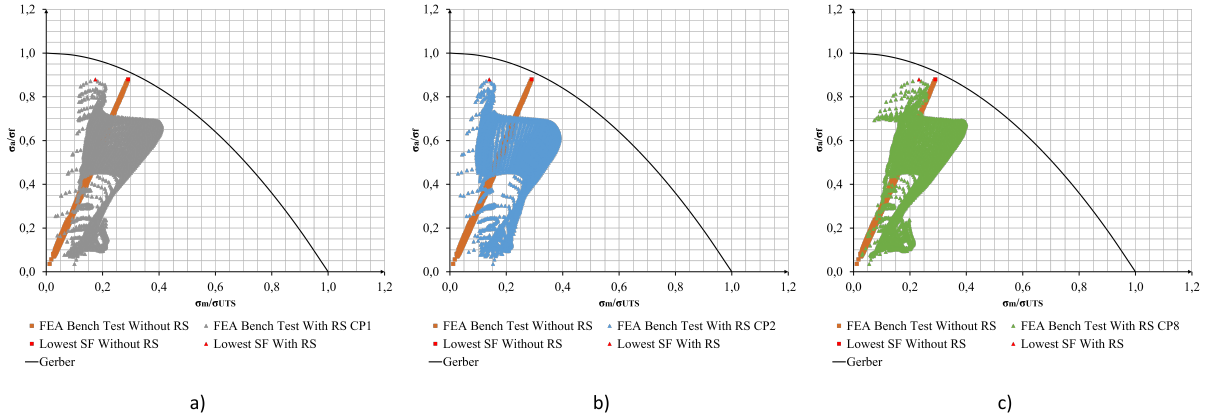

Figure 5.30 – Comparison of the mean and alternate stress resulting from the bench test on region D using the thermal history from a)CP1 b)CP2 and c)CP8.

Figure 5.31 shows the comparison of the bench test endurance safety factor on the

most critical node on regions A, B, C and D with residual stress from CP1, CP2 and CP8 and without residual stress. The residual stress on regions B and D shifted the SF_e to higher values on all tested candidate points (CP1, CP2 and CP8), while region C has its SF_e shifted to lower safety factors for all candidate points. However, region A showed a mixed behavior as CP1 and CP8 shifted SF_e to higher values and CP2 shifted it to lower values. Despite the good agreement between CP1, CP2 and CP8 results, this indicates that further experimental could be used to validate which CP is the most appropriate and if the residual stress has a positive or a negative impact on this region.

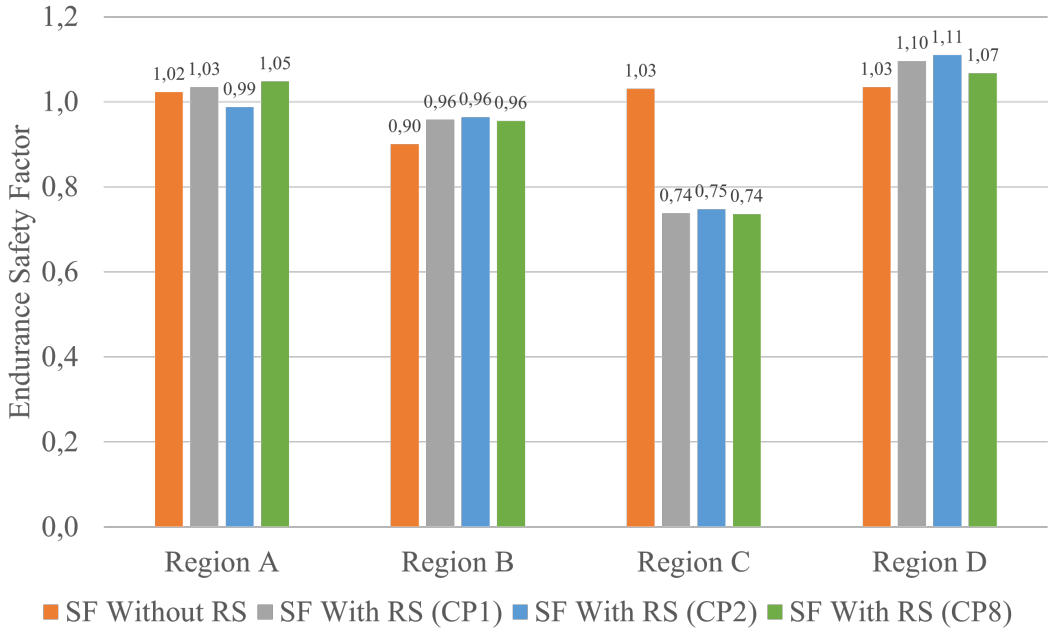

Figure 5.31 – Comparison of bench test endurance safety factor on the most critical node from regions A, B, C and D using different sources of residual stress (none, CP1, CP2 and CP8).

Despite the variation of SF_e seen among the tested CPs, the order of most to least critical SF_e remains the same as seen in Figure 5.24 for all tested cases in which residual stress was considered in the calculation. The second and third most critical regions should be regions A and B, respectively. However, the calculation shows an inverted order of criticality. The SF_e resulting from CP2 showed a difference of only 0.03 between these regions, but still in the wrong order. Other parameters also have an impact on the occurrence of fatigue failures, such as surface finishing, stress gradient, geometry deviations, and many other parameters which are not in the scope of this analysis but

could have an impact on the SF_e calculation and their consideration in the analysis could lead to the correct prediction of the order of criticality seen on the bench test.

6 CONCLUSION

This work proposes a methodology to predict the residual stress imposed on cylinders during a T6 thermal treatment and its impact on a subsequent bench test endurance performance. The proposed uncoupled thermal-thermomechanical approach captures the most relevant mechanical phenomena for the residual stress formation and relaxation, where the fatigue prediction accuracy is improved using the residual stress as a mean stress modifier in the endurance safety factor calculation.

For the thermal problem, the inverse heat transfer problem allowed the fitting of the cooling curves in the regions where experimental data is available. The HTC curves, reconstructed from the set of the best candidates (h_i parameters), showed a significant dispersion in some parameters. However, the sensitivity analysis showed that such dispersion has a low impact on the resulting cooling curves. Therefore, as expected, any of the best candidates will result in similar temperature curves in the regions where experimental data is available. Finally, for the thermal problem, the proposed methodology to evaluate the thermal history during the heat treatment showed to be adequate, as the chosen HTC curves resulting from the inverse heat transfer problem could reproduce the experimental cooling curves with good accuracy.

Moreover, complementary studies were performed to understand possible results variations on the resulting temperature field due to the reduced temperature history data during T6 thermal treatment (4 sets of data). This type of study is useful because, in addition to providing more information about the characteristics of the results, it allows us to outline new approaches for future studies indicating regions to obtain a new set of experimental data that aim to improve the confidence of the results and conclusions. Then, when analyzing the regions where no experimental data is available, the results show that CP1 results in a mean cooling rate among the 11 best candidates, while CP2 and CP8 show the highest and lowest cooling rates, respectively. This observation corroborates the choice of CP1, as the mean behavior minimizes the potential deviation from the unknown real cooling curve in this region.

For the thermomechanical problem, the calculated thermal history from CP1 was used as a boundary condition in the model to predict the residual stress resulting from it. The final residual stress distribution is then used as a mean stress modifier in the

SF_e, evaluated using a FEA bench test. The resulting SF_e, with and without the residual stress consideration, were compared to the experimental bench test fatigue data, which showed that the consideration of the residual stress improves the fatigue model accuracy.

Additionally, a sensitivity analysis to study the choice of the best candidate was performed using the thermal history from CP2 and CP8, instead of the thermal history obtained from CP1. The resulting SF_e showed a similar behavior between the three candidates, which shows the convergence of the calculated thermal profiles.

Finally, the application of the proposed methodology allowed the correct prediction of the most critical region for fatigue failure and improve the overall prediction of other regions when compared to the calculation without residual stress consideration. The correct prediction of the most critical region is of great importance in the development of new components, as it allows the optimization efforts to be spent on the most critical part of the component. This saves resources that would be otherwise spent in the manufacturing and testing of prototypes that would inadvertently fail, as well as resources spent in the optimization of regions that would not fail. Additionally, the accurate assessment of the real loads allows the part to be designed to work closer to the material limits, resulting in lighter and more reliable components.

6.1 Suggestion for next works

Numerical observations indicate that there are regions with a higher dispersion on the cooling curves (from -21% to +23% - Figure 5.11) when all the best candidates obtained from optimization are studied. Therefore, additional experimental data could be measured in different regions of the part. A fifth temperature field can be obtained in this region to determine which candidate has the most appropriate response. Furthermore, the additional data could be used to further refine the heat transfer activation timing to model the water entrance effect.

The water entrance effect could also be improved by solving the water flow during quenching. A computational fluid dynamics (CFD) model could be built to improve the representation of fluid-dynamics effects which were not physically modeled in the current method.

The residual stress level was indirectly validated through its impact on the component fatigue performance. Experimental measurements could be assessed to directly

validate the calculated residual stress level.

Fatigue assessment could also be further investigated in future works. For example, a multiaxial fatigue model could be implemented to check the endurance safety factors with a more comprehensive model. In addition, other parameters that impact fatigue performance could also be considered in the calculation, such as surface finish and local stress gradients.

REFERENCES

Adeyemi, M. B., Stark, R. A., and Modlen, G. F., p. 122–125. Metals Society, 1979 edition, 1979.

ANSYS, I. **Ansys Mechanical APDL Theory Reference**, 2022.

Babu, K. and Prasanna Kumar, T. Mathematical modeling of surface heat flux during quenching, **Metallurgical and Materials Transactions B**, vol. 41(1), p. 214–224, 2009.

Bathe, K.-J. **Finite Element Procedures**. Prentice-Hall, 2019.

Budynas, R. G., Nisbett, J. K., Shigley, J. E., and Tangchaichit, K. **Shigley's Mechanical Engineering Design**. McGraw-Hill Education, 2021.

Chiocca, A., Frendo, F., and Bertini, L. Residual stresses influence on the fatigue strength of structural components, **Procedia Structural Integrity**, vol. 38, p. 447–456, 2022.

Dahle, A. Aluminum alloys, heat treatment of, **Encyclopedia of Materials: Science and Technology**, p. 111–113, 2001.

Davis, J. R. **ASM speciality handbook: Aluminium and aluminium alloys**. ASM, 1993.

Denkena, B., Boehnke, D., and de León, L. Machining induced residual stress in structural aluminum parts, **Production Engineering**, vol. 2(3), p. 247–253, 2008.

Dixit, M., Mishra, R., and Sankaran, K. Structure–property correlations in al 7050 and al 7055 high-strength aluminum alloys, **Materials Science and Engineering: A**, vol. 478(1-2), p. 163–172, 2008.

Dolan, G. and Robinson, J. Residual stress reduction in 7175-T73, 6061-T6 and 2017a-T4 aluminium alloys using quench factor analysis, **Journal of Materials Processing Technology**, vol. 153-154, p. 346–351, 2004.

Earle, T., Robinson, J., and Colvin, J. Investigating the mechanisms that cause quench cracking in aluminium alloy 7010, **Journal of Materials Processing Technology**, vol. 153-154, p. 330–337, 2004.

El-Axir, M. A method of modeling residual stress distribution in turning for different materials, **International Journal of Machine Tools and Manufacture**, vol. 42(9), p. 1055–1063, 2002.

Exler, O. and Schittkowski, K. A trust region SQP algorithm for mixed-integer nonlinear programming, **Optimization Letters**, vol. 1(3), p. 269–280, 2006.

Faghri, A. and Zhang, Y. **10 - BOILING**. Academic Press, Boston, 2006.

Faupel, J. H. and Fisher, F. E. **Engineering design: A synthesis of stress analysis and Materials Engineering**. J. Wiley and Sons, 1981.

Fletcher, D. Q. **Mechanics of Materials**. Holt, Rinehart, and Winston, 1985.

Frost, N., Marsh, K. J., and Pook, L. P. **Metal Fatigue**. Oxford University Press, 1974.

Fuh, K.-H. and Wu, C.-F. A residual-stress model for the milling of aluminum alloy (2014-T6), **Journal of Materials Processing Technology**, vol. 51(1-4), p. 87–105, 1995.

Gartling, D. K. Convective heat transfer analysis by the Finite Element Method, **Computer Methods in Applied Mechanics and Engineering**, vol. 12(3), p. 365–382, 1977.

Godlewski, L. A., Su, X., Pollock, T. M., and Allison, J. E. The effect of aging on the relaxation of residual stress in cast aluminum, **Metallurgical and Materials Transactions A**, vol. 44(10), p. 4809–4818, 2013.

Hertzberg, R. W. **Deformation and Fracture Mechanics of Engineering Materials**. Wiley, 4th edition edition, 1996.

Hughes, T. J. R. **The Finite Element Method: Linear Static and Dynamic Finite Element Analysis**. Prentice-Hall, 1987.

James, M. Relaxation of residual stresses an overview, **Residual Stresses**, p. 349–365, 1987.

Jan, J. and Nannapuraju, M. CFD Investigation of Quench Media and Orientation Effects on Structural Stress Induced in the Intense Quenching Processes for Aluminum Cylinder Heads, **Heat Treat 2017: Proceedings of the 29th ASM Heat Treating Society Conference**, 2017.

Jean, L. and Chaboche, J.-L. **Mechanics of Solid Materials**. Cambridge University Press, 2009.

Jeanmart, P. and Bouvaist, J. Finite element calculation and measurement of thermal stresses in quenched plates of high–strength 7075 aluminium alloy, **Materials Science and Technology**, vol. 1(10), p. 765–769, 1985.

Kobayashi, K., Nakamura, O., and Haraguchi, Y. Water Quenching CFD (Computational Fluid Dynamics) Simulation with Cylindrical Impinging Jets, **NIPPON STEEL; SUMITOMO METAL TECHNICAL REPORT**, vol. 111, p. 62–71, 2016.

Kopun, R., Zhang, D., Edelbauer, W., Stauder, B., Basara, B., and Greif, D. Immersion quenching simulation of realistic cylinder head geometry, **SAE International Journal of Materials and Manufacturing**, vol. 7(3), p. 520–529, 2014a.

Kopun, R., Škerget, L., Hriberšek, M., Zhang, D., Stauder, B., and Greif, D. Numerical simulation of immersion quenching process for cast aluminium part at different pool temperatures, **Applied Thermal Engineering**, vol. 65(1-2), p. 74–84, 2014b.

Koç, M., Culp, J., and Altan, T. Prediction of residual stresses in quenched aluminum blocks and their reduction through cold working processes, **Journal of Materials Processing Technology**, vol. 174(1-3), p. 342–354, 2006.

Krige, D. G. A Statistical Approach to Some Basic Mine Valuation Problems on the Witwatersrand, **Journal of the Chemical, Metallurgical and Mining Society of South Africa**, vol. 52, p. 119–139, 1951.

Kunugi, T. "MARS for multiphase calculation, **Computational Fluid Dynamics Journal**, vol. 9(1), 2000.

Lacarac, V., Smith, D. J., and Pavier, M. J. Residual stress creep relaxation around cold expanded holes in an aluminium alloy, **AIAA Journal**, vol. 42(7), p. 1444–1449, 2004.

Leggatt, R. and Davey, T. Measurements of the reduction due to proof loads of residual stresses in simulated pressure vessel welds, **Mechanical Relaxation of Residual Stresses**, 1981.

Li, P., Maijer, D. M., Lindley, T. C., and Lee, P. D. Simulating the residual stress in an A356 automotive wheel and its impact on fatigue life, **Metallurgical and Materials Transactions B**, vol. 38(4), p. 505–515, 2007.

Louhichi, M. A., Poulachon, G., Lorong, P., Outeiro, J., and Monteiro, E. Experimental and simulative determination of residual stress during heat treatment of 7075-T6 aluminum, **Procedia CIRP**, vol. 108, p. 82–87, 2022.

Marin, J. Interpretation of fatigue strength for combined stresses, **Proceedings of International Conference on Fatigue of Metals**, p. 184–192, 1956.

McClung, R. C. A literature survey on the stability and significance of residual stresses during fatigue, **Fatigue and Fracture of Engineering Materials and Structures**, vol. 30(3), p. 173–205, 2007.

McDowell, D. An approximate algorithm for elastic-plastic two-dimensional rolling/sliding contact, **Wear**, vol. 211(2), p. 237–246, 1997.

Meduri, P. K., Warrier, G. R., and Dhir, V. K. Wall heat flux partitioning during subcooled forced flow film boiling of water on a vertical surface, **International Journal of Heat and Mass Transfer**, vol. 52(15-16), p. 3534–3546, 2009.

Merwin, J. E. and Johnson, K. L. An analysis of plastic deformation in rolling contact, **Proceedings of the Institution of Mechanical Engineers**, vol. 177(1), p. 676–690, 1963.

Nukiyama, S. The maximum and minimum values of the heat Q transmitted from metal to boiling water under atmospheric pressure, **Journal of the Society of Mechanical Engineers**, vol. 37(206), p. 367–374, 1934.

Padet, J. Transient convective heat transfer, **Journal of the Brazilian Society of Mechanical Sciences and Engineering**, vol. 27(1), p. 74–95, 2005.

Pereverzyev, S. S., Pinnau, R., and Siedow, N. Initial temperature reconstruction for nonlinear heat equation: Application to a coupled radiative conductive heat transfer problem, **Inverse Problems in Science and Engineering**, vol. 16(1), p. 55–67, 2008.

Pook, L. P. **Linear Elastic Fracture Mechanics for Engineers: Theory and Applications**. WIT Press, 2000.

Prime, M. B. and Hill, M. R. Residual stress, stress relief, and inhomogeneity in aluminum plate, **Scripta Materialia**, vol. 46(1), p. 77–82, 2002.

Radaj, D. **Heat effects of welding: Temperature field, residual stress, distortion**. Springer-Verlag, 1992.

Reinhardt, H.-J., Hào, D. N., Frohne, J., and Suttmeier, F.-T. Numerical solution of inverse heat conduction problems in two spatial dimensions, **Journal of Inverse and Ill-posed Problems**, vol. 15(2), p. 181–198, 2007.

Rice, R. C. **SAE Fatigue Design Handbook**. Society of Automotive Engineers, 1997.

Robinson, J. S. and Tanner, D. A. Residual stress development and relief in high strength aluminium alloys using standard and retrogression thermal treatments, **Materials Science and Technology**, vol. 19(4), p. 512–518, 2003.

Robinson, J. S., Tanner, D. A., and Truman, C. E. 50th anniversary article: The origin and management of residual stress in heat-treatable aluminium alloys, **Strain**, vol. 50(3), p. 185–207, 2014.

Sasahara, H., Obikawa, T., and Shirakashi, T. FEM analysis of cutting sequence effect on mechanical characteristics in machined layer, **Journal of Materials Processing Technology**, vol. 62(4), p. 448–453, 1996.

Schajer, G. S., Roy, G., Flamen, M. T., and Lu, J. **Handbook of measurement of residual stresses**. Liburn, GA, The Fairmont Press Inc., 1996.

Schulze, V., Arrazola, P., Zanger, F., and Osterried, J. Simulation of distortion due to machining of thin-walled components, **Procedia CIRP**, vol. 8, p. 45–50, 2013.

Sendeckyj, G. Constant life diagrams — a historical review, **International Journal of Fatigue**, vol. 23(4), p. 347–353, 2001.

Stephens, R. I., Fatemi, A., Stephens, R. R., and Fuchs, H. O. **Metal Fatigue in Engineering**. Wiley, 2000.

Suresh, S., **Introduction**, p. 1–1. Cambridge University Press, 1998.

Susmel, L. Fundamentals of Fatigue Assessment, **Multiaxial Notch Fatigue**, p. 33–97, 2009.

SUSMEL, L., TOVO, R., and LAZZARIN, P. The mean stress effect on the high-cycle fatigue strength from a multiaxial fatigue point of view, **International Journal of Fatigue**, vol. 27(8), p. 928–943, 2005.

Tensi, H. M., Stich, A., and Totten, G. E. Fundamentals about quenching by submerging, **Proceedings of International Heat Treating Conference: Equipment and Processes**, p. 243–251, 1994.

Wang, R., Ram, D., Stauder, B., Gutiérrez, R. F., Gariboldi, E., and Poletti, M. C. Stress relaxation during artificial aging of an alsi7cu0.5mg cast alloy, **Crystals**, vol. 12(8), p. 1168, 2022.

Weber, D., Kirsch, B., Chighizola, C., Jonsson, J., D'Elia, C., Linke, B., Hill, M., and Aurich, J. Investigation on the scale effects of initial bulk and machining induced residual stresses of thin walled milled monolithic aluminum workpieces on part distortions: experiments and finite element prediction model, **Procedia CIRP**, vol. 102, p. 337–342, 2021.

Webster, G. and Ezeilo, A. Residual stress distributions and their influence on fatigue lifetimes, **International Journal of Fatigue**, vol. 23, p. 375–383, 2001.

Webster, G. A. 'Neutron diffraction measurements of residual stresses in a shrnk-fit ring and plug: a round robin study, **VAMAS Report**, vol. 38, 2000.

Withers, P. and Bhadeshia, H. Residual stress. part 2 – nature and origins, **Materials Science and Technology**, vol. 17(4), p. 366–375, 2001.

Xiao, G., Chen, B., Li, S., and Zhuo, X. Fatigue life analysis of aero-engine blades for abrasive belt grinding considering residual stress, **Engineering Failure Analysis**, vol. 131, 2022.

Xiaoming H., Sun J., L. J. H. X. X. Q. An experimental investigation of residual stresses in high-speed end milling 7050-T7451 aluminum alloy, **Advances in Mechanical Engineering**, vol. 5, p. 592–659, 2013.

Yang, X., Zhu, J., Nong, Z., Lai, Z., and He, D. FEM simulation of quenching process in A357 aluminum alloy cylindrical bars and reduction of quench residual stress through cold stretching process, **Computational Materials Science**, vol. 69, p. 396–413, 2013a.

Yang, X.-w., ZHU, J.-c., LAI, Z.-h., LIU, Y., HE, D., and NONG, Z.-s. Finite element analysis of quenching temperature field, residual stress and distortion in a357 aluminum alloy large complicated thin-wall workpieces, **Transactions of Nonferrous Metals Society of China**, vol. 23(6), p. 1751–1760, 2013b.

Yang, Y., Deng, X., and Shi, W. Numerical simulation of stress evolutions in 2A14 aluminum alloy components during solution and aging process, **Heat Treatment and Surface Engineering**, vol. 4(1), p. 1–12, 2022.

Zhang, L., Feng, X., Li, Z., and Liu, C. FEM simulation and experimental study on the quenching residual stress of aluminum alloy 2024, **Proceedings of the Institution of Mechanical Engineers, Part B: Journal of Engineering Manufacture**, vol. 227(7), p. 954–964, 2013.

Zhang, W., Jiang, W., Zhao, X., and Tu, S.-T. Fatigue life of a dissimilar welded joint considering the weld residual stress: Experimental and finite element simulation, **International Journal of Fatigue**, vol. 109, p. 182–190, 2018.

APPENDIX A – Cooling curves from sensibility study

Table A.1 shows the parameters used on each case run on the sensibility study (S1 to S18). CP1 was used as base and the highlighted parameters were modified on each case. Parameters h_6 and h_7 were equal to zero on CP1; thus, no percent variation was possible on these parameters. A value of 5 and 10% of the peak curve were used on these cases to overcome this issue and evaluate the cost function sensibility to these parameters.

Table A.1 – Parameters used in the sensibility study.

	h1	h2	h3	h4	h5	h6	h7	h8	h9
CP1	h1	h2	h3	h4	h5	h6	h7	h8	h9
S1	0.95*h1	h2	h3	h4	h5	h6	h7	h8	h9
S2	1.05*h1	h2	h3	h4	h5	h6	h7	h8	h9
S3	h1	0.95*h2	h3	h4	h5	h6	h7	h8	h9
S4	h1	1.05*h2	h3	h4	h5	h6	h7	h8	h9
S5	h1	h2	0.95*h3	h4	h5	h6	h7	h8	h9
S6	h1	h2	1.05*h3	h4	h5	h6	h7	h8	h9
S7	h1	h2	h3	0.95*h4	h5	h6	h7	h8	h9
S8	h1	h2	h3	1.05*h4	h5	h6	h7	h8	h9
S9	h1	h2	h3	h4	0.95*h5	h6	h7	h8	h9
S10	h1	h2	h3	h4	1.05*h5	h6	h7	h8	h9
S11	h1	h2	h3	h4	h5	0.10*h5	h7	h8	h9
S12	h1	h2	h3	h4	h5	0.05*h5	h7	h8	h9
S13	h1	h2	h3	h4	h5	h6	0.10*h8	h8	h9
S14	h1	h2	h3	h4	h5	h6	0.05*h8	h8	h9
S15	h1	h2	h3	h4	h5	h6	h7	0.95*h8	h9
S16	h1	h2	h3	h4	h5	h6	h7	1.05*h8	h9
S17	h1	h2	h3	h4	h5	h6	h7	h8	0.95*h9
S18	h1	h2	h3	h4	h5	h6	h7	h8	1.05*h9

The cooling curves resulting for all 18 cases run on sensibility study (S1 to S18) are showed on figures A.1 to A.9 and compared to the benchmark CP1.

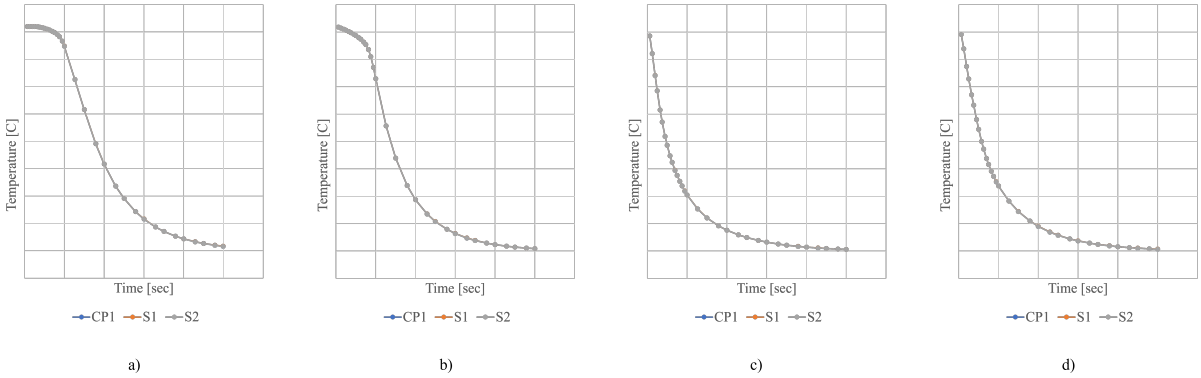

Figure A.1 – Cooling curves from h1 parameter variation on sensibility study on a)region 1 b)region 2 c)region 3 d)region 4

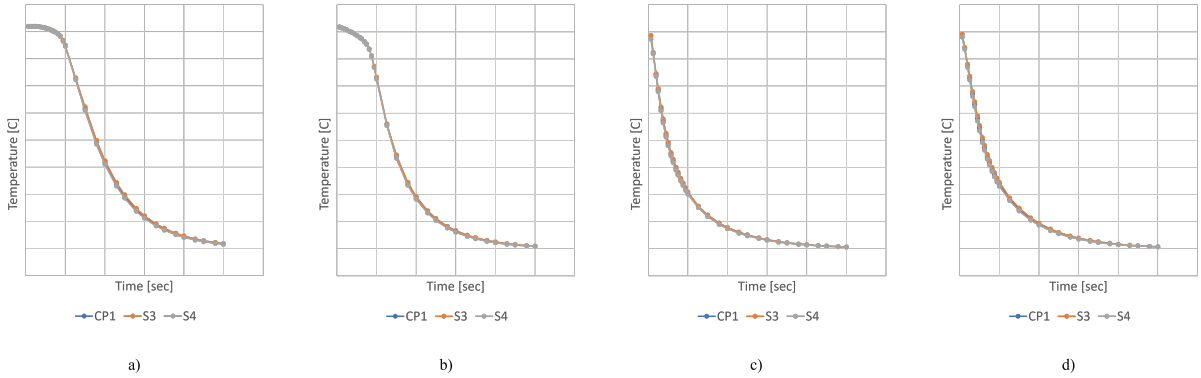

Figure A.2 – Cooling curves from h2 parameter variation on sensibility study on a)region 1 b)region 2 c)region 3 d)region 4

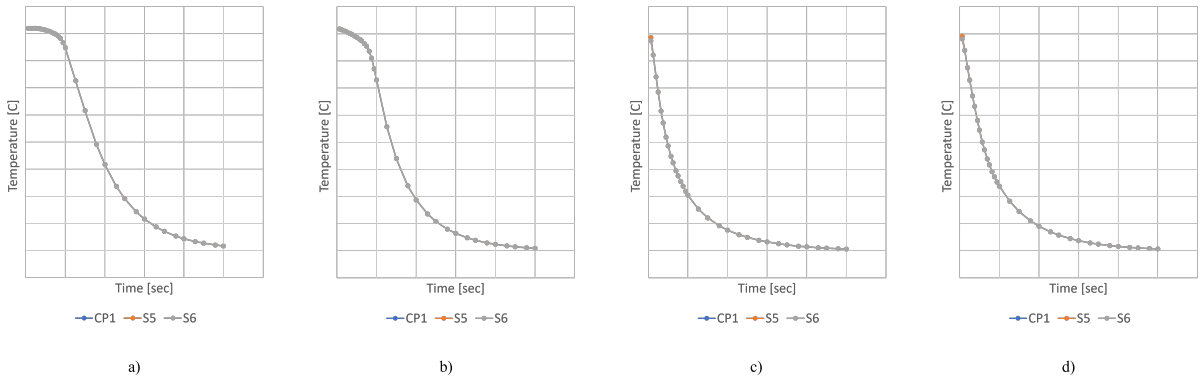

Figure A.3 – Cooling curves from h3 parameter variation on sensibility study on a)region 1 b)region 2 c)region 3 d)region 4

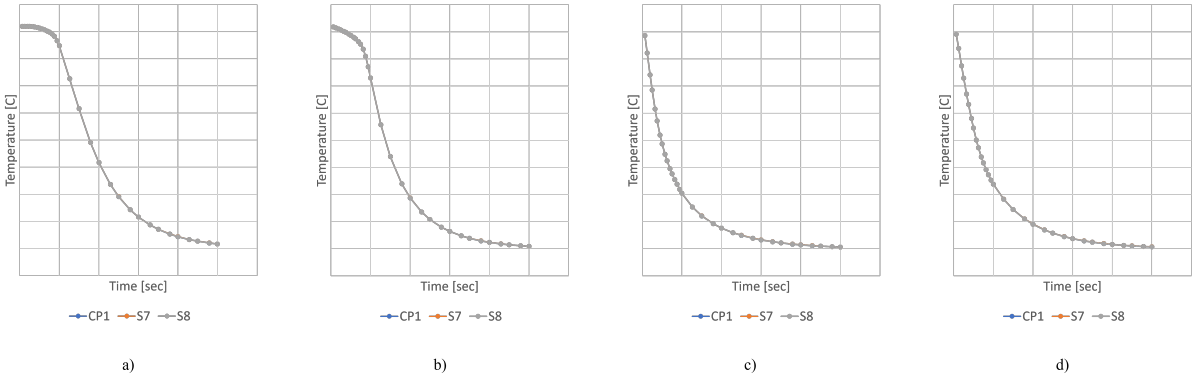

Figure A.4 – Cooling curves from h4 parameter variation on sensibility study on a)region 1 b)region 2 c)region 3 d)region 4

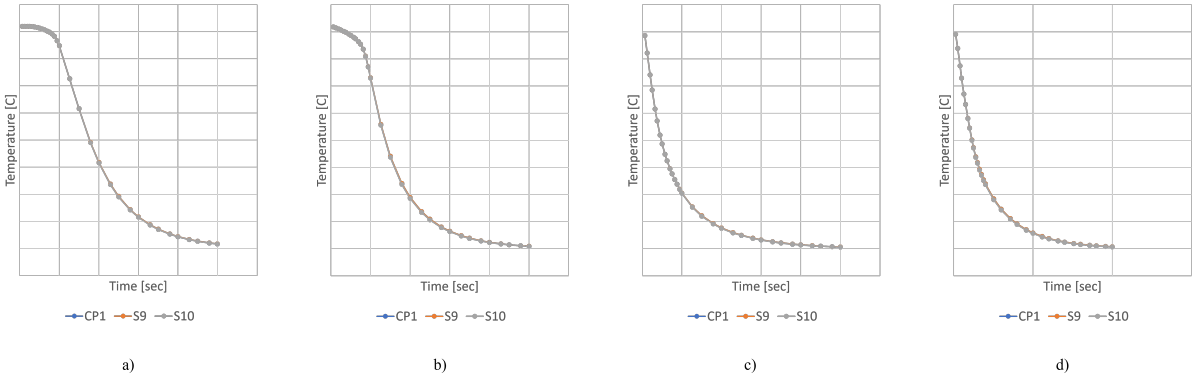

Figure A.5 – Cooling curves from h5 parameter variation on sensibility study on a)region 1 b)region 2 c)region 3 d)region 4

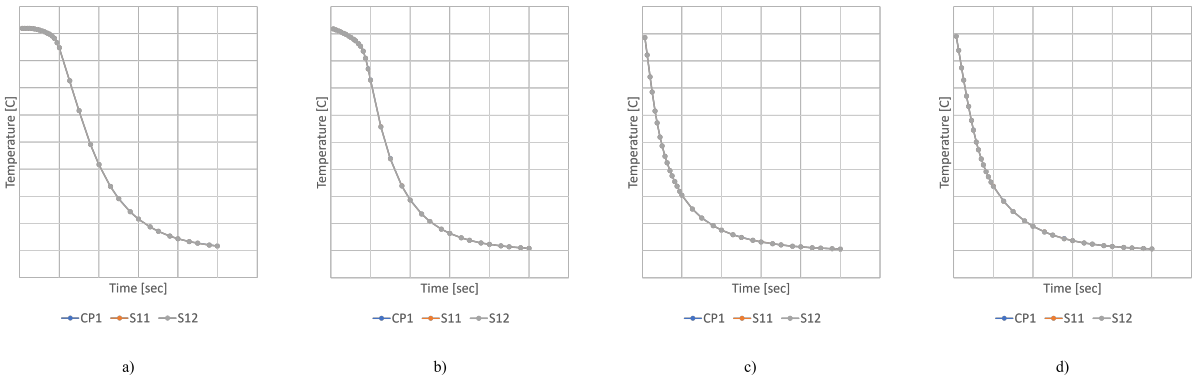

Figure A.6 – Cooling curves from h6 parameter variation on sensibility study on a)region 1 b)region 2 c)region 3 d)region 4

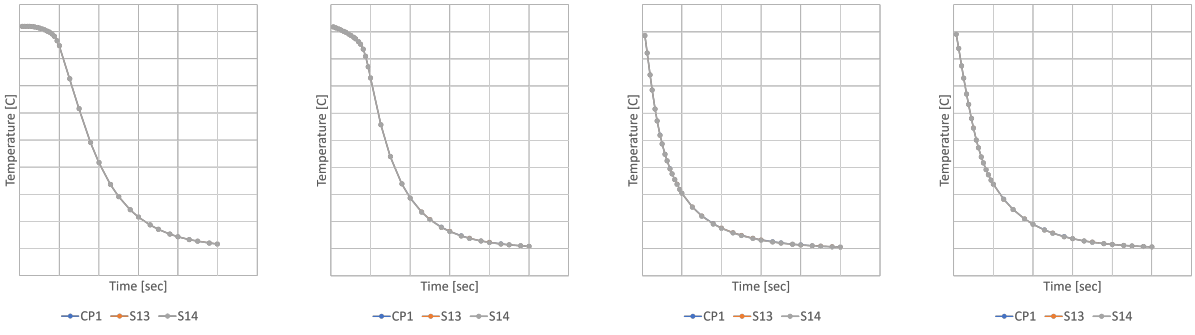

Figure A.7 – Cooling curves from h7 parameter variation on sensibility study on a)region 1 b)region 2 c)region 3 d)region 4

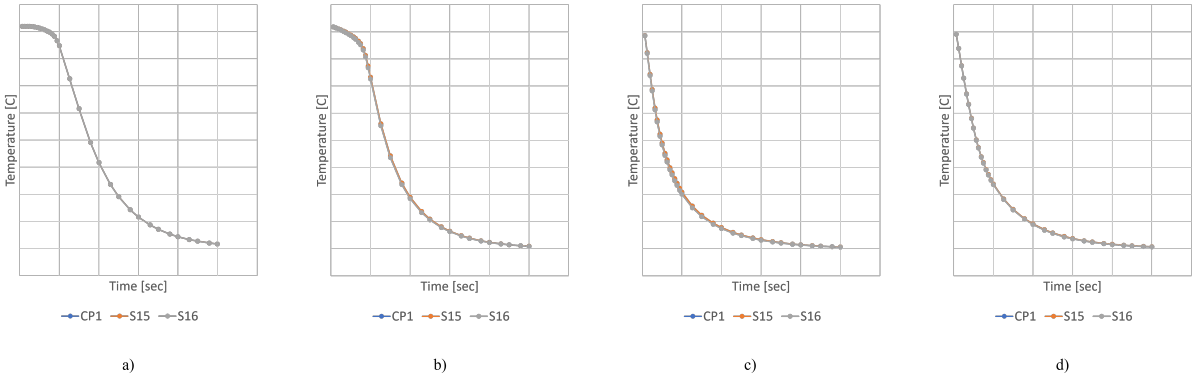

Figure A.8 – Cooling curves from h8 parameter variation on sensibility study on a)region 1 b)region 2 c)region 3 d)region 4

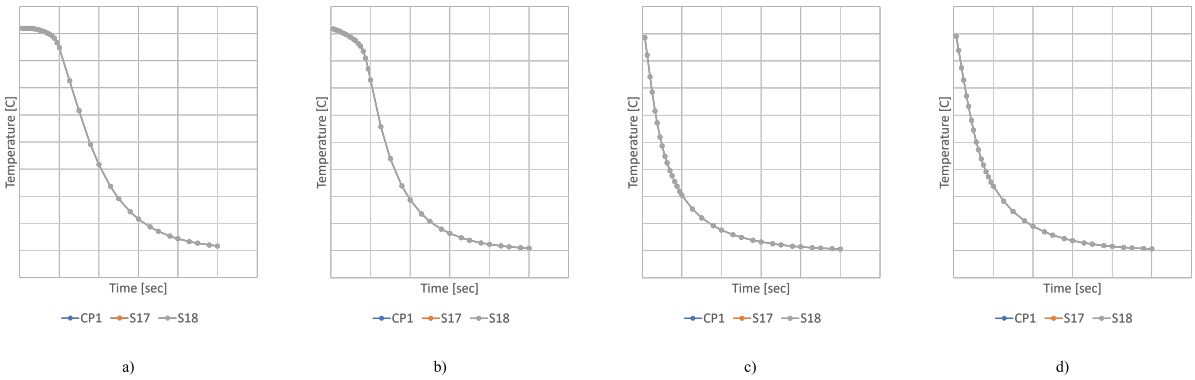

Figure A.9 – Cooling curves from h9 parameter variation on sensibility study on a)region 1 b)region 2 c)region 3 d)region 4